การเตรียมสารเพอรอฟสไกต์ $La_{1-x}Sr_xFe_{1-y}M_yO_{3-\delta}$ สำหรับวัสดุของเซลล์เชื้อเพลิงออกไซด์ของแข็ง

นางสาวอัญญ์ภัสร์สุดา ไชยวงศ์

วิทยานิพนธ์นี้เป็นส่วนหนึ่งของการศึกษาตามหลักสูตรปริญญาวิทยาศาสตรมหาบัณฑิต
สาขาวิชาปิโตรเคมีและวิทยาศาสตร์พอลิเมอร์
คณะวิทยาศาสตร์ จุฬาลงกรณ์มหาวิทยาลัย
ปีการศึกษา 2552

PREPARATION OF $La_{1-x}Sr_xFe_{1-y}M_yO_{3-\delta}$ PEROVSKITES FOR SOLID OXIDE FUEL CELL MATERIALS

Miss Aunpajsuda Chaiyawong

A Thesis Submitted in Partial Fulfillment of the Requirements
for the Degree of Master of Science Program in Petrochemistry and Polymer Science
Faculty of Science
Chulalongkorn University
Academic Year 2009

Thesis Title	PREPARATION OF $La_{1-x}Sr_xFe_{1-y}M_yO_{3-\delta}$ PEROVSKITES FOR SOLID OXIDE FUEL CELL MATERIALS
By	Miss Aunpajsuda Chaiyawong
Field of Study	Petrochemistry and Polymer Science
Thesis Advisor	Assistant Professor Oravan Sanguanruang, Ph.D.
Thesis Co-Advisor	Parichatr Vanalabhpatana, Ph.D.

Accepted by the Faculty of Science, Chulalongkorn University in Partial Fulfillment of the Requirements for the Master's Degree

…… Dean of the Faculty of Science
(Professor Supot Hannongbua, Dr.rer.nat.)

THESIS COMMITTEE

…… Chairman
(Associate Professor Sirirat Kokpol, Ph.D.)

…… Thesis Advisor
(Assistant Professor Oravan Sanguanruang, Ph.D.)

…… Thesis Co-Advisor
(Parichatr Vanalabhpatana, Ph.D.)

…… Examiner
(Associate Professor Wimonrat Trakarnpruk, Ph.D.)

…… External Examiner
(Associate Professor Preecha Phahonthep)

อัญญ์ภัสร์สุดา ไชยวงศ์ : การเตรียมสารเพอรอฟสไกต์ $La_{1-x}Sr_xFe_{1-y}M_yO_{3-\delta}$ สำหรับวัสดุของเซลล์เชื้อเพลิงออกไซด์ของแข็ง. (PREPARATION OF $La_{1-x}Sr_xFe_{1-y}M_yO_{3-\delta}$ PEROVSKITES FOR SOLID OXIDE FUEL MATERIALS) อ. ที่ปรึกษาวิทยานิพนธ์หลัก : ผศ.ดร. อรวรรณ สงวนเรือง, อ. ที่ปรึกษาวิทยานิพนธ์ร่วม : ดร. ปาริฉัตร วนลาภพัฒนา, 105 หน้า.

ศึกษาผลของการเติมสตรอนเทียมที่ตำแหน่ง A และโครเมียม นิกเกิล และคอปเปอร์ที่ตำแหน่ง B ต่อลักษณะโครงสร้างและสมบัติต่างๆ ของสารเพอรอฟสไกต์ $LaFeO_3$ จากการวิเคราะห์ด้วยเทคนิคการเลี้ยวเบนของรังสีเอ็กซ์ พบว่า $La_{1-x}Sr_xFe_{1-y}M_yO_{3-\delta}$ (M = Cr, Ni and Cu; x = 0.3-0.7; y = 0.0-0.3) ที่สังเคราะห์ด้วยวิธีซิเตรตประยุกต์ แสดงเฟสเดียวและโครงสร้างแบบลูกบาศก์ ABO_3 ยกเว้น $La_{0.4}Sr_{0.6}Fe_{0.7}Ni_{0.3}O_{3-\delta}$ ที่ประกอบด้วยสารอื่นปน จากการศึกษาโดยกล้องจุลทรรศน์อิเล็กตรอนแบบส่องกราด แสดงว่าลักษณะสัณฐานของแผ่นเพอรอฟสไกต์ออกไซด์นี้มีโครงสร้างระดับไมโครที่หนาแน่น ขนาดเกรนของ $La_{1-x}Sr_xFe_{1-y}M_yO_{3-\delta}$ เพิ่มขึ้นตามปริมาณสตรอนเทียมที่เติมเข้าไป ค่าการนำไฟฟ้าของสารเพอรอฟสไกต์ออกไซด์นี้ที่วัดโดยเทคนิคขั้วกระแสตรงชนิด 4 ขั้ว แสดงว่าค่าการนำไฟฟ้าของ $LaFeO_3$ เพิ่มขึ้นด้วยการเติมสตรอนเทียม นิกเกิล และคอปเปอร์ ซึ่งค่าการนำไฟฟ้าของ $La_{0.4}Sr_{0.6}Fe_{0.8}Ni_{0.2}O_{3-\delta}$ มีค่าสูงสุดที่ 495.46 ซีเมนต์ต่อเซนติเมตร ณ 550 องศาเซลเซียส ในการวิเคราะห์การขยายตัวทางความร้อนนั้น ค่าสัมประสิทธิ์การขยายตัวทางความร้อนของ $La_{1-x}Sr_xFeO_{3-\delta}$ เพิ่มขึ้นด้วยการเติมสตรอนเทียมที่ตำแหน่ง A และโครเมียม นิกเกิล และคอปเปอร์ที่ตำแหน่ง B การวัดค่าการซึมผ่านของออกซิเจนแสดงให้เห็นว่าการเคลือบตัวเร่งปฏิกิริยาพื้นผิวบนเมมเบรน สามารถเพิ่มค่าการซึมผ่านออกซิเจนของเมมเบรนได้ โดยเฉพาะการเคลือบตัวเร่งทั้งสองด้าน โดยที่อุณหภูมิ 1,000 องศาเซลเซียสค่าการซึมผ่านออกซิเจนสูงสุดเท่ากับ 72.51×10^{-8} โมลต่อวินาทีต่อตารางเซนติเมตร วัดได้จากเมม เบรนของ $La_{0.4}Sr_{0.6}Fe_{0.8}Ni_{0.2}O_{3-\delta}$ ที่ทาด้วย $La_{0.4}Sr_{0.6}Fe_{0.8}Ni_{0.2}O_{3-\delta}$ ที่มีลักษณะเป็นรูพรุนทั้งสองด้าน

สาขาวิชา ปิโตรเคมีและวิทยาศาสตร์พอลิเมอร์ ลายมือชื่อนิสิต .....

ปีการศึกษา 2552 ลายมือชื่อ อ.ที่ปรึกษาวิทยานิพนธ์หลัก .....

ลายมือชื่อ อ.ที่ปรึกษาวิทยานิพนธ์ร่วม .....

5072279023 : MAJOR PETROCHEMISTRY AND POLYMER SCIENCE
KEYWORDS : PEROVSKITE OXIDE / LSF / ELECTRICAL CONDUCTIVITY / THERMAL EXPANTION COEFFICIENT / OXYGEN PERMEATION

AUNPAJSUDA CHAIYAWONG : PREPARATION OF $La_{1-x}Sr_xFe_{1-y}M_yO_{3-\delta}$ PEROVSKITES FOR SOLID OXIDE FUEL CELL MATERIALS. THESIS ADVISOR : ASST. PROF. ORAVAN SANGUANRUANG, Ph.D., THESIS CO-ADVISOR : PARICHATR VANALABHPATANA, Ph.D., 105 pp.

The influences of Sr-doping at A-site and Cr-, Ni- and Cu-doping at B-site on the structures and properties of $LaFeO_3$ perovskites were studied. Confirmed by XRD technique, $La_{1-x}Sr_xFe_{1-y}M_yO_{3-\delta}$ (M = Cr, Ni and Cu; x = 0.3-0.7; y = 0.0-0.3) synthesized by the modified citrate method showed single-phase and ABO_3 cubic structure, except that $La_{0.4}Sr_{0.6}Fe_{0.7}Ni_{0.3}O_{3-\delta}$ contained impurity phase. Using SEM, the morphology of the perovskite oxide discs revealed dense microstructures. The grain sizes of $La_{1-x}Sr_xFe_{1-y}M_yO_{3-\delta}$ were found to increase with the doped Sr content. The perovskite oxide conductivity measured by DC-4 probe technique displayed that the electrical conductivity of $LaFeO_3$ was improved by the addition of Sr, Cu and Ni. The specific conductivity of $La_{0.4}Sr_{0.6}Fe_{0.8}Ni_{0.2}O_{3-\delta}$ reached the maximum value of 495.46 S/cm at 550 °C. For thermal expansion analysis, the TEC values of $La_{1-x}Sr_xFeO_{3-\delta}$ increased with doping Sr at A-site and doping Cr, Ni and Cu at B-site. Oxygen permeation measurement proved that coating surface catalyst on doped $LaFeO_3$ membrane can enhance the membrane oxygen permeation flux, especially with both-sides catalyst coating. At 1,000 °C, the highest oxygen permeating flux of 72.51×10^{-8} mol/s*cm^2 was obtained from $La_{0.4}Sr_{0.6}Fe_{0.8}Ni_{0.2}O_{3-\delta}$ membrane coated with porous $La_{0.4}Sr_{0.6}Fe_{0.8}Ni_{0.2}O_{3-\delta}$ on both sides.

Field of Study : Petrochemistry and Polymer Science Student's Signature .....
Academic Year : 2009 Advisor's Signature .....
Co-Advisor's Signature .....

ACKNOWLEDGEMENTS

The success of this thesis can be attributed to the extensive support and assistance from Assistant Professor Dr. Oravan Saguanruang and Dr. Parichatr Vanalabhpatana. I deeply thank them for their valuable advice, assistance, guidance, and generous encouragement throughout the course of this research.

I would like to gratitude Associate Professor Dr. Sirirat Kokpol, Associate Professor Dr. Wimonrat Trakarnpruk and Associate Professor Preecha Phahonthep as the chairman and members of this thesis committee, respectively, for all of their kindness and useful advice in the research.

I would like to gratefully thank Dr. Thanakorn Wasanapiarnpong in Department of Material Science, Faculty of Science, Chulalongkorn University for supporting many instruments. Moreover, I would like to thank Department of Chemistry, Faculty of Science, Chulalongkorn University for the valuable knowledge and experience. In addition, Thailand Japan Technology Transfer Project supported a loan by Japan Banks for International Cooperation (TJTTP-JBIC) for instrument support and National Center of Excellence for Petroleum, Petrochemicals, and Advanced Materials (NCE-PPAM). Furthermore, This thesis could not have been completed without generous help of the staff members of the Material Chemistry and Catalysis Research Unit for their kind assistance and generosity.

For all of my friends, I greatly appreciate their help and encouragement throughout the course of my research and study.

Finally, I would like to express my deepest gratitude to my family for their entirely care and support. The usefulness of this thesis, I dedicate to my family and all teachers who have taught me since my childhood.

CONTENTS

Page

Page

Page

Page

LIST OF TABLES

Page

LIST OF FIGURES

Page

Page

Page

LIST OF SCHEMES

LIST OF ABBREVIATIONS

LSF	$La_{1-x}Sr_xFeO_{3-\delta}$
LSCo	$La_{1-x}Sr_xCoO_{3-\delta}$
LSCu	$La_{1-x}Sr_xCuO_{3-\delta}$
LSM	$La_{1-x}Sr_xMnO_{3-\delta}$
LSCo64	$La_{0.6}Sr_{0.4}CoO_{3-\delta}$
LSFNi4682	$La_{0.4}Sr_{0.6}Fe_{0.8}Ni_{0.2}O_{3-\delta}$
C1-LSCo	membrane coated with $La_{0.6}Sr_{0.4}CoO_{3-\delta}$ on the air side
C2-LSCo	membrane coated with $La_{0.6}Sr_{0.4}CoO_{3-\delta}$ on both air and He sides
C1- LSFNi4682	membrane coated with $La_{0.4}Sr_{0.6}Fe_{0.8}Ni_{0.2}O_{3-\delta}$ on the air side
C2- LSFNi4682	membrane coated with $La_{0.4}Sr_{0.6}Fe_{0.8}Ni_{0.2}O_{3-\delta}$ on both air and He sides
MIEC	Mixed ionic and electronic conductor
SOFCs	Solid oxide fuel cells
XRD	X-ray diffractrometry
SEM	Scanning electron microscopy
TEC	Thermal expansion coefficient
M	metal
^oC	degree Celsius
^oF	degree Fahrenheit
K	Kelvin
k	kilo
%	percent
r_x	ionic radii of x
a,b,c	unit lattice parameter
t	tolerance factor
δ	oxygen non-stoichiometry
L	length
I	current
T	thickness

V	voltage
W	width
ρ	Specific resistance
R	the universal gas constant
F	the faraday constant
σ	Specific conductivity
Ω	Ohm
min	minute
h	hour
g	gram
mg	milligram
ml	milliliter
mm	millimeter
cm	centimeter
nm	nanometer
Å	Angstrom

CHAPTER I

INTRODUCTION

Nowadays, global demand of energy is increasing but petroleum fuels are limited. This event is established energy supply and use problems. Moreover, it is related to increasing environmental problems such as global warming, air pollution and ozone depletion. Therefore, the development of new power generation technologies will become increasingly important. Indeed, energy is one of the main factors that must be considered in discussions of sustainable development. In response to the critical need for a cleaner energy technology, some potential solutions have evolved, including energy conservation through improved energy efficiency, reduction in the consumption of fossil fuels, and an increase in the supply of environmental-friendly energy, such as renewable sources and fuel cells. Solid oxide fuel cells (SOFCs), one type of fuel cells, is one of the most efficient and environmental-friendly technologies available for generating power from hydrogen, natural gas, and other renewable fuels. Large-scale utility based SOFC power generation systems have reached pilot-scale demonstration stages in the US, Europe and in Japan. Small-scale SOFC systems are being developed for military, residential, industrial and transportation applications.

1.1 Fuel cells

A fuel cell is an energy conversion device that converts the chemical energy of a fuel gas directly to electrical energy and heat without the need for direct combustion as an intermediate step, giving much higher conversion efficiencies than conventional thermomechanical methods. The operating principles of fuel cells are similar to those of batteries, i.e., electrochemical combination of reactants to generate electricity, a combination made of a gaseous fuel (hydrogen) and an oxidant gas (oxygen from the air) through electrodes and via an ion conducting electrolyte. However, unlike a battery, a fuel cell does not run down or require recharging. A fuel cell operates as long as both fuel and oxidant are supplied to the electrodes and the influence it exerts on the surrounding environment is negligible.

Fuel cells are generally classified by the chemical characteristics of the electrolyte used as the ionic conductor in the cell, as summarized in Table 1.1. SOFC technology is the most demanding that arise from:

- SOFCs are the most efficient fuel cell electricity generators currently being developed world-wide.
- SOFCs are flexible in the choice of fuel.
- SOFCs have a modular and solid state construction and do not present any moving parts, thereby are quiet enough to be installed indoors.
- The high operating temperature of SOFCs produces high quality heat byproduct which can be used for co-generation or for use in combined cycle applications.
- SOFCs do not contain noble metals that could be problematic in resource availability and price issue in high volume manufacture.
- SOFCs do not have problems with electrolyte management (for example, liquid electrolytes which are corrosive and difficult to handle).
- SOFCs have extremely low emissions by eliminating the danger of carbon monoxide in exhaust gases, as any CO produced is converted to CO_2 at the high operating temperature.
- SOFCs have a potential long life expectancy of more than 40000-80000 h.

Table 1.1 Comparison of fuel cells technologies [1]

Fuel Cell Type	Common Electrolyte	Operating Temperature	System Output	Electrical Efficiency	Combined Heat and Power (CHP) Efficiency
Polymer Electrolyte Membrane (PEM)	Solid organic polymer poly - perfluorosulfonic acid	50 - 100 °C 122 - 212 °F	< 1kW - 250kW	53-58% (transportation) 25-35% (stationary)	70-90% (low-grade waste heat)
Alkaline (AFC)	Aqueous solution of potassium hydroxide soaked in a matrix	90 - 100 °C 194 - 212 °F	10kW - 100kW	60%	> 80% (low-grade waste heat)
Phosphoric Acid (PAFC)	Liquid phosphoric acid soaked in a matrix	150 - 200 °C 302 - 392 °F	50kW - 1MW	> 40%	> 85%
Molten Carbonate (MCFC)	Liquid solution of lithium, sodium, and/or potassium carbonates, soaked in a matrix	600 - 700 °C 1112 - 1292 °F	< 1kW - 1MW	45-47%	> 80%
Solid Oxide (SOFC)	Yttria-stabilized zirconia	600 - 1000 °C 1202 - 1832 °F	< 1kW - 3MW	35-43%	< 90%

1.2 Solid oxide fuel cells

A SOFC system usually utilizes a solid ceramic as the electrolyte and operates at extremely high temperatures (600-1000 °C). SOFCs differ in many respects from other fuel cell technologies. First, they are composed of all-solid-state materials. Second, the cells can operate at temperatures as high as 1000 °C, significantly hotter than any other major category of fuel cell. Third, the solid state character of all SOFC components means that there is no fundamental restriction on the cell configuration. Cells are being constructed in two main configurations as shown in Figure 1.1, i.e., tubular cells or rolled tubes, such as those being developed at Westinghouse Electric Corporation since the late 1950s, and a flat-plates configuration adopted more recently by many other developers and employed today by the electronics industry.

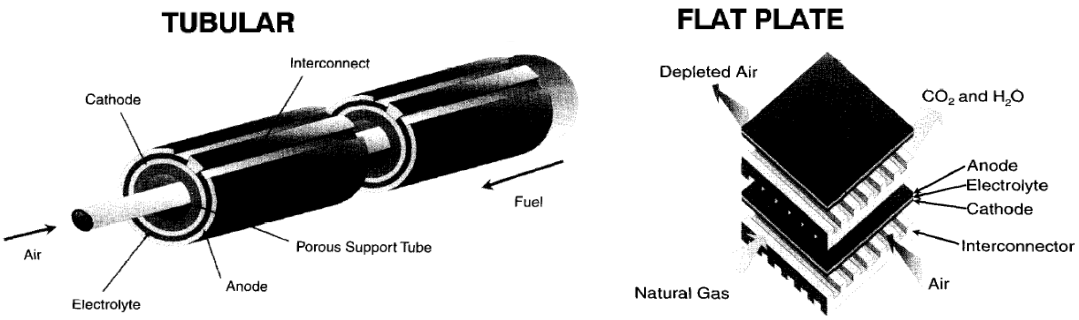

Figure 1.1 Tubular and flat-plates Solid oxide fuel cell [2].

1.2.1 Operation of solid oxide fuel cells

A SOFC consists of two electrodes sandwiched around a ceramic electrolyte. Hydrogen is fed into the anode of the fuel cell and oxygen (from the air) enters the cell through the cathode. At the cathode, the oxygen molecules are split into two oxygen ions. The oxygen ions are diffused through the electrolyte and combine with hydrogen at the anode, releasing electrons. The electrons transport through the anode to the external circuit, providing a source of useful electrical energy in an external circuit. The only byproduct of this process is a pure water molecule (H_2O) and heat, as shown in Figure 1.2.

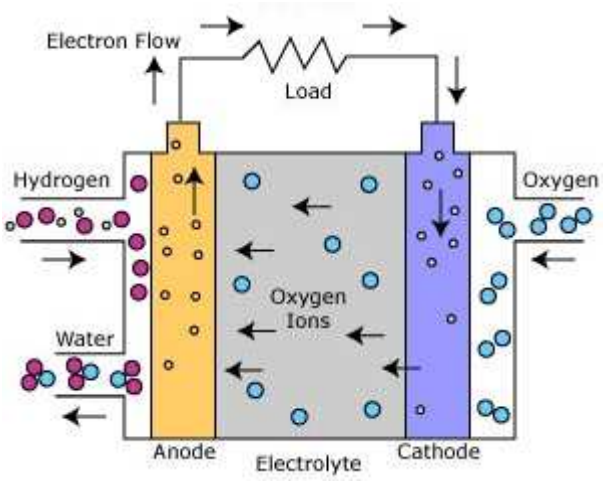

Figure 1.2 Operating of solid oxide fuel cells [3].

The solid oxide fuel cells reactions:

anode side:

$$H_2 + O^{2-} \longrightarrow H_2O + 2e^- \quad (1.1)$$

cathode side:

$$½O_2 + 2e^- \longrightarrow O^{2-} \quad (1.2)$$

the overall cell reaction:

$$H_2 + ½O_2 \longrightarrow H_2O \quad (1.3)$$

1.2.2 Components of solid oxide fuel cells

A SOFC is mainly composed of two electrodes (the anode and the cathode) and a solid electrolyte. Each component of the SOFC serves several functions and must therefore meet certain requirements such as [4]:

(a) high stability (chemical, phase, morphological and dimensional)
(b) high conductivity
(c) chemical compatibility with other components
(d) similar thermal expansion to avoid cracking during the cell operation
(e) dense electrolyte to prevent gas mixing
(f) porous anode and cathode to allow gas transport to the reaction sites
(g) high strength and toughness properties
(h) compatibility at higher temperatures at which the ceramic structures are fabricated
(i) low cost
(j) relatively simple fabrication

1.2.2.1 Electrolyte

The electrolyte determines the operating temperature of the fuel cell and is used to prevent the two electrodes to come into electronic contact by blocking the electrons. It also allows the flow of charged ions from one electrode to the other to maintain the overall electrical charge balance. The most common non-porous electrolyte has been the stabilized zirconia with conductivity based on oxygen ions (O^{2-}), especially yttria-stabilized zirconia (Y_2O_3-stabilized ZrO_2).

The properties of materials used as electrolytes in SOFCs must be [5]:

(a) ionically conductive
(b) electronically insulating
(c) chemically stable at high temperatures
(d) chemically stable in reducing and oxidizing environments
(e) gas tight/free of porosity
(f) production as a uniformly thin layer (to minimize ohmic losses)
(g) thermal expansion that matches electrodes

1.2.2.2 Anode

The anode disperses the hydrogen gas equally over its whole surface and conducts the electrons (from hydrogen molecule), to be used as a useful power in the external circuit. SOFC anodes are fabricated from composite powder mixtures of electrolyte material, which serves to inhibit sintering of the metal particles and to provide a thermal expansion coefficient comparable to those of the other cell materials. The anode structure is fabricated with a porosity of 20-40% to facilitate mass transport of reactant and product gases. Design requirements for the anode are [5]:

(a) electrically conductive
(b) high electrocatalytic activity
(c) stable in a reducing environment
(d) can be made thin enough to avoid mass transfer losses, but thick enough to provide area and distribute current
(e) able to provide mechanical support to electrolyte and cathode if the cell is anode supported
(f) thermal expansion coefficient similar neighboring cell component

(g) chemically compatible with neighboring cell component
(h) has a fine particle size
(i) able to withstand low vapor pressures (will not cause unwanted reactions)

1.2.2.3 Cathode

The cathode distributes the oxygen fed to it onto its surface and conducts the electrons back from the external circuit where they can recombine with oxygen ions, passed across the electrolyte, and hydrogen to form water. Perovskite-type lanthanum strontium manganite, $LaSrMnO_3$ (LSM) and lanthanum calcium manganite, $LaCaMnO_3$ (LCM) offer excellent thermal expansion match with zirconia electrolytes and provide good performance at operating temperatures above 800°C. Similar to the anode, the cathode is a porous structure that must permit rapid mass transport of reactant and product gases. The cathode has to meet the following requirements [5]:

(a) high electronic conductivity
(b) chemically compatible with neighboring cell component
(c) can be made thin and porous (thin enough to avoid mass transfer losses, but thick enough to provide area and distribute current)
(d) stable in an oxidizing environment
(e) catalyze the dissociation of oxygen
(f) high ionic conductivity
(g) adhesion to electrolyte surface
(h) thermal expansion coefficient similar to other SOFC materials

1.2.2.4 Interconnection

In SOFCs, interconnect is the electric link to the cathode and protects the electrolyte from the reducing reaction. The requirements of the interconnection are the most severe of all cell components and include the following [5]:

(a) high temperature oxidation and reduction resistance (simultaneous fuel and oxidant gas exposure)
(b) stable under multiple chemical gas streams
(c) very high electrical conductivity

(d) high density with “no open porosity”
(e) strong and high creep resistances for planar configurations
(f) good thermal conductivity
(g) phase stability under temperature range
(h) resistant to sulfur poisoning, oxidation and carburization
(i) low materials and fabrication cost
(j) matching thermal expansion to other cell components

1.3 Perovskite [6]

Perovskite is named for a Russian mineralogist, Count Lev Aleksevich von Perovski. The mineral was discovered and named by Gustav Rose in 1839 from samples found in the Ural Mountains. Its most common mineral, perovskite, lends its name to this important group of oxides. The importance of this group is two fold. First, every member of this group has rare earth metals as trace elements in their structures and second, the structure of this group is unique and many ceramic, synthetic and useful substances can be created using the structure. Perovskite exhibits both electronic and ionic conductivities (Mixed ionic electronic conductors; MIEC), making them promising candidate materials for Solid oxide fuel cells.

1.3.1 Structure of perovskite oxides

The general formula of perovskite oxides is ABO_3, where A is the larger cation (such as an alkaline earth cation) and B is the smaller cation (such as a transition metal cation). The ideal perovskite structure ABO_3 is primitive cubic, as shown in Figure 1.3. The perovskite structures can be appropriately modified by partial substitution of A or B cations by other cations with different ionic radius or valence numbers.

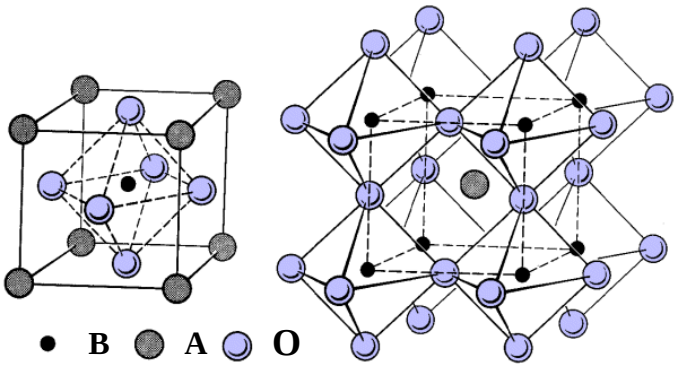

Figure 1.3 ABO_3 ideal perovskite structure [7].

The formation of perovskite structure requires ionic radii fitting to the lattice. This can be illustrated for the perovskite structure by deriving a relationship between the radii of the various ions. Figure 1.4 shows the relationship between ionic radii in the perovskite structure.

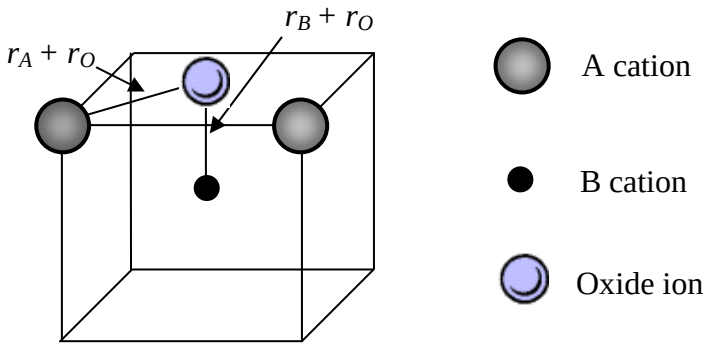

Figure 1.4 The relationship of ionic radii in perovskite structure (Where r_A , r_B and r_O are the ionic radii of A, B and oxide ions, respectively).

Where the atoms are touching one another, the B-O distance is equal to $a/2$ (a is the cubic unit cell parameter) while the A-O distance is $a/\sqrt{2}$ and the following relationship between the ionic radius holds shown in Equation 1.6.

$$a = 2\times(B-O) = 2(r_B + r_O) \tag{1.4}$$

and

$$a = \frac{1}{\sqrt{2}} \times 2\times(A-O) = \sqrt{2}(r_A + r_O) \tag{1.5}$$

hence,

$$2\,(r_B + r_O) = \sqrt{2}\,(r_A + r_O) \tag{1.6}$$

Goldschmidt introduced a tolerance factor (*t*), describing the relationship between symmetry and ionic radii in the perovskites. It can be defined as:

$$t = \frac{(r_A + r_O)}{\sqrt{2}(r_B + r_O)} \tag{1.7}$$

The ideal perovskite is the cubic structure with the tolerance factor close to 1.0 at high temperature. The perovskite structure is stable in the range $0.75 < t < 1.0$, and is cubic in the range $t > 0.95$. Deviations from the ideal structure are well known as orthorhombic, rhombohedral, tetragonal, monoclinic and triclinic symmetry. The distorted structure may exist at room temperature but it transforms to the cubic structure at high temperature.

1.3.2 Nonstoichiometry in perovskites [8]

Besides the ionic radii requirements, another condition to be fulfilled is electroneutrality, i.e., the sum of charges of A and B equals the total charge of oxygen anions (such as form $A^{1+}B^{5+}O_3$, $A^{2+}B^{4+}O_3$ or $A^{3+}B^{3+}O_3$). In addition, partial substitution of A and B ions is allowed, thus yielding a plethora of compounds while preserving the perovskite structure. However, deficiencies of cations at the A- or B-sites or of oxygen anions are frequent which results in defective perovskites.

1.3.2.1 Oxygen nonstoichiometry

Oxygen vacancies are accomplished by substituting ions of similar size but different valence. Oxygen vacancies are more common than involving cationic vacancies. The former composition can be considered as an anion-deficient perovskite with one-sixth of the oxygen ions being vacant.

However, oxygen excess nonstoichiometry in perovskite oxides is not as common as anion-deficient nonstoichiometry probably because introduction of interstitial oxygen in perovskite structure is thermodynamically unfavorable. There are two reasons occur of oxygen excess nonstoichiometry. First, because the trivalent cation vacancies cause a large electronic imbalance and local lattice distortion, it does not stay close to each other. Second, with the formation of cation vacancies, a nonbonding O2p level is formed by the oxide ions around the vacancies. This nonbonding O2p level serves as the hole-trap. Applying this structure,

nonstoichiometry of the oxygen-deficient composition was explained by the random distribution of oxide-ion vacancies. The general formula of oxygen-deficient perovskite oxides is $ABO_{3-\delta}$ or $ABO_{3+\delta}$.

1.3.2.1 Cation nonstoichiometry

An oxygen excess can also readily be achieved in perovskites that are structurally deficient in oxygen because of cation nonstoichiometry.

B-site vacancies in perovskite oxides are not so common, although a few examples displaying this type of defect are known. This is a consequence of the fact that the B-site vacancies are not thermodynamically favored because of the large charge and the small size of the B cations. Other perovskites exhibit A-site vacancies. This is because the BO_3 array in the perovskite structure forms a stable network, the large A cation at 12 coordinated sites can be partially missing.

1.3.3 Properties of perovskites

1.3.3.1 Electrical conductivity

The electrical conductivity of perovskites also shows wide variations. Several compounds have been used for their dielectric properties, while others show metallic conductivity, although most are semiconductors. As for other compounds, the electrical behavior in perovskites depends on the outermost electrons, which may be localized at specific atomic sites or may be collective. Since localized electrons may carry a spontaneous moment, there is a strong correlation between the electrical and magnetic properties of perovskites. Rare earth perovskites containing transition ions show widely differing electrical properties.

Furthermore, the electronic conduction can be n-type or p-type. In the case of the first type of conductors, the formation of oxygen vacancies (or interstitial metal ions) is complemented by the formation of electrons which is responsible for electronic conductivity. This type of electronic conductor is generally called an n-type conductor. The second type of conductors involves the creation of electron holes (positive electronic defects) to complement the formation of metal vacancies (or interstitial oxygen ions). This type of electronic conductor is termed a p-type conductor. In n-type conductors, neutral levels near the conduction bands are ionized to free an electron into a conduction band. The electron then acts as an electronic

species. In the p-type conductors however, neutral levels near the valence band may be ionized to accept the electron, leaving the so-called electron hole in the valence band, which then acts as an electronic species in this typical material. The concept of the energy bands is therefore required to have a good understanding of the concept of electron and electron holes [9, 10]. Another contribution to electronic conductivity can arise from the presence of a multivalent cation in mixed oxides. This extrinsic factor is assumed to occur via a small polaron mechanism, involving the hopping of electrons between cations with different valence states and commonly called the "hopping conductivity contribution" [11, 12].

The electrical conductivity of perovskite was measured by using DC 4-probe or "Kelvin" measurement.

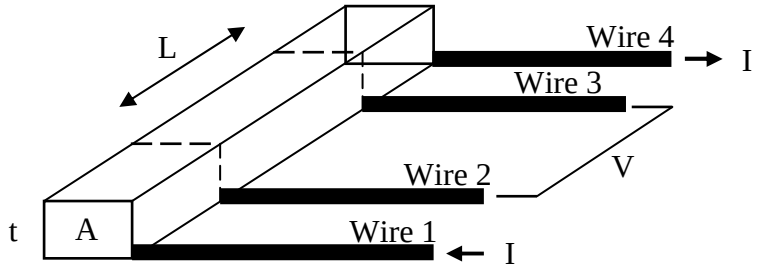

Figure 1.5 DC 4-probe method.

The measurement method then includes a forced current I through the outer wires 1 and 4 and a measurement of the voltage drop over wire 2 and 3, using a very high ohmic measurement device, so that the current flowing through wire 2 and 3 nearly zero. In that case the individual, additional contact resistance does not play a role as it cancels out of the equation. To study the behavior of the structure an I/V curve is generated, typically in the μA to the mA range. If the graph shows a straight line, the structure behaves as an Ohmic resistor. If assume that the resistance of a structure to be R then the following applies:

$$R = \frac{\rho L}{A} \tag{1.8}$$

Where L = the length of the structure (m)

A = the area (width x thickness) of the cross section (m^2)

ρ = the specific resistivity (Ω.m of the practical unit μΩ.cm)

1.3.3.2 Mixed ionic-electronic conductors

The perovskite oxides exhibit both ionic and electronic conductivity. These material oxides may show both high oxygen ion conductivity due to the high oxygen vacancy concentration in the structure, and a high electronic conductivity due to the mixed-valence state. For example $La_{1-x}Sr_xBO_{3-\delta}$ in this case [13], when the B ions can take a mixed-valence state, charge neutrality is maintained by both the formations of oxygen vacancies and a change in the valence state of the B ions. The concentration of oxygen vacancies can also be increased by mild B-site ion substitution, such as Cu and Ni ions which naturally take the divalent oxidation state [14]. If the valence state of the B ions is fixed, neutrality is maintained only by the formation of oxygen vacancies. The oxides may be predominantly ionic conductors.

1.3.3.3 Oxygen permeation

The mixed conductive perovskite membrane can be an intrinsically mixed conductor or a mixture of an oxide ion conductor and an electronic phase. Because of their properties, these materials could be developed as membranes for oxygen separation. There are two concepts of oxygen separators using a mixed ionic-electronic conducting membrane: current driven membranes and pressure driven membranes. In the first case, under an electrical field, molecular oxygen is dissociated at the cathode into oxide ions which migrate through the membrane and recombine as O_2 at the anode. This allows the production of given amounts of oxygen under pressure. In the second case, a difference of oxygen partial pressure between an oxygen rich compartment and an oxygen poor compartment is the driving force for the migration of O_2 from the rich to the oxygen poor compartment, as illustrated in Figure 1.6.

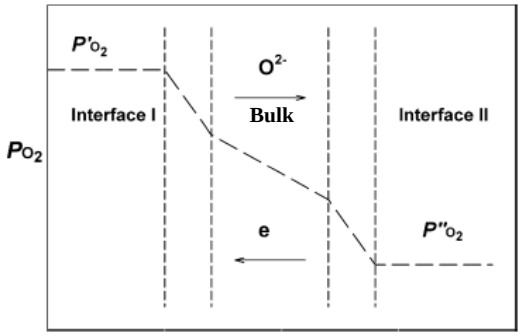

Figure 1.6 Different sections involved in oxygen transport during oxygen permeation. (The membrane is in the middle, high oxygen pressure zone ($P'o_2$) is in the left of the membrane and low oxygen pressure zone ($P''o_2$) is in right sides of the membrane) [15].

The driving force for oxygen transport is the difference of oxygen partial pressures of both sides. The oxygen anions permeate from the high to the low partial pressure side, while overall charge neutrality was maintained by a counterbalancing flux of electrons (and/or electron holes). Mechanism for oxygen permeation through a mixed ionic-electronic conducting membrane can be described as follows [16, 17]:

1. mass transfer of gaseous oxygen from the gas phase with high oxygen partial pressure to the membrane surface
2. reaction between the molecular oxygen and oxygen vacancies at the membrane surface
3. dissociation and electron transfer, giving chemisorbed oxygen species
4. incorporation in membrane surface layer
5. diffusion of lattice defects to interior
6. oxygen vacancy bulk diffusion across the membrane
7. association and electron transfer, forming chemisorbed oxygen species
8. desorption from the surface
9. mass transfer of oxygen from the membrane surface to the gas phase with low oxygen partial pressure

When the oxygen transport in a membrane is at steady state, the oxygen permeation flux can be calculated by using the Wagner equation [18]:

$$Jo_2 = \frac{RT}{(4F)^2}\frac{\sigma_{amb}}{L}\ln\frac{P'o_2}{P''o_2} \quad (1.9)$$

Where $P''o_2$ and $P'o_2$ stand for the oxygen partial pressure in the higher and lower oxygen partial pressure compartment, respectively, L is the sample thickness, T is the temperature, R is the universal gas constant and F is the faraday constant. The ambipolar conductivity is defined as:

$$\sigma_{amb} = \frac{\sigma_e\sigma_i}{(\sigma_e + \sigma_i)} \quad (1.10)$$

Where σ_e is the electronic contribution and σ_i is the ionic contribution to the total conductivity.

There is no need for an external current but the membrane must be a mixed conductor to allow the reverse flow of the electrons needed for the oxygen dissociation. The expected oxygen permeation flux in such membranes depends therefore on the difference of oxygen partial pressure between the two compartments, on the membrane thickness and on the ionic and electronic conductivity of the membrane.

- *Modification of membrane surface*

When the oxygen flux is determined by the oxygen exchange reaction, the modification of both membrane "flat" surfaces can lead to the strong enhancement of the oxygen permeation. Successful enhancement was reached by simple roughening leading to higher surface/volume ratios [19]. Further enhancement is predicted by modeling a layered structure with graded porous support, dense membranes and a porous functional top layer [20]. The available surface area for oxygen exchange (adsorption, dissociation and oxidation) can be increased in a porous top coating by promoting the formation of a mesoporous pore system. Other options include the use of the membrane material with a high ionic conductivity as porous coating and subsequently modifying the porous surface by (i) impregnation with noble metals or catalytically active transition metals and (ii) coating of the

porous structures using colloidal suspensions of nanoparticles of active oxides in the oxygen activation.

1.3.4 Perovskite synthesis

As a summary, about five synthesis methods have been employed quite extensively to produce mixed oxide compounds [21].

1.3.4.1 Solid-state reaction

The most common synthesis process to produce conventional powders employs the thorough reaction of mixed oxides, carbonates, hydroxides or salts and firing at temperatures of at least two thirds of the melting point for periods up to 10 h [22]. The size of the particles is controlled by laborious mechanical mixing of starting materials and grinding processes. The homogeneity and purity of the powder is considered poor, not to mention its broad particle size distribution [21]. Apart from the fact that this process has a high-energy consumption because of the high temperature, other problems may arise when one component in the compounds (i.e. toxic Pb) vaporizes during the long reaction time [22].

1.3.4.2 Co-precipitation

One of the oldest techniques comprised of mixing an aqueous solution containing the desired cations and another solution acting as a precipitation agent. Filtration, drying and thermal decomposition followed to acquire desired products. The desired products and their physical properties are adjusted using pH, mixing rates, temperatures and concentration. Usually, the morphology, purity and composition control achieved is good, although different precipitation rates sometimes result in inhomogeneities. A doping agent may be added to assist in reaching the compositional homogeneity. The resultant compound requires a lower sintering temperature than those employed in the conventional powder method [21] due to the high dispersion of the different metals in the precipitate, and its particle size is typically in the range of few nanometers, which is achieved by careful precipitation using suitable surfactants and capping agents [23]. A careful control of pH and precipitation temperature is substantial to obtain material with an exact stoichiometric condition.

1.3.4.3 Sol-gel techniques

The sol-gel technique involves the production of an amorphous like gel, followed by dehydration at low temperature [24]. This technique delivers high purity and excellent composition control.

- *Alkoxide route.*

In here, all the starting materials employed for sol−gel preparation are in the form of metal alkoxides. Metal alkoxides are readily hydrolyzed and condensed to hydroxides or oxides. Aliphatic alcohol as a by-product is removed by volatilization and several complex perovskites have been synthesized using this technique [25]. A perovskite structure can be acquired at far lower temperatures than that needed using conventional powder methods. Usually the hydrolysis reaction is carried out within a mixture of polar and non-polar solvents [21].

- *Alkoxide-salt route.*

Metal alkoxides of groups I and II are solid and non-volatile, which make them difficult to purify by distillation. Metal salts or hydroxides are generally used in this case. This route comprises the preparation of desired alkoxides and then adding the metal salts in an alcoholic solution or an aqueous solution. In this process, hydrolysis must be controlled due to different reaction rates among the mixture of alkoxides and salts [21].

- *EDTA, citrate and modified citrate route.*

This route is very popular and has been utilized extensively due to its advantages such as carbonate-free and chemically homogeneous final oxide compounds with a high relative density. Citric acid, ethylenediaminetetraacetic acid (EDTA) or glycine can be used as chelating agent. As an example, investigation on the effect of different ligands on perovskite structure evolution and sintering temperature in strontium cerates-based ceramic powder showed that citric acid was most effective for this particular compound [26]. This route involves complexation of metal ions in EDTA/citric acid, followed by evaporation of water solvent and thermal decomposition of the complex with subsequent formation of perovskite phase. A chelating agent is used to prevent partial segregation of metal components, which

could occur in the case of different stabilities with the metal ions in solution. In some cases [27], a polyol (e.g. ethylene glycol) is added to the reaction batch to promote the polymerization with chelating agent and producing an organometallic polymer, which results in a perovskite precursor after drying and pyrolysis.

Sol-gel process involves producing precursor from citric acid and metal nitrate before thermal decomposition. For example, the production of Sr-substituted $LaMnO_3$ perovskite powder by the amorphous citrate process, obtained the manganese citrate-nitrate precursor as shown in Scheme 1.1 [28].

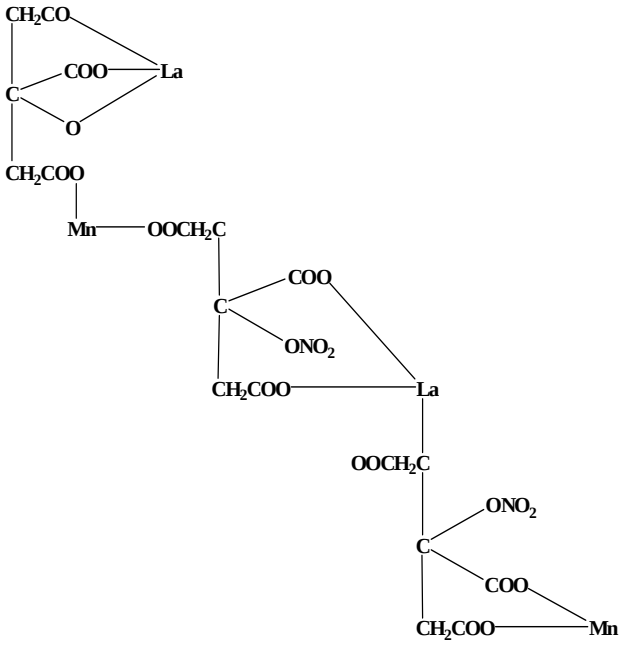

Scheme 1.1 The manganese citrate-nitrate precursor.

In the complex, the lanthanum is triply charged and replaces in normal citrate formation in the hydrogen of three -COOH groups and it replaces in the hydrogen of one -OH group and two -COOH groups. As manganese is divalent state replaces in the hydrogen of two -COOH groups while NO_2 replaces the hydrogen of one -OH group, respectively.

In all cases the minimum amount of citric acid used was that necessary to bond the metals if all the NO_3^- ions were replaced. However, the amounts of metal and citric acid should not less than equimolar. If the high amount of citric acid was used, complex of $Mn(NO_3)_2$ and citrate ion was formed as in Scheme 1.2:

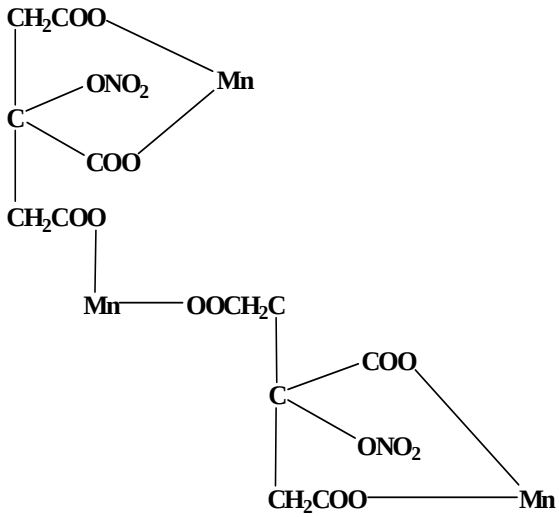

Scheme 1.2 Complex of $Mn(NO_3)_2$ and citrate ion.

The formation of this complex would also liberate NO_3^- groups for each two molecules of $Mn(NO_3)_2$ originally present in solution. The formation of above structure would allow some citric acid, water and nitrate ions to be lost during the preparation of gel. Every three molecules of citric originally present one remains uncombined and may be removed from the mixture by either evaporation or decomposition to yield acetone, carbon dioxide and water during the precursor preparation in the vacuum oven.

1.3.4.4 Hydrothermal synthesis

This synthesis method is applied to produce advanced mixed oxides, a compound with specific characteristics in their composition such as pigments for electronics. This process generally uses temperatures between the boiling point of water and the material's critical temperature (i.e. 374 °C), while the pressure can be as high as 15MPa [29, 30]. Consequently, the calcination step required by other steps discussed above can be eliminated in this case. Hydrothermal synthesis can be used to assist the sol-gel technique in controlling the particle size. The materials used are generally inexpensive, easy to control in terms of its size, shape and stoichiometry. Elimination of impurities associated with milling and other advantages mentioned will result in very fine and highly reactive ceramic powders [21].

1.3.4.5 Spray and freeze drying

Spray drying consists of a rapid vaporization of the solvent in small droplets containing required solutions of cations, whereas freeze drying involves the slow sublimation of the solvent. Excellent impurity and composition control is inherent, leading to homogeneous fine materials. In addition, spray drying is an industrially established process and the manufacture of complex multi-metallic oxides can be scaled up easily. The important steps in the freeze drying are the spraying of fine droplets of solution into liquid nitrogen, and the sublimation of the solvent in the absence of the liquid phase [31].

In summary, the five techniques as mentioned earlier are the most established. The first three have been commercially established, while the last two are still in the demonstration stage. There is a sequential order of improvement in the property of the membranes related to particle size, homogeneity and purity of the desired membranes from conventional powder methods, through co-precipitation, sol-gel, hydrothermal and spray drying method. This is by no means a fast rule, as the oxygen permeation properties will depend on the compound mixture. However, the trend has been established and there is strong technical and experimental evidence to support improvement claims by using more advanced methods as compared to conventional powder technology. Finally, the calcinations temperature is also being lowered in the same sequential order, thus providing savings in this high-energy process, although better methods will usually be accompanied by the higher cost of novel technologies [21].

1.3.5 Calcination [32]

The calcination (also referred to as calcining) is a thermal treatment process applied to ores and other solid materials in order to bring about a thermal decomposition, phase transition, or removal of a volatile fraction. The calcination process normally takes place at temperatures below the melting point of the product materials. The objects of calcination are usually: (1) to drive off water, present as absorbed moisture, as water of crystallization or as water of constitution; (2) to drive off carbon dioxide, sulphl11'dioxide or other volatile constituent; (3) to oxidize a part or the whole of the substance. There are a few other purposes for which calcination is

employed in special cases and these will be mentioned in their propel' places. The process is often called roasting, firing or burning by the workmen.

1.3.6 Sintering [33]

Sintering is the process whereby powder compacts are heated so that adjacent particles fuse together. The fusing of particles results in an increase in the density of the part and hence the process is sometimes called densification. The density of the component can also change during sintering, depending on the materials and the sintering temperature.

When a powder aggregate is sintered, necks form between the particles, and the aggregate may increase in density. The growth of the neck is due to the transport of matter or of the counter-flow of vacancies between the particles and the pores, as shown in Figure 1.7. In crystalline powder, its transport occurs by diffusion (bulk, surface or grain boundary diffusion), whereas in amorphous materials, it occurs by viscous flow.

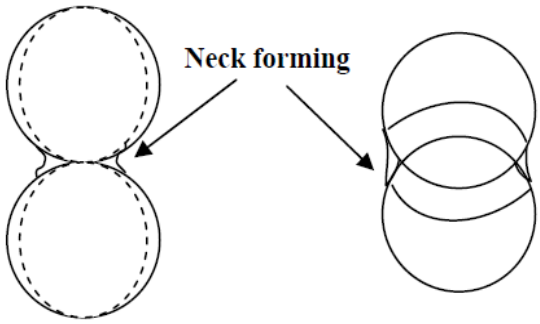

Figure 1.7 Mechanism of sintering.

The sintering process can be distinguished by three stages. The first stage or initial stages during which the necks form at points of particle contact and the particles usually center approach each other. At this stage the individual particles are still distinguishable. The intermediate stage during that the necks become large, resulting in the formation of an interconnected pore structure. The third or the final stages during, the pores become isolated. Elimination of the interconnectivity of pores eliminates surface and vapor transport.

Closed pores isolated from grain boundaries shrink very slowly because grain boundary diffusion is far away from the pores. The growth of grains, therefore, hinders the attainment of theoretical density, since the pore's growth is also enhanced. It is essential, therefore, to retard grain growth so that densification of the compact can continue to the theoretical limit. This is particularly important with the present trend of using ultrafine particles as starting materials for the fabrication of technical ceramics. Surface diffusion becomes important in the case of very fine particles. Grain boundary diffusion and volume diffusion are the main mechanisms causing shrinkage of the neck, whereas surface diffusion does not contribute to any shrinkage. The most important diffusion paths during the sintering of two spheres with a grain boundary are surface diffusion, grain boundary diffusion, volume diffusion from the grain boundary to the neck surface, and volume diffusion from the sphere surface to the neck surface. The sintering rate also affected by the crystallization and growth processes, which occur concurrently. The sintering rate is reduced when there is intensive grain growth because when diffusion forms the pores occurs toward the boundaries of individual grains, the distance over which diffusion occurs with a reduction in pores is determined by the size of the crystals.

1.4 Literature reviews

Priti et al. [34] used three different wet chemistry routes, namely co-precipitation, combustion and sol-gel methods, to synthesize $LaFeO_3$ perovskite. The perovskite synthesized using sol-gel method yields comparatively pure, crystalline phase of $LaFeO_3$ and relatively higher surface area of 16.5 m^2g^{-1} and porosity. The material synthesized using co-precipitation method yielded other phases in addition to the targeted phase. The morphology of perovskite synthesized using co-precipitation method was uniform agglomerates. Combustion method yields flakes type morphology and that of sol-gel method was open pore type morphology. The sol-gel method reported in this study can be alternative low temperature synthesis route for $LaFeO_3$ as to conventional solid-oxide route for obtaining pure perovskite phase with high surface area.

Yu et al. [35] prepared Sr substituted lanthanum metal oxide of $La_{1-x}Sr_xMO_{3-\delta}$ (where M = Co and Cu) in the nanoscale by the polymer modified sol-gel method using polyacrylic acid as a chelating agent. Strontium substituted lanthanum cobaltite

and cuprate can be synthesized in particle size ranging between 25 and 30 nm with good crystallinity. The electrical conductivities of the sintered $La_{1-x}Sr_xCoO_{3-\delta}$ (LSCo) and $La_{1-x}Sr_xCuO_{3-\delta}$ (LSCu) were measured by DC 4-probe method. The electrical conductivities of these two systems decreased with the increasing temperature from room temperature to 95 °C. Both LSCo and LSCu systems exhibit excellent electrical conductivities of more than 1200 S/cm when the strontium addition was more than 25%. The electrical conductivities of strontium doped lanthanum cobaltite and cuprate are rationalized by the formation of electron holes due to the strontium addition.

Simner et al. [36] synthesized the lanthanum ferrite by a glycine-nitrate combustion technique. This study details subtle compositional modifications (marginal A-site deficiencies and Cu B-site dopant additions) to a $La_{0.8}Sr_{0.2}FeO_3$ cathode to enhance sintering below 1000 °C. A total of 1 mol% Cu dopant appears insufficient to facilitate significantly improved densification at low temperatures, whereas increasing the level to 2 mol% adequately lowers the sintering onset temperature. Further sintering improvements are achieved by increasing the Cu content to 5 and 20 mol%. Initial single cell studies utilizing the $(La_{0.8}Sr_{0.2})_{0.98}Fe_{0.98}Cu_{0.02}O_3$ cathode on an anode-supported YSZ cell have indicated high power densities in the range 1.35-1.75 W/cm^2 at 750 °C.

Kharton et al. [37] investigated the effect of doping by iron and nickel in the $LaCo_{1-x-y}Fe_xNi_yO_3$ (x = 0.1-0.2; y = 0.1-0.3) oxide system. XRD analysis of the powders $LaCo_{1-x-y}Fe_xNi_yO_3$ demonstrated that a rhombohedrally distorted perovskite phase was formed. Introducing nickel into the perovskite lattice led to increasing oxygen nonstoichiometry and electrical conductivity and decreasing thermal expansion. Averaged thermal expansion coefficients of the ceramics at 300-1100 K are in the range 18.0-20.8 $\times 10^{-6}$ K^{-1}. The substitution of cobalt with nickel resulted in a sharp increase in the permeation flux due to increasing oxygen nonstoichiometry which is accompanied by an occurrence of the surface exchange limitations of the oxygen transport.

Vitoriano et al. [38] synthesized $La_{0.6}Ca_{0.4}Fe_{1-x}Ni_xO_3$ (x = 0.1, 0.2 and 0.3) (LCFN) by liquid mix method. The XRD patterns were indexed as the orthoferrite similar to that of $LaFeO_3$ having a single phase with orthorhombic perovskite structure. The morphological characterization was performed by scanning electron microscopy (SEM) obtaining a mean particle size less than 300 nm. The

electrochemical measurements showed a better performance of $La_{0.6}Ca_{0.4}Fe_{0.9}Ni_{0.1}O_3$ material using SDC as electrolyte, exhibiting an area specific resistance (ASR) value is 0.88 Ωcm^2 at 800 °C. The DC 4-probe measurement indicated that $La_{0.6}Ca_{0.4}Fe_{0.9}Ni_{0.1}O_3$ exhibits fairly high electrical conductivity over 350 S/cm at T > 500 °C, indicating that these materials are interest to be considered as electrodes in intermediate temperature SOFC devices.

Ishihara et al. [39] prepared Ni-doped $LaGaO_3$-based oxide by a conventional solid state reaction technique. Oxide ionic and partial electronic conduction in Ni-doped $LaGaO_3$-based oxide was investigated. Doping small amount of Ni doped for Ga site of $LaGaO_3$ is useful for improving oxide ion conductivity, since the estimated oxide ion conductivity increased with increasing amount of Ni. This may be resulted from improved mobility of oxide ion. Considering the transport number of oxide ion, the desirable amounts for Ni dopant exist from 5 to 10 mol% for Ga site.

Lu et al. [40] studied crystal structure, oxygen permeability and stability of $Ba_{0.5}Sr_{0.5}Co_{0.8}Fe_{0.1}M_{0.1}O_{3-\delta}$; BSCFMO (where M = Cr, Mn and Zr). These materials possess purely cubic perovskite structure and have single phase when doped by Cr, whereas Mn- and Zr-substituted BSCFO exist impurities. Oxygen permeability across these dense membrane disks were measured under an air/He oxygen partial pressure gradient in the temperature range of 973-1123 K. The results demonstrated that the oxygen permeation fluxes of the BSCFMO membranes increased in the following order: Cr > Zr > Mn. Cr-substituted BSCFO membrane material indicating good stability of oxygen permeation. XRD patterns after treating at 1073 K for 50 h under various oxygen partial pressures ($1\text{-}10^{-5}$ atm), confirmed that the material could keep the purely cubic perovskite structure, and no phase transition and additional peaks were observed, demonstrating its excellent structural stability at 1073 K.

Virattayanon N. [41] synthesized $La_{0.7}Sr_{0.3}Fe_{1-x}M_xO_3$, where M= Ni, Cu, Al and Mn; x = 0.1-0.4, by using modified citrate method. The Cu, Al and Mn specimens showed homogeneous and single phase with cubic perovskite structure. Reduction property was determined by Temperature Programmed Reduction (TPR) technique. The result showed that the reduction process increased with the B site metal doping. The conductivity of $La_{0.7}Sr_{0.3}FeO_3$ species was improved by Cu and Ni doping, especially 30% Ni doping that was the most effective quantity for enhancing the electrical conductivity of $La_{0.7}Sr_{0.3}FeO_3$. At 750 °C, the conductivity of $La_{0.7}Sr_{0.3}Fe_{0.7}$

$Ni_{0.3}O_3$ (650.5 S/cm) was about 3.8 times higher than that of undoped $La_{0.7}Sr_{0.3}FeO_3$ (170 S/cm).

Huang et al. [42] fabricated Sr-doped $LaFeO_3$ (LSF) - yttria-stabilized zirconia (YSZ) composites by impregnation of a porous YSZ matrix with aqueous solutions containing La, Sr and Fe salts, followed by calcinations at various temperatures. Composites of LSF-YSZ were studied for application as high-performance cathodes for solid oxide fuel cells (SOFCs). The electronic conductivity of the 40 wt% LSF-YSZ composite was maximized by calcination at 1123 K. SOFCs prepared with a 40 wt% LSF-YSZ cathode showed improved performance over SOFCs prepared with conventional Sr-doped $LaMnO_3$(LSM)-YSZ cathodes at 973 K, increasing the maximum power density at 973 K in H_2 from 210 to 230 mW/cm^2.

Teraoka et al. [43] investigated the catalytic effects on the oxygen permeation flux under the air/He gradient. The effects of the porous layer coating using $SrCo_{0.8}Fe_{0.2}O_{3-\delta}$ (SCF82) as both membrane and catalyst materials were investigated in this study. The porous catalytic layer of SCF82 perovskites was coated on either surface or both surfaces of the dense membranes of SCF82 perovskites with nearly 1 mm thickness. The permeation flux increased by applying porous catalyst layers, and the largest enhancement was observed with the coating on both sides of the membrane type, followed by the coating either side of the membrane types. The porous layer coating on both sides of the membrane improved the oxygen permeation flux of the uncoated membrane from 0.6 to 1.0 ml/cm^2 min at 1173 K.

Lee et al. [44] modified oxygen permeating property of $LaSrBFeO_3$ (B = Co, Ga) perovskite membrane with $LaSrCoO_3$ surface catalyst. Oxygen permeation fluxes have been investigated as a function of temperature for a mixed ionic-electronic conducting $La_{0.6}Sr_{0.4}Co_{0.2}Fe_{0.8}O_{3-\delta}$ (LSCF) and $La_{0.7}Sr_{0.3}Ga_{0.6}Fe_{0.4}O_{3-\delta}$ (LSGF) membranes. Ga-doped composition showed limited oxygen permeation flux as compared with a Co-containing system. However, modification of both surfaces with catalytically surface-reactive $La_{0.6}Sr_{0.4}CoO_{3-\delta}$ (LSC) made Ga-doped perovskite an excellent oxygen permeable membrane. The oxygen permeation flux of dense LSC-coated LSGF (D-LSC/GF) was about two times (0.15 ml/cm^2 min) higher than that of unmodified LSGF (0.08 ml/cm^2 min), it was not as high as porous LSC coated LSGF (P-LSC/GF) (0.48 ml/cm^2 min) at 950 °C. The difference in the fluxes between D-LSC/GF and PLSC/GF can be explained by the disparity in effective surface area.

These increases in the oxygen fluxes may have been caused both by the increase in the effective surface area and by the increase in surface activity to oxygen dissociation and association according to the application of porous LSC for both surfaces, this promotion is conspicuous if the coating layer is porous, or has larger surface area.

1.5 The objectives of the thesis

The objectives of this study are as follows:

1. To synthesize perovskite powders of $La_{1-x}Sr_xFe_{1-y}M_yO_{3-\delta}$ where M = Cr, Ni and Cu, x = 0.3-0.7 and y = 0.0-0.3.
2. To characterize and study the properties of synthesized perovskite oxides for application in SOFC.
3. To study the effect of the surface catalyst coating on membrane for modified oxygen permeation property.

Firstly, $La_{1-x}Sr_xFe_{1-y}M_yO_{3-\delta}$ (M = Cr, Ni and Cu; x = 0.3-0.7; y = 0.0-0.3) were synthesized. The synthesized perovskite compounds were characterized by XRD and SEM. The electrical conductivity was measured with the DC 4-probe technique and the thermal expansion coefficient (TEC) was determined by dilatometer.

Secondly, $La_{1-x}Sr_xFe_{0.9}M_{0.1}O_{3-\delta}$ (M = Cr, Ni and Cu) with x value exhibiting maximum electrical conductivity value was doped with more metal ratio (y = 0.2-0.3) at B-site. For example, $La_{0.4}Sr_{0.6}Fe_{0.9}M_{0.1}O_{3-\delta}$ showed maximum electrical conductivity value thus $La_{0.4}Sr_{0.6}Fe_{0.8}M_{0.2}O_{3-\delta}$ and $La_{0.4}Sr_{0.6}Fe_{0.7}M_{0.3}O_{3-\delta}$ were synthesized, characterized and their properties were investigated.

Lastly, oxygen permeation property of the prepared perovskite oxide sample with highest electrical conductivity was determined.

CHAPTER II

EXPERIMENTAL

The chemicals, apparatus and experimental procedures including processing of perovskite powders synthesis, perovskite disc preparation and characterization of materials, are described as below:

2.1 Chemicals

The chemicals listed in Table 2.1, were used without further purification.

Table 2.1 Reagents for synthesis of perovskites

Reagents	Formula Weight	Purity%	Company
$La(NO_3)_3 \cdot 6H_2O$	433.02	≥ 99.0	Fluka
$Sr(NO_3)_2$	211.63	≥ 99.0	Fluka
$Fe(NO_3)_3 \cdot 9H_2O$	404.00	98-101	Fluka
$Cr(NO_3)_3 \cdot 9H_2O$	400.15	99.0	Sigma- Aldrich
$Ni(NO_3)_2 \cdot 6H_2O$	290.81	≥ 97	Wako
$Cu(NO_3)_2 \cdot 3H_2O$	241.60	99-104	Fluka
$Co(NO_3)_2 \cdot 6H_2O$	291.03	98-102	APS
$C_6H_8O_7$	192.43	99.5	Riedel-deHaën
$NH_3 \cdot H_2O$	35.05	25	Merck
C_2H_5OH	46.07	30	Merck

2.2 Synthesis of perovskite powder by modified citrate method

The perovskite powders $La_{1-x}Sr_xFe_{1-y}M_yO_{3-\delta}$ (M = Cr, Ni and Cu, x = 0.3-0.7, y = 0.0-0.3) were synthesized by using the modified citrate method. $La(NO_3)_3 \cdot 6H_2O$, $Sr(NO_3)_2$, $Fe(NO_3)_3 \cdot 9H_2O$, $Cr(NO_3)_3 \cdot 9H_2O$, $Ni(NO_3)_2 \cdot 6H_2O$ and $Cu(NO_3)_2 \cdot 3H_2O$ were used as raw materials. The high purity metal nitrates in proper ratio (based on 3 g. of perovskite powder) were partially dissolved in 15 ml D.I. water, and citric acid was added with two times of total metal ions. The above solution was mixed at room temperature under constant stirring for 3 hours. Then, the pH value of the solution was adjusted to ~9 with 25% ammonia solution (at the controlled rate of 2-3 ml/min) and then stirred at room temperature for 2 hours. After that a homogenous clear solution (in a 2,500 ml beaker covered with a fine sieve) was heated and continuously stirred on a hot plate at around 200-300 °C to condense and the sol transformed into a dried gel. Then the self combustion was initiated and spread rapidly in the whole system and the combustion was finished instantaneously. The as-burned loose powders were ground by mortar and pestle, subsequently the synthesized perovskite oxide was calcined in a furnace in air to make the incompletely combusted part react thoroughly, achieve phase purity and eliminate the residual organic compound.

The conditions used for the calcination of the perovskite powders were set depending on the composition as follows:

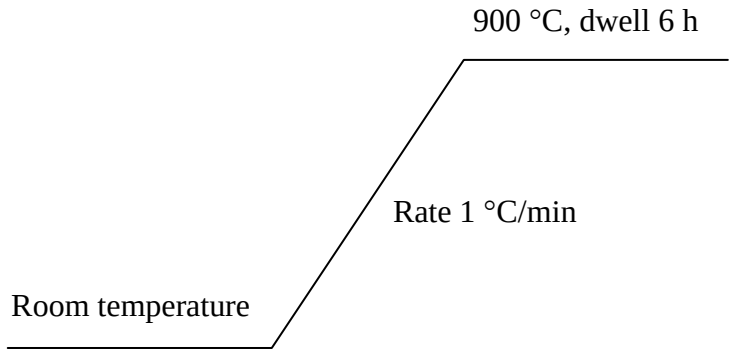

Figure 2.1 The condition of calcination for $La_{1-x}Sr_xFe_{1-y}M_yO_{3-\delta}$ M = Fe, Ni and Cu.

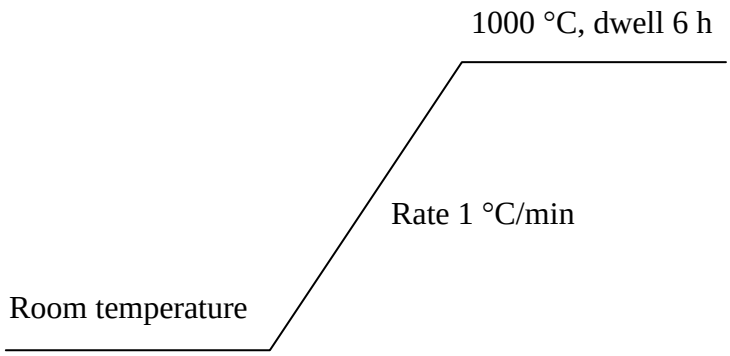

Figure 2.2 The condition of calcination for $La_{1-x}Sr_xFe_{1-y}M_yO_{3-\delta}$ M = Cr.

2.3 Perovskite disc preparation

The shape-forming process of perovskite powders was used by a KBr die.

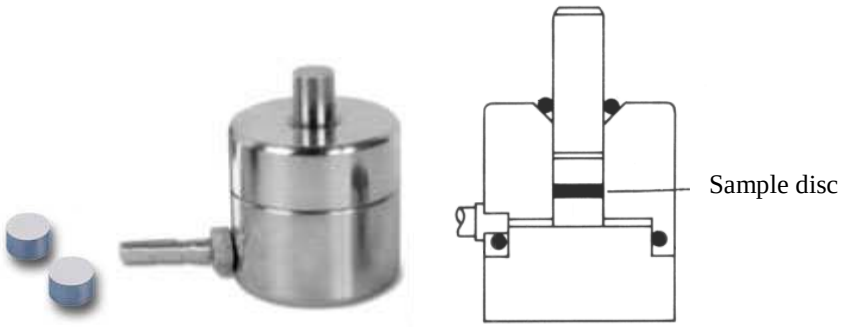

Figure 2.3 KBr die.

The calcined perovskite powders were ground with ethanol by mortar for three times. The fine perovskite powders about 1.8 g. were loaded into the cavity of die. The plunger was brought to the surface of the powder gently and then rotates for smooth surface.

After that, the pressure was slowly applied about 2-2.5 tons on the plunger of the die by the uniaxial pressing machine. The pressure was released and the die was removed from the pressing machine after 10-15 minutes. The disc is around 1 mm thick, 13 mm diameter was stripped from the die and plunger. Then the discs were generally sintered in air.

2.4 The sintering of the perovskite oxides

The perovskite discs were generally sintered in air under different conditions, depending on the composition. The condition of sintering of perovskite disc was exhibited in Figures 2.4-2.5.

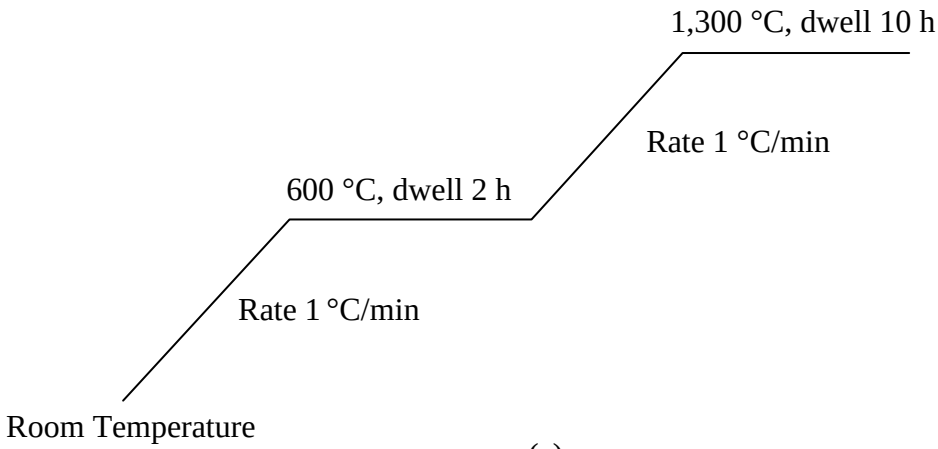

(a)

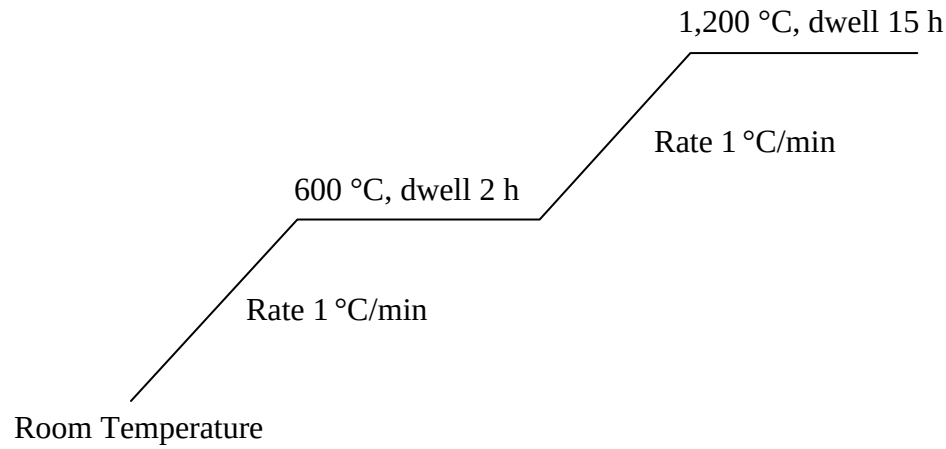

(b)

Figure 2.4 The sintering conditions of perovskite (a) $La_{1-x}Sr_xFeO_{3-\delta}$ and $La_{1-x}Sr_xFe_{1-y}Cr_yO_{3-\delta}$ (b) $La_{1-x}Sr_xFe_{1-y}Ni_yO_{3-\delta}$.

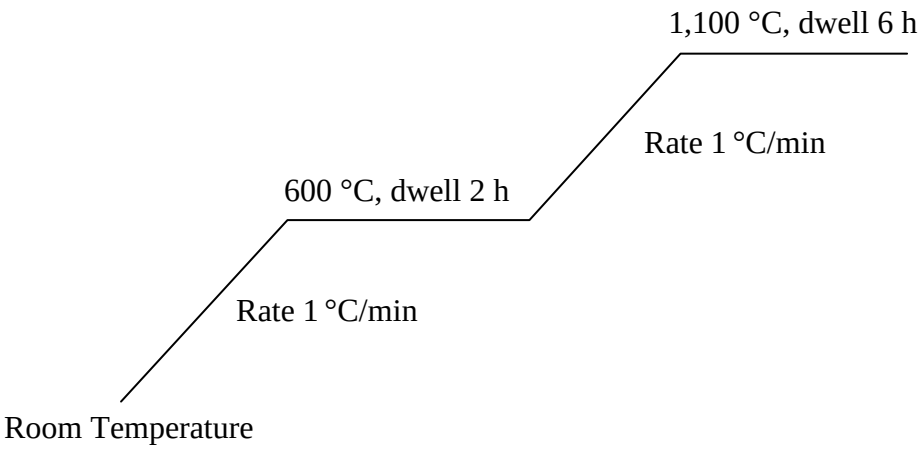

Figure 2.5 The sintering conditions of perovskite $La_{1-x}Sr_xFe_{1-y}Cu_yO_{3-\delta}$.

2.5 Characterization techniques

2.5.1 X-ray diffractrometry (XRD)

The phase formations of perovskite oxide were investigated after calcination by X-ray powder diffraction (XRD). The perovskite powders were ground and pressed on the slide before put in specimen slot of X-ray diffractometer. The XRD patterns were taken by using Rigaku, DMAX 2002 Ultima Plus X-Ray powder diffractometer equipped with a monochromator and a Cu-target X-ray tube (40 kV, 30 mA) and angles of 2θ ranged from 20-70 degree (step time 0.5 sec., scan step 0.020 degree) at Department of Chemistry, Faculty of Science, Chulalongkorn University.

2.5.2 Scanning electron microscopy (SEM)

The morphology of the sintered disc was carried out using a JEOL JSM-5800LV scanning electron microscopy, Oxford Instrument (Link ISIS series 300) at the Scientific and Technological Research Equipment Center (STREC), Chulalongkorn University. This instrument uses electrons scattered back from the surface “illuminated” by a restored electron beam to generate an image with remarkable three-dimensional qualities.

2.6 Properties measurement

2.6.1 Electrical conductivity measurement

The DC 4-probes is a device used for the investigation of electrical phenomena in air. The sintered disc was cut into a rectangular specimen with approximate dimensions of 12 mm x 5 mm x 1.5 mm. Four Pt wires were attached to the specimen with Pt paste as shown in Figure 2.6.

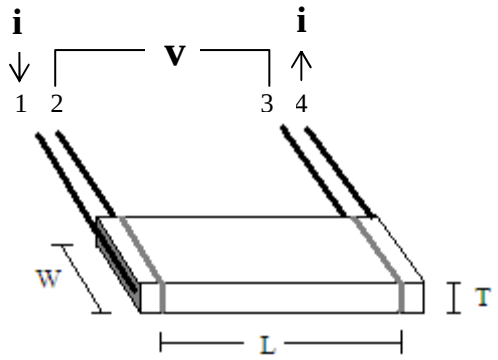

Figure 2.6 DC 4-probes measurement.

The condition used for the specimen was set as follows:

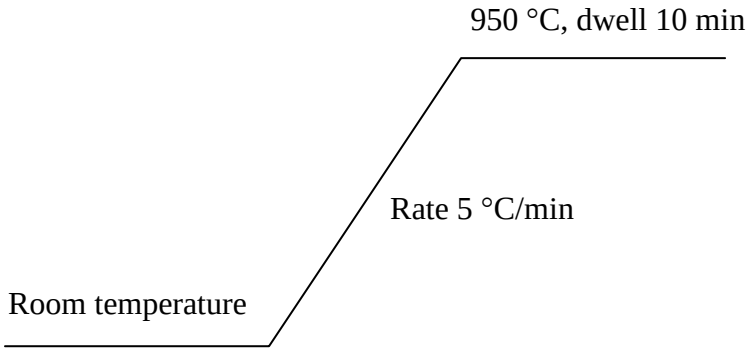

Figure 2.7 The heating conditions of the specimen.

The specimen was heated to 950 °C for 10 min with the heating rate of 5 °C/min. The electrical conductivity measurements were performed in a tube furnace at the temperature range of room temperature to 800 °C. Specimen was applied current (I) through the outer wires 1 to 4 and measured the voltages drop over wires 2 and 3 at each temperature by potentiostat/galvanostat (Autolab PG100).

The electrical conductivity was calculated by the equation:

$$\sigma = \frac{I}{V}\frac{L}{W \times T} \tag{2.1}$$

where σ = electrical conductivity

I = applied current (A)

V = resulting voltages (V)

L = length between Pt wires 2 and 3 (cm)

T = thickness of specimen (cm)

W = width of specimen (cm)

2.6.2 Thermal expansion measurement

The thermal expansion behavior is also critical to get the value matching between electrolyte material and electrodes material for SOFC.

A dilatometer, NETZSCH DIL 402C (from Department of Materials Science, Faculty of Science, Chulalongkorn University) was used to determine the thermal expansion coefficients (TEC) of the sintered specimens. The sintered disc was cut to specimen (about 12 mm in length, 5 mm in width and 1.5 mm in thickness). The principle of dilatometer is to measure the changing of specimen length compared to the changing of increased temperature. In this evaluation used heating rate of 10 °C /min and measured from room temperature to 800 °C in air.

2.6.3 Oxygen permeation measurement

Powders of the surface catalysts, $La_{0.6}Sr_{0.4}CoO_{3-\delta}$ and $La_{0.4}Sr_{0.6}Fe_{0.8}Ni_{0.2}O_{3-\delta}$, were prepared by modified citrate method. The starting materials were $La(NO_3)_3{\cdot}6H_2O$, $Sr(NO_3)_2$, $Fe(NO_3)_3{\cdot}9H_2O$, $Co(NO_3)_2{\cdot}6H_2O$ and $Ni(NO_3)_2{\cdot}6H_2O$. The $La_{0.6}Sr_{0.4}CoO_{3-\delta}$ and $La_{0.4}Sr_{0.6}Fe_{0.8}Ni_{0.2}O_{3-\delta}$ powders obtained by auto-combustion were fired at 1200 °C and 900 °C, respectively, for 6 h. The resultant powders were ground and confirmed to be the single phase by the X-ray powder diffractometer.

The thickness of the sintered membrane was polished to be 0.7 mm by grinding with a diamond grinding machine. The catalyst powders ($La_{0.6}Sr_{0.4}CoO_{3-\delta}$ or $La_{0.4}Sr_{0.6}Fe_{0.8}Ni_{0.2}O_{3-\delta}$) were ground again and then coated on one or both surfaces of membrane with the slurry using butyl acetate for solvent and then fired at 800 °C.

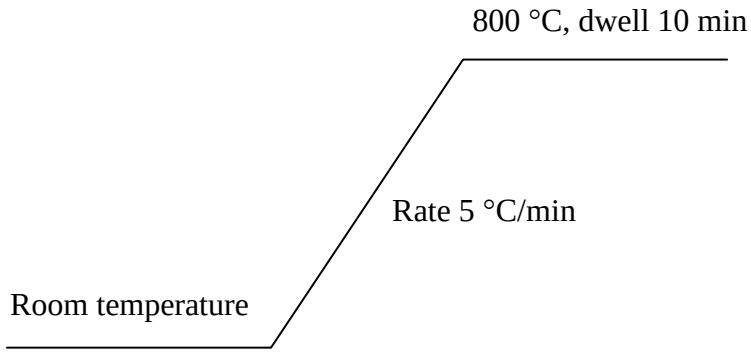

Figure 2.8 The heating conditions of the coated disc.

The oxygen permeation rate from air to He was measured by using the equipment described in Figure 2.9. The specimen was sealed into a mullite tube with a Pyrex glass. Dry air and He gas were supplied to each side of the specimen at a flow rate of 50 ml/min. Oxygen permeation flux from air to He was measured in the temperature range of 600-1000 °C by a gas chromatograph (VARIAN, CP-3800) and repeated twice.

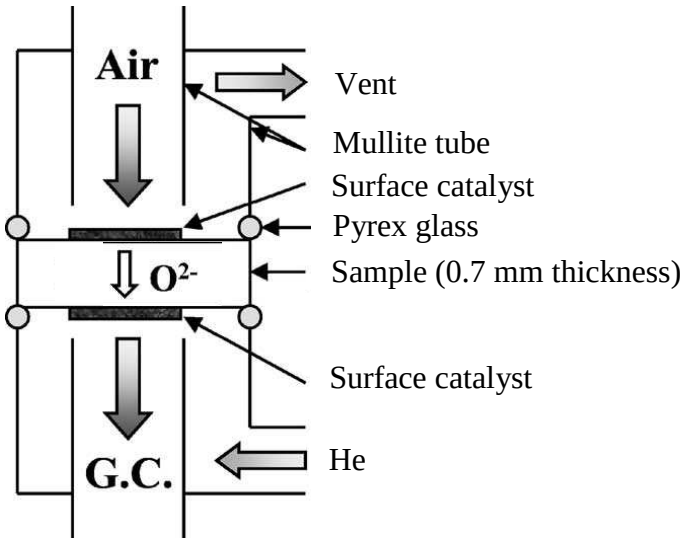

Figure 2.9 Schematic view of the membrane reactor used for oxygen permeation [45].

CHAPTER III

RESULTS AND DISCUSSIONS

In this research, perovskite powders $LaFeO_3$ were doped with different contents of metal ions in A-site (Sr) and B-site (Cr, Ni and Cu). Each perovskite compound is indicated by the abbreviation using the initial letters of each metal in A and B-sites sequentially, followed by the corresponding number which refers to the proportion of each metal in the compound. For examples, $La_{0.4}Sr_{0.6}Fe_{0.9}Cr_{0.1}O_{3-\delta}$ and $La_{0.4}Sr_{0.6}FeO_{3-\delta}$ are abbreviated as LSFCr4691 and LSF46, respectively.

3.1 Synthesis of $La_{1-x}Sr_xFe_{1-y}M_yO_{3-\delta}$ (M = Cr, Ni and Cu; x = 0.3-0.7; y = 0.0-0.3) by modified citrate method

The perovskite powders $La_{1-x}Sr_xFe_{1-y}M_yO_{3-\delta}$ were prepared by the modified citrate method. The metal nitrates were dissolved in D.I. water and citric acid was added at a ratio of citric acid to metal ions 2:1. The pH value of the solution was adjusted to ~9 with 25% ammonia solution ($NH_3 \cdot H_2O$), the solution changed from clear red brown to clear deep brown solution. Then a clear solution was heated and stirred, the excess solvent was firstly evaporated until a sticky gel was obtained. During the final stage of evaporation, the mixture began to swell, and became viscous. The generated gas was observed. Finally, at around 200-300 °C the spontaneous combustion was initiated to convert the mixture into the oxide powder.

The powders were calcined in air at 900-1,100 °C for 6 hours to achieve pure phase and remove residual organic compound. The calcined powders were ground and pressed to make a disc. The perovskite discs were sintering in air at 1,100-1,300 °C for 10-15 hours, depending on the composition, to increase the density of the perovskite disc and eliminate the pores.

3.2 Characterization of the synthesized compounds

The structures of synthesized perovskite compounds were characterized by XRD and the surface morphology of the sintered discs were examined by SEM.

3.2.1 X-ray diffraction (XRD)

XRD was used to indicate the formation of the perovskite phase. The phase formations of perovskites were investigated after calcination. If the XRD patterns of the calcined powders showed impurity phase, the perovskite phase of sintered disc were investigated. The diffraction peaks of perovskites were observed within angles of 2θ ranged from 20-70 degree.

3.2.1.1 Phase formation of $La_{1-x}Sr_xFeO_{3-\delta}$ (x = 0.3-0.7)

The formation of $La_{1-x}Sr_xFeO_{3-\delta}$ (x = 0.3-0.7) calcined powders investigated by XRD was shown in Figure 3.1.

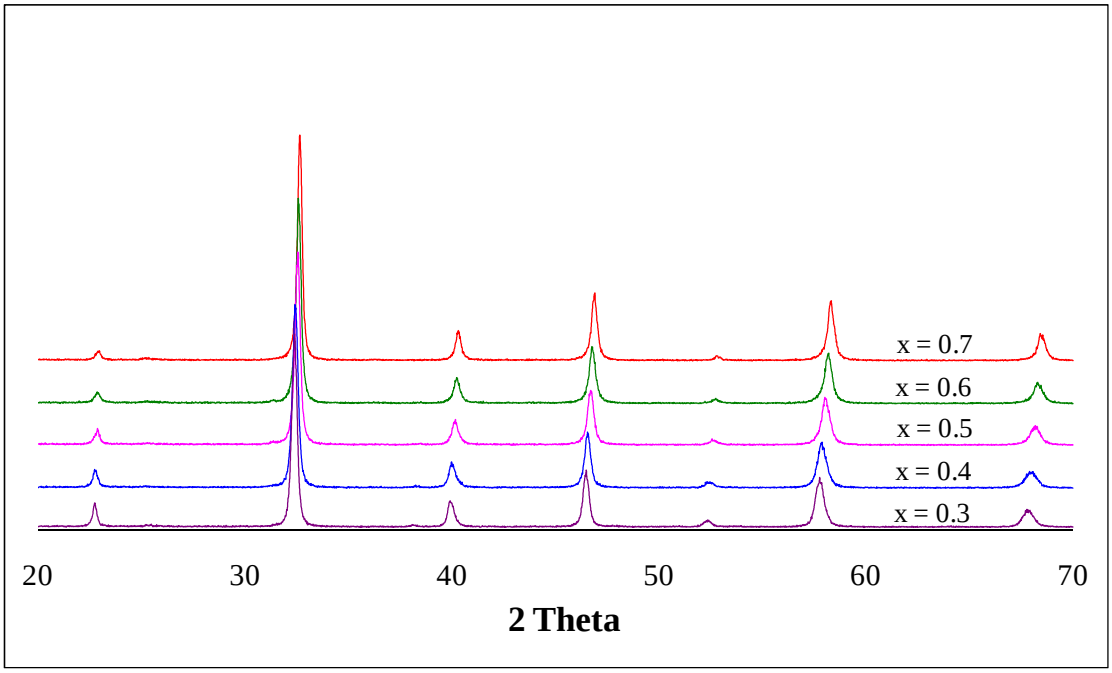

Figure 3.1 XRD patterns of $La_{1-x}Sr_xFeO_{3-\delta}$ (x = 0.3-0.7) powders after calcined at 900 °C for 6 hours.

The XRD patterns of $La_{1-x}Sr_xFeO_{3-\delta}$ in the range $0.3 \leq x \leq 0.7$ exhibited the single phase of ABO_3 perovskite oxides with a cubic structure (a space group P23 (195)). Miller index from these perovkite structures was 100, 110, 111, 200, 012, 211 and 220. The lattice parameter calculated by Jade software was shown in Table 3.1.

It was observed that the XRD patterns shifted to the higher angle with increasing of Sr in $La_{1-x}Sr_xFeO_{3-\delta}$, corresponding to the lattice shrinkage. This shift increased with the increasing content of Sr. When La lattice sites (La^{3+}; 1.032 A°) are partially occupied by the larger ionic radius of Sr^{2+} (1.180 A°), the charge imbalance occurs. Since there are two ways to maintain charge neutrality: electronic compensation by oxidizing Fe^{3+} to Fe^{4+} and ionic compensation by the formation of oxygen vacancies [46]. Then, the stoichiometric $LaFeO_3$ structure is transformed to oxygen deficient $La_{1-x}Sr_xFeO_{3-\delta}$ perovskite. Some of Fe^{3+} (0.645 A°) oxidized to Fe^{4+} (0.585 A°) reduces the average ion radius of the B-site. When x value increases, the concentration of Fe^{4+} and oxygen vacancies increased, making the diffusion of lattice oxygen from the bulk to the surface more favorable. Therefore, with the increase of Sr content, the lattice must be reduced to maintain the perovskite structure, causing smaller lattice parameter. The XRD result in this work is similar to the report of Armstrong et al. [47]. They explained why the lattice volume of $La_{1-x}Sr_xFeO_{3-\delta}$ was decreased although Sr^{2+} ion has a larger ionic radius than that of La^{3+} ion. Because the size changes due to the B-site transition (the increase of Fe^{4+}content) had a greater effect on the lattice size than that due to the substitution of Sr on the La sites. The decrease of lattice parameter with the increase of Sr content in $La_{1-x}Sr_xFeO_{3-\delta}$ was shown in Figure 3.2.

Table 3.1 The lattice parameters of $La_{1-x}Sr_xFeO_{3-\delta}$ (x = 0.3-0.7) powders after calcined at 900 °C for 6 hours

Ratio	Lattice parameter (A°)
x = 0.3	3.905
x = 0.4	3.893
x = 0.5	3.887
x = 0.6	3.881
x = 0.7	3.870

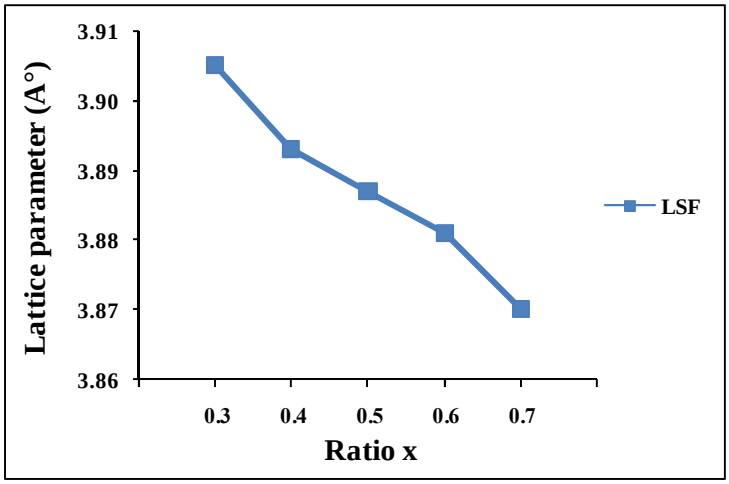

Figure 3.2 Ratio x dependence of the lattice parameters for $La_{1-x}Sr_xFeO_{3-\delta}$ (x = 0.3-0.7) powders.

3.2.1.2 Phase formation of $La_{1-x}Sr_xFe_{0.9}Cr_{0.1}O_{3-\delta}$ (x = 0.3-0.7)

Figure 3.3 shows the XRD patterns of $La_{1-x}Sr_xFe_{0.9}Cr_{0.1}O_{3-\delta}$ (x = 0.3-0.7) powders calcined at 1,100 °C for 6 hours.

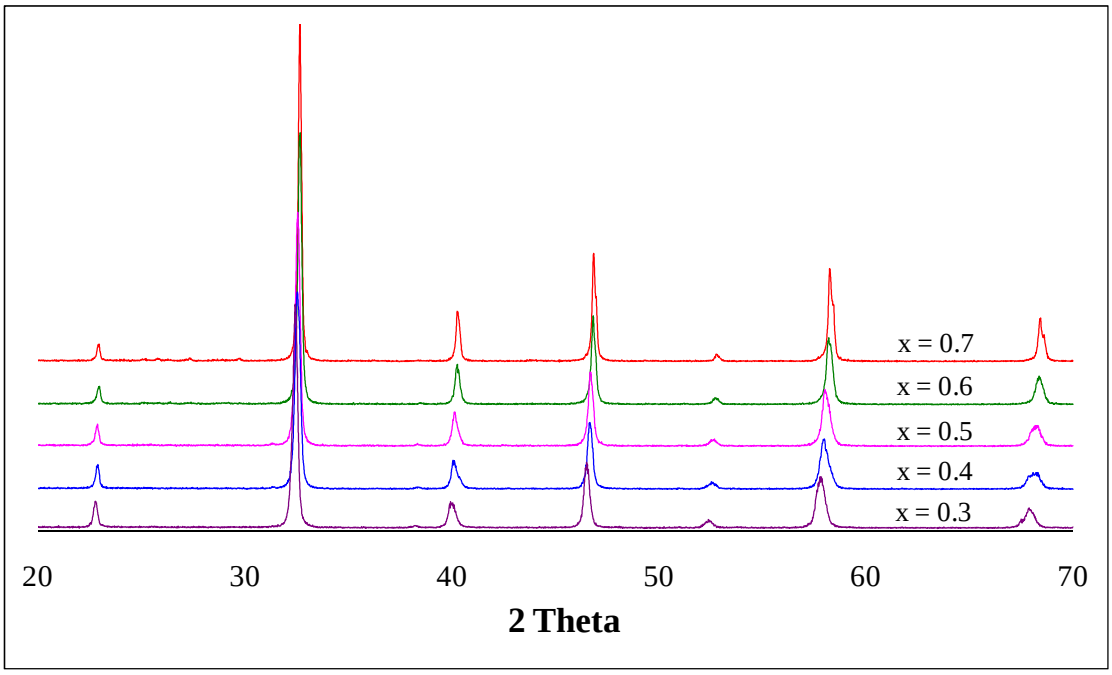

Figure 3.3 XRD patterns of $La_{1-x}Sr_xFe_{0.9}Cr_{0.1}O_{3-\delta}$ (x = 0.3-0.7) powders after calcined at 1,100 °C for 6 hours.

The XRD results demonstrated that all samples doped with 0.1 mol of Cr in the B-site of $La_{1-x}Sr_xFeO_{3-\delta}$ (x = 0.3-0.7) did not exhibit any impurity phase. As shown in Figure 3.3, the XRD peaks shifted slightly to the higher angle when compared with those of $La_{1-x}Sr_xFeO_{3-\delta}$ perovskites. The lattice parameters of $La_{1-x}Sr_xFe_{0.9}Cr_{0.1}O_{3-\delta}$ were similar to the results of $La_{1-x}Sr_xFeO_{3-\delta}$, they decreased with increasing the amount of Sr (Table 3.2 and Figure 3.4). It means that Cr^{3+} and smaller Cr^{4+} ion occupy the part of Fe^{3+} and Fe^{4+} sites in $La_{1-x}Sr_xFeO_{3-\delta}$ crystal lattice. Thus the lattice parameter should diminish. The parameters decrease slightly from those of undoped oxides because the content of Cr was only 10%.

Table 3.2 The lattice parameters of $La_{1-x}Sr_xFe_{0.9}Cr_{0.1}O_{3-\delta}$ (x = 0.3-0.7) powders after calcined at 1,100 °C for 6 hours

Ratio	Lattice parameter (A°)
x = 0.3	3.902
x = 0.4	3.889
x = 0.5	3.887
x = 0.6	3.878
x = 0.7	3.867

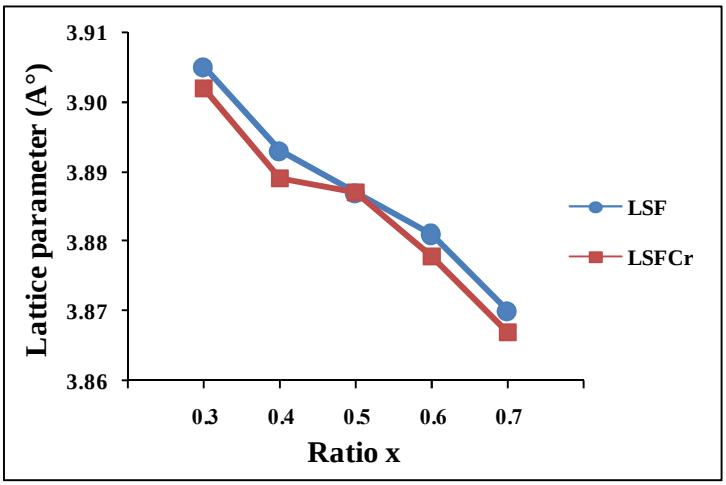

Figure 3.4 Ratio x dependence of the lattice parameters for $La_{1-x}Sr_xFe_{0.9}Cr_{0.1}O_{3-\delta}$ (x = 0.3-0.7) powders.

3.2.1.3 Phase formation of $La_{0.4}Sr_{0.6}Fe_{1-y}Cr_yO_{3-\delta}$ (y = 0.0-0.3)

It should be noted here that complete perovskite structure of $La_{0.4}Sr_{0.6}Fe_{1-y}Cr_yO_{3-\delta}$ (y = 0.2-0.3) can be obtained after sintering. XRD patterns of $La_{0.4}Sr_{0.6}Fe_{1-y}Cr_yO_{3-\delta}$ (y = 0.0-0.3) sintered discs were shown in Figure 3.5.

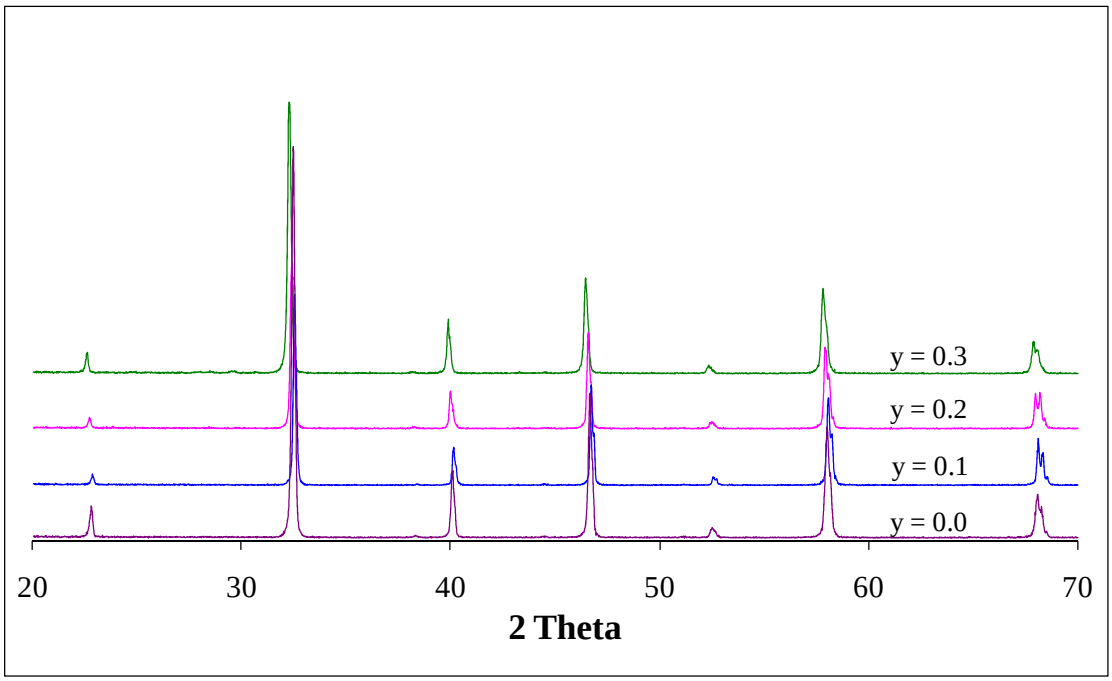

Figure 3.5 XRD patterns of $La_{0.4}Sr_{0.6}Fe_{1-y}Cr_yO_{3-\delta}$ (y = 0.0-0.3) discs after sintered at 1,300 °C for 10 hours.

XRD patterns of Cr-doped perovskite oxide revealed single phase with cubic structure. The peaks shifted to the lower angle as compared with that of $La_{0.4}Sr_{0.6}FeO_{3-\delta}$ especially when Cr = 0.3. The experiment results showed the lattice parameter expand when Cr concentration increased to 0.2 and 0.3. It was seen that the lattice parameter of $La_{1-x}Sr_xFeO_{3-\delta}$ change slightly when doped Cr 10% (see Figure 3.6). Incorporating two types of transition metal ions with different sizes at B-site can cause simple distortion of the cubic unit cell or enlargement of cubic unit cell or a combination of both. Figure 3.6 showed the cubic structure can be maintained with larger lattice parameters.

Table 3.3 The lattice parameters of $La_{0.4}Sr_{0.6}Fe_{1-y}Cr_yO_{3-\delta}$ (y = 0.0-0.3) discs after sintered at 1,300 °C for 10 hours

Ratio	Lattice parameter (A°)
y = 0.0	3.892
y = 0.1	3.889
y = 0.2	3.898
y = 0.3	3.905

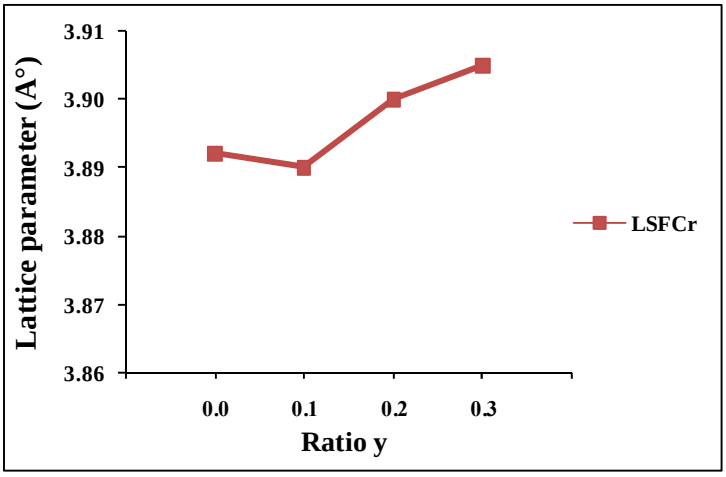

Figure 3.6 Ratio y dependence of the lattice parameters for $La_{0.4}Sr_{0.6}Fe_{1-y}Cr_yO_{3-\delta}$ (y = 0.0-0.3) discs.

3.2.1.4 Phase formation of $La_{1-x}Sr_xFe_{0.9}Ni_{0.1}O_{3-\delta}$ (x = 0.3-0.7)

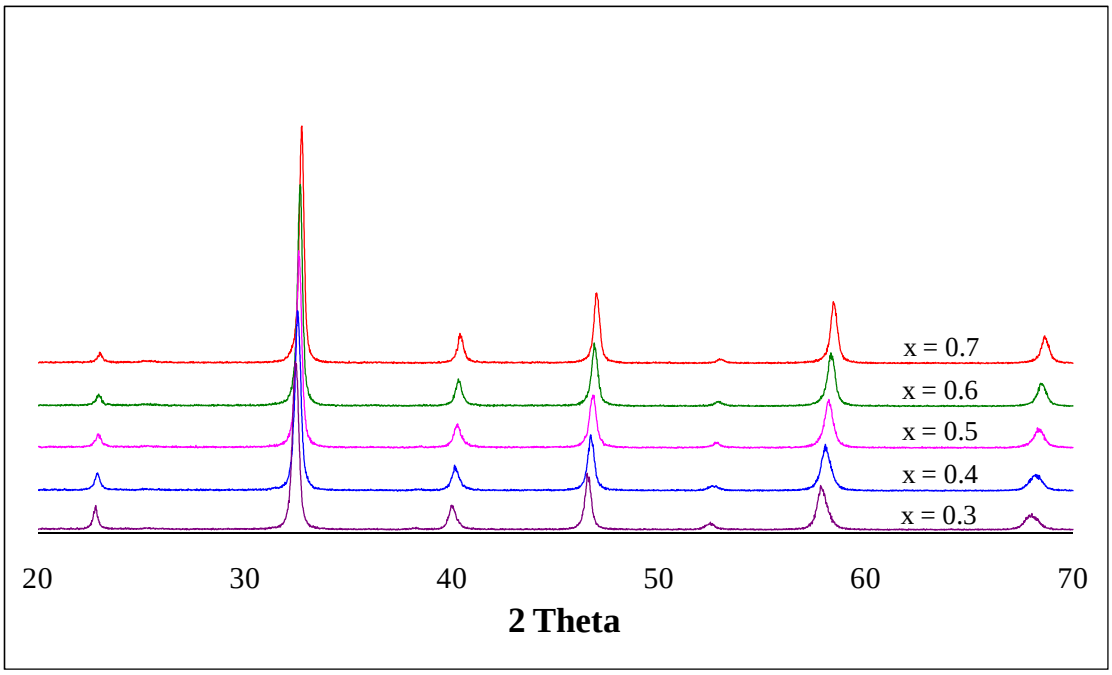

Figure 3.7 XRD patterns of $La_{1-x}Sr_xFe_{0.9}Ni_{0.1}O_{3-\delta}$ (x = 0.3-0.7) powders after calcined at 900 °C for 6 hours.

The XRD patterns of all samples doping with 0.1 mol of Ni at the B-sites of $La_{1-x}Sr_xFeO_{3-\delta}$ (x = 0.3-0.7) were displayed in Figure 3.7. It demonstrated that $La_{1-x}Sr_xFe_{0.9}Ni_{0.1}O_{3-\delta}$ has no impurity phase and the structures are cubic. The XRD patterns of doped Ni specimens are slightly shifted to the higher angle compared with $La_{1-x}Sr_xFeO_{3-\delta}$. As shown in Table 3.4 and Figure 3.8, the lattice parameters of $La_{1-x}Sr_xFe_{0.9}Ni_{0.1}O_{3-\delta}$ decreased with increasing Sr content. The lattice parameters of Ni-doping in $La_{1-x}Sr_xFe_{0.9}Ni_{0.1}O_{3-\delta}$ oxide are slightly lower than those of undoped perovskites. The decrease in the lattice parameters is due to the content of Ni^{3+} substituted Fe^{3+} since the ionic radius of Ni^{3+} (0.56 A°) is smaller than that Fe^{3+} (0.645 A°)

Table 3.4 The lattice parameters of $La_{1-x}Sr_xFe_{0.9}Ni_{0.1}O_{3-\delta}$ (x = 0.3-0.7) powders after calcined at 900 °C for 6 hours

Ratio	Lattice parameter (A°)
x = 0.3	3.901
x = 0.4	3.887
x = 0.5	3.878
x = 0.6	3.873
x = 0.7	3.865

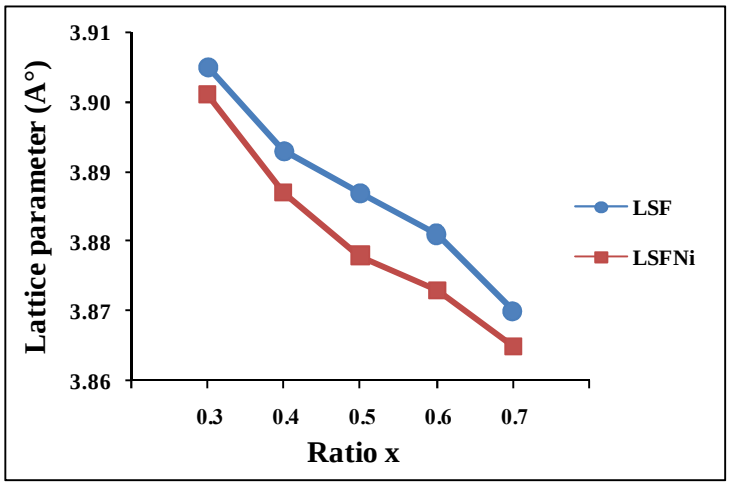

Figure 3.8 Ratio x dependence of the lattice parameters for $La_{1-x}Sr_xFe_{0.9}Ni_{0.1}O_{3-\delta}$ (x = 0.3-0.7) powders.

3.2.1.5 Phase formation of $La_{0.4}Sr_{0.6}Fe_{1-y}Ni_yO_{3-\delta}$ (y = 0.0-0.2)

Figure 3.9 shows the XRD patterns of $La_{0.4}Sr_{0.6}Fe_{1-y}Ni_yO_{3-\delta}$ (y = 0.0-0.2) discs sintered at 1,200 °C for 15 hours.

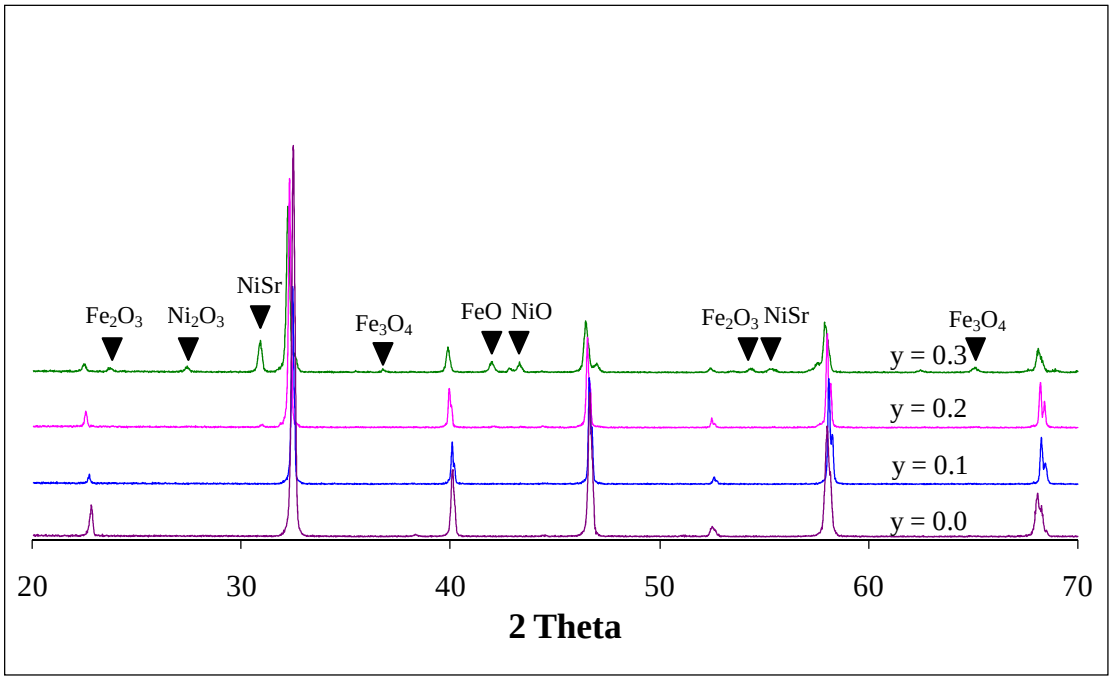

Figure 3.9 XRD patterns of $La_{0.4}Sr_{0.6}Fe_{1-y}Ni_yO_{3-\delta}$ (y = 0.0-0.3) discs after sintered at 1,200 °C for 15 hours.

The XRD patterns confirmed that all oxide samples had cubic perovskite structure. Single phase of perovskite structure was observed for doped $La_{0.4}Sr_{0.6}FeO_{3-\delta}$ when y = 0.0-0.2. But impurity phases appeared when y = 0.3 such as Fe_2O_3, Ni_2O_3 and NiSr. It was suggested that $La_{0.4}Sr_{0.6}FeO_{3-\delta}$ cannot be doped with 0.3 mol of Ni. With the increasing of Ni, the XRD peaks shifted gradually to the lower angle. Table 3.5 and Figure 3.10 showed that Ni content increased from 10% to 20% replaced at Fe site, the parameter barely increased.

Table 3.5 The lattice parameters of $La_{0.4}Sr_{0.6}Fe_{1-y}Ni_yO_{3-\delta}$ (y = 0.0-0.2) discs after sintered at 1,200 °C for 15 hours

Ratio	Lattice parameter (A°)
y = 0.0	3.892
y = 0.1	3.888
y = 0.2	3.893

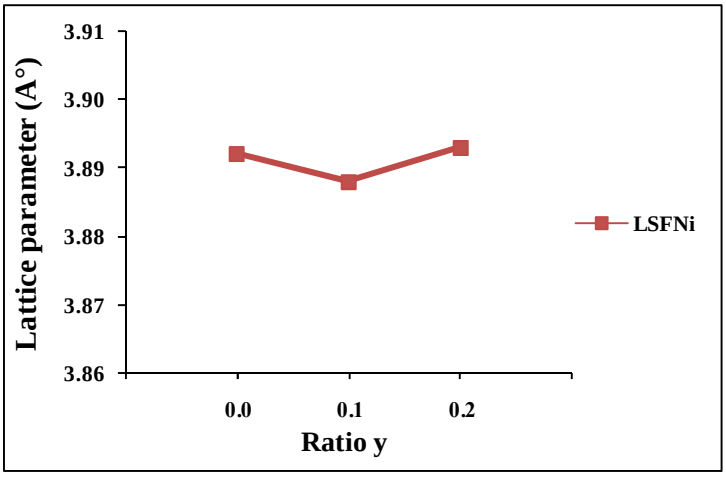

Figure 3.10 Ratio y dependence of the lattice parameters for $La_{0.4}Sr_{0.6}Fe_{1-y}Ni_yO_{3-\delta}$ (y = 0.0-0.2) discs.

3.2.1.6 Phase formation of $La_{1-x}Sr_xFe_{0.9}Cu_{0.1}O_{3-\delta}$ (x = 0.3-0.7)

The XRD patterns of $La_{1-x}Sr_xFe_{0.9}Cu_{0.1}O_{3-\delta}$ (x = 0.3-0.7) powders were depicted in Figure 3.11.

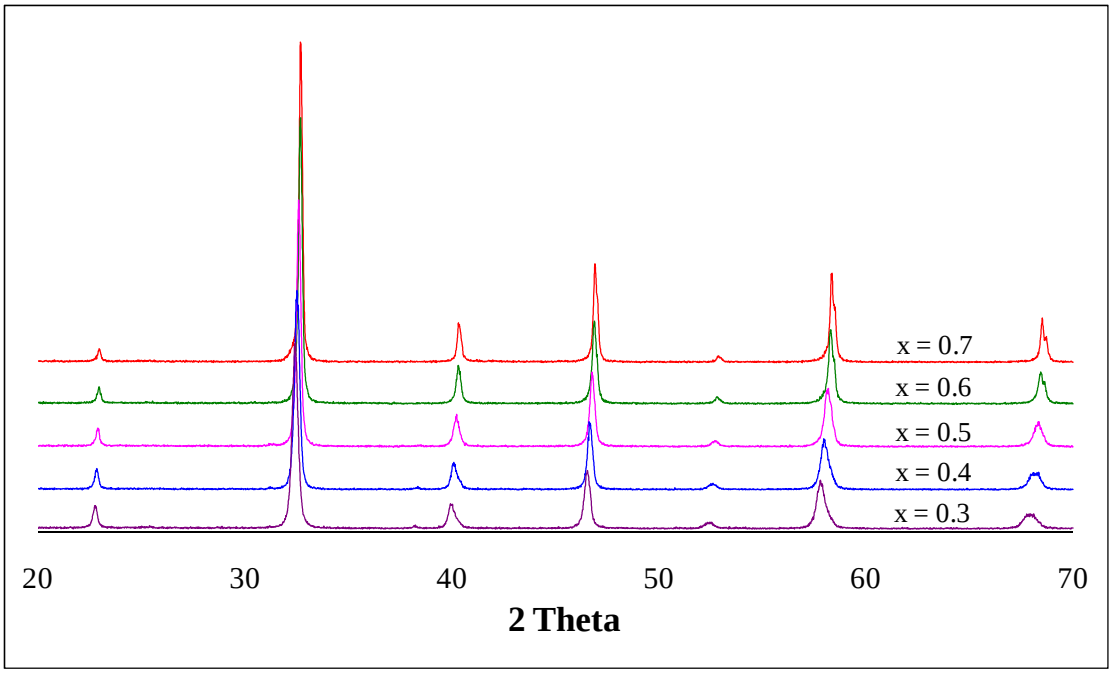

Figure 3.11 XRD patterns of $La_{1-x}Sr_xFe_{0.9}Cu_{0.1}O_{3-\delta}$ (x = 0.3-0.7) powders after calcined at 900 °C for 6 hours.

The XRD results indicated that Fe replaced by Cu 0.1 mol showed single phase and a cubic structure. XRD patterns of $La_{1-x}Sr_xFe_{0.9}Cu_{0.1}O_{3-\delta}$ shifted very slightly when compared with those of $La_{1-x}Sr_xFeO_{3-\delta}$ (x = 0.3-0.7). It was suggested that 0.1 mol of Cu can replace partially into Fe without any change of the $La_{1-x}Sr_xFeO_{3-\delta}$ structure. The lattice parameters of $La_{1-x}Sr_xFeO_{3-\delta}$ doping with 0.1 mol of Cu slightly changed and decreased with increasing Sr content, they were similar to the results of $La_{1-x}Sr_xFeO_{3-\delta}$. The substitution of 10% Fe^{3+} by Cu^{2+} leads to positive charge deficiency, which is compensate for by oxygen vacancy, resulting in decreasing of parameters.

Table 3.6 The lattice parameters of $La_{1-x}Sr_xFe_{0.9}Cu_{0.1}O_{3-\delta}$ (x = 0.3-0.7) after calcined at 900 °C for 6 hours

Ratio	Lattice parameter (A°)
x = 0.3	3.902
x = 0.4	3.885
x = 0.5	3.881
x = 0.6	3.876
x = 0.7	3.868

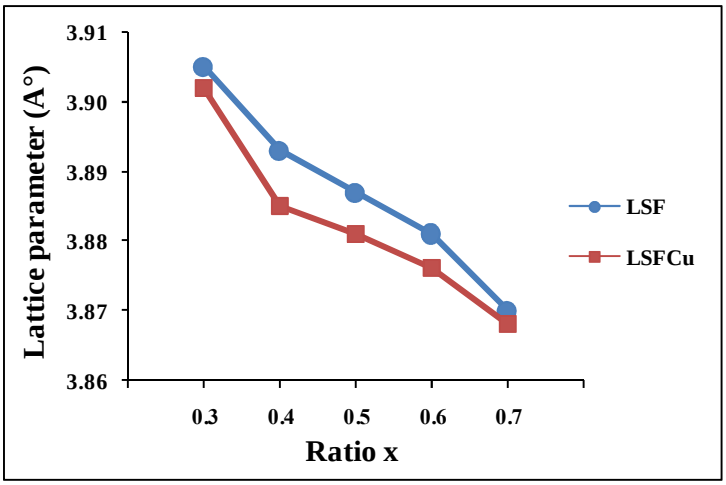

Figure 3.12 Ratio x dependence of the lattice parameters for $La_{1-x}Sr_xFe_{0.9}Cu_{0.1}O_{3-\delta}$ (x = 0.3-0.7) powders.

3.2.1.7 Phase formation of $La_{0.4}Sr_{0.6}Fe_{1-y}Cu_yO_{3-\delta}$ (y = 0.0-0.3)

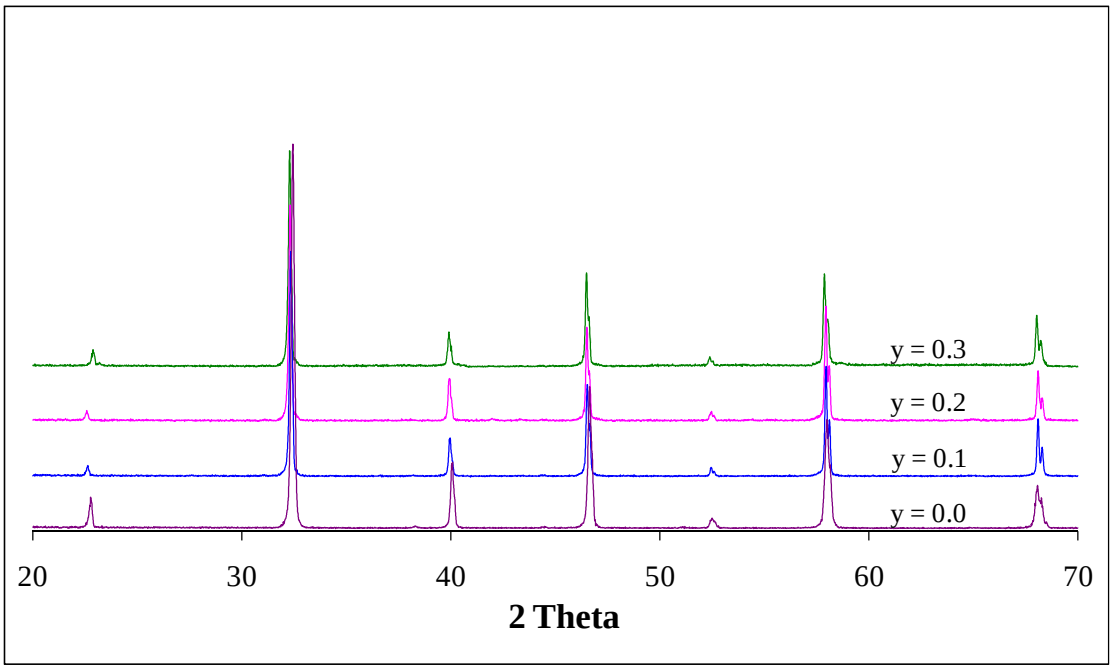

Figure 3.13 XRD patterns of $La_{0.4}Sr_{0.6}Fe_{1-y}Cu_yO_{3-\delta}$ (y = 0.0-0.3) discs after sintered at 1,100 °C for 6 hours.

Figure 3.13 shows the XRD patterns of $La_{0.4}Sr_{0.6}Fe_{1-y}Cu_yO_{3-\delta}$ (y = 0.0-0.2) discs sintered at 1,100 °C for 6 hours. The XRD results indicated that Fe replaced by Cu showed single phase and a cubic structure. XRD peaks of doped oxides shifted slightly to the lower angle when compared with $La_{0.4}Sr_{0.6}FeO_{3-\delta}$. The the lattice parameters of Cu-doped $La_{0.4}Sr_{0.6}FeO_{3-\delta}$ slightly decreased when Cu 0.1 mol. The replacing of Fe^{3+} by smaller ions (Cu^{3+}) would effect to the decreasing of lattice parameter and Fe–O covalent bond. However, the lattice parameters of $La_{0.4}Sr_{0.6}Fe_{1-y}Cu_yO_{3-\delta}$ increased when Cu content changed to 0.2 and 0.3 mol. It was due to the increasing of Cu–O covalent bond which might cause the loss of oxygen from structure. The force of positive charge made the increasing of lattice parameters.

Table 3.7 The lattice parameters of $La_{0.4}Sr_{0.6}Fe_{1-y}Cu_yO_{3-\delta}$ (y = 0.0-0.3) discs after sintered at 1,100 °C for 6 hours

Ratio	Lattice parameter (A°)
y = 0.0	3.892
y = 0.1	3.890
y = 0.2	3.892
y = 0.3	3.899

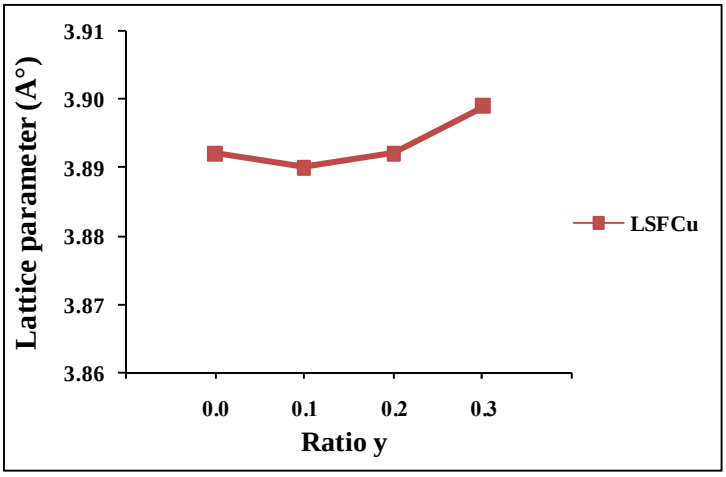

Figure 3.14 Ratio y dependence of the lattice parameters for $La_{0.4}Sr_{0.6}Fe_{1-y}Cu_yO_{3-\delta}$ (y = 0.0-0.3) discs.

The XRD results confirmed that $La_{1-x}Sr_x\ Fe_{1-y}M_yO_{3-\delta}$ (M = Cr, Ni and Cu; x = 0.3-0.7; y = 0.0-0.3) had cubic perovsike structure. However, XRD pattern of $La_{0.4}Sr_{0.6}Fe_{0.7}Ni_{0.3}O_{3-\delta}$ showed impurity phase. It was suggested that Ni 0.3 mol cannot be doped at B-site of $La_{0.4}Sr_{0.6}FeO_{3-\delta}$.

The XRD results indicated that La replaced by Sr at A-site had effect on the lattice parameter. With increasing content of Sr, the lattice parameter decreased significantly. The compensate electroneutrality of the perovskite oxide with the formation of oxygen vacancies caused the shrinkage of lattice parameter. As compared to B-site doping (doped Fe by Cr, Ni and Cu); the small change of parameters was observed.

3.2.2 Scanning electron microscope (SEM) and density

The surface morphologies of perovskite discs were characterized by SEM technique. Densities of samples were determined by the Archimedes immersion method using water as a medium.

3.2.2.1 Morphologies of $La_{1-x}Sr_xFeO_{3-\delta}$ (x = 0.3-0.7)

The surface morphology of $La_{1-x}Sr_xFeO_{3-\delta}$ sintered discs was investigated by SEM shown in Figure 3.15.

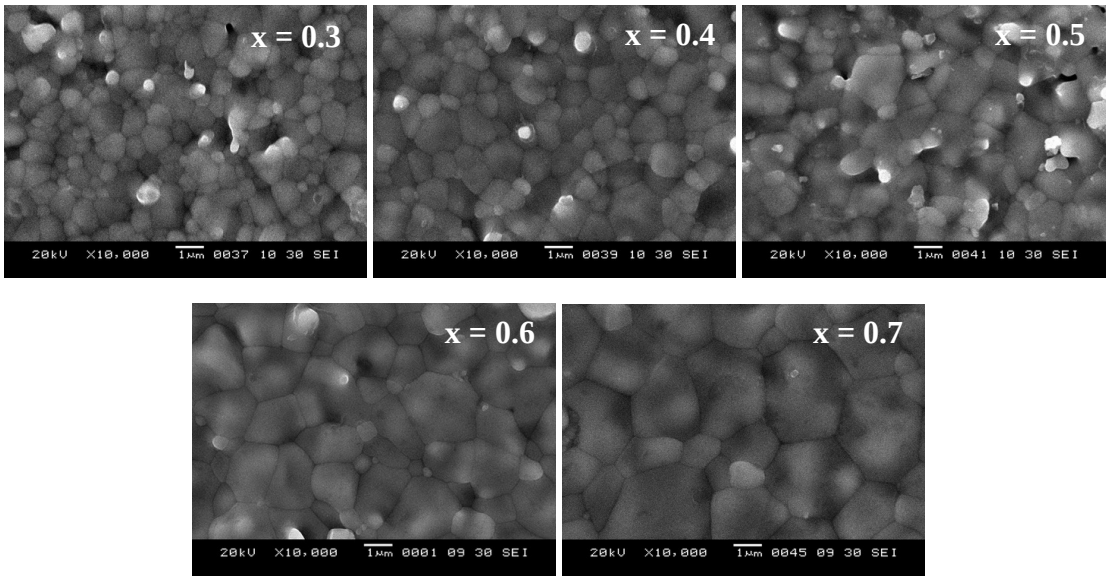

Figure 3.15 Surface morphology of $La_{1-x}Sr_xFeO_{3-\delta}$ (x = 0.3-0.7) discs.

Table 3.8 Density of $La_{1-x}Sr_xFeO_{3-\delta}$ (x = 0.3-0.7) discs

Ratio	Density ($g.cm^3$)	Relative density (%)
x = 0.3	6.080	95.72
x = 0.4	5.856	93.44
x = 0.5	5.759	93.61
x = 0.6	5.625	93.20
x = 0.7	5.504	92.64

SEM micrographs of $La_{1-x}Sr_xFeO_{3-\delta}$ (x = 0.3-0.7) discs exhibited high density (relative density > 92%) and homogeneous surface. The grain size increases with increasing of Sr content. According to our results, $La_{0.3}Sr_{0.7}FeO_{3-\delta}$ showed the

largest grain size. The densities of $La_{1-x}Sr_x$ $FeO_{3-\delta}$ disc decrease with the increase of Sr which was listed in Table 3.8.

3.2.2.2 Morphologies of $La_{1-x}Sr_xFe_{0.9}Cr_{0.1}O_{3-\delta}$ (x = 0.3-0.7)

The surface morphology of $La_{1-x}Sr_xFe_{0.9}Cr_{0.1}O_{3-\delta}$ (x = 0.3-0.7) disc after sintered at 1,300 °C for 10 hours were indicated in Figure 3.16.

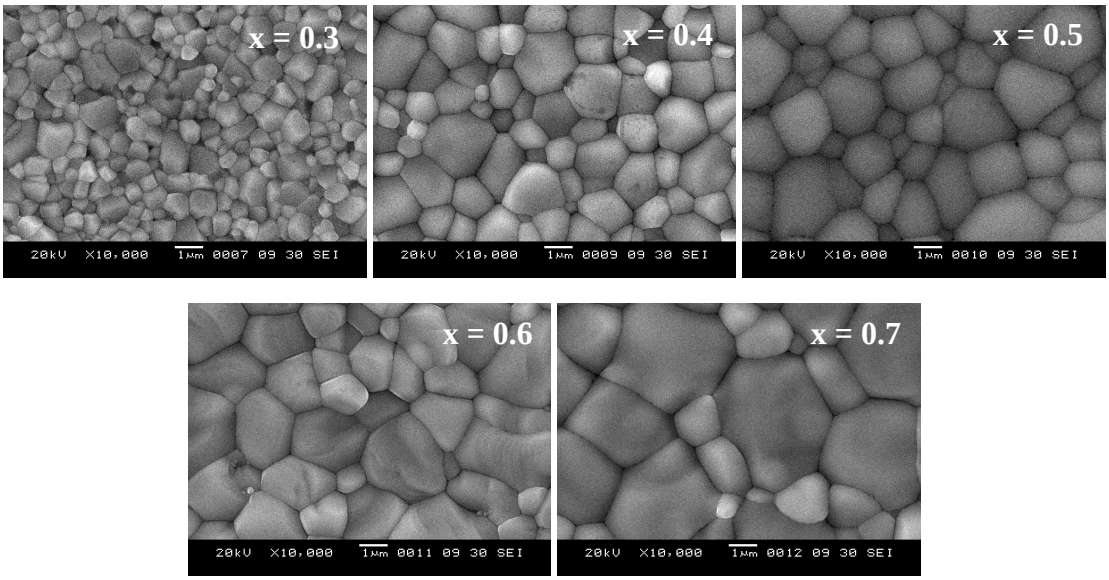

Figure 3.16 Surface morphology of $La_{1-x}Sr_xFe_{0.9}Cr_{0.1}O_{3-\delta}$ (x = 0.3-0.7) discs.

SEM pictures of $La_{1-x}Sr_xFe_{0.9}Cr_{0.1}O_{3-\delta}$ show the dense morphology without any impurity phase on the surface which is consistent with the XRD results. It is seen that the grain size of $La_{1-x}Sr_xFeO_{3-\delta}$ (x = 0.3-0.7) increased with the substitution Cr 0.1 mol in B-site (when x > 0.3). The relative density of La_{1-x} $Sr_xFe_{0.9}Cr_{0.1}O_{3-\delta}$ (x = 0.3-0.7) discs are more than 94% as shown in Table 3.9.

Table 3.9 Density of $La_{1-x}Sr_xFe_{0.9}Cr_{0.1}O_{3-\delta}$ (x = 0.3-0.7) discs

Ratio	Density ($g.cm^3$)	Relative density (%)
x = 0.3	6.027	94.83
x = 0.4	5.911	94.19
x = 0.5	5.875	95.67
x = 0.6	5.770	95.56
x = 0.7	5.691	96.42

3.2.2.3 Morphologies of $La_{0.4}Sr_{0.6}Fe_{1-y}Cr_yO_{3-\delta}$ (y = 0.0-0.3)

Figure 3.17 shows the surface morphology of $La_{0.4}Sr_{0.6}Fe_{1-y}Cr_yO_{3-\delta}$ (y = 0.0-0.3) discs sintered at 1,300 °C for 10 hours.

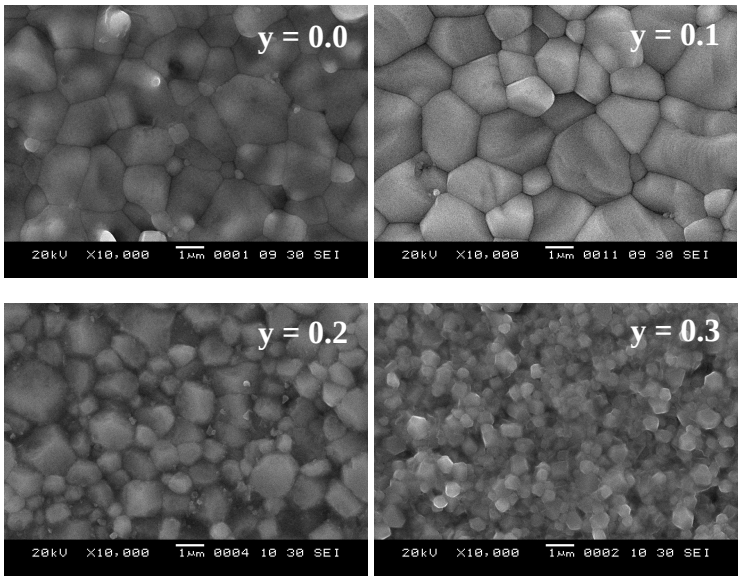

Figure 3.17 Surface morphology of $La_{0.4}Sr_{0.6}Fe_{1-y}Cr_yO_{3-\delta}$ (y = 0.0-0.3) discs.

The morphologies of $La_{0.4}Sr_{0.6}FeO_{3-\delta}$ doping with Cr^{3+} at B-site display dense surface. The grain size of the oxides increased when doped only 10% Cr but decreases when amount of Cr increase to 20 and 30%. It is seen that $La_{0.4}Sr_{0.6}Fe_{0.7}Cr_{0.3}O_{3-\delta}$ has the smallest grain size. The densities of $La_{0.4}Sr_{0.6}Fe_{1-y}Cr_yO_{3-\delta}$ with various Cr contents were listed in Table 3.10.

Table 3.10 Density of $La_{0.4}Sr_{0.6}Fe_{1-y}Cr_yO_{3-\delta}$ (y = 0.0-0.3) discs

Ratio	Density ($g.cm^3$)	Relative density (%)
y = 0.0	5.625	93.20
y = 0.1	5.770	95.56
y = 0.2	5.551	93.54
y = 0.3	5.487	93.13

3.2.2.4 Morphologies of $La_{1-x}Sr_xFe_{0.9}Ni_{0.1}O_{3-\delta}$ (x = 0.3-0.7)

Figure 3.18 shows the SEM micrographs of $La_{1-x}Sr_xFe_{0.9}Ni_{0.1}O_{3-\delta}$ (x = 0.3-0.7) disc sintered at 1200 °C for 15 hours.

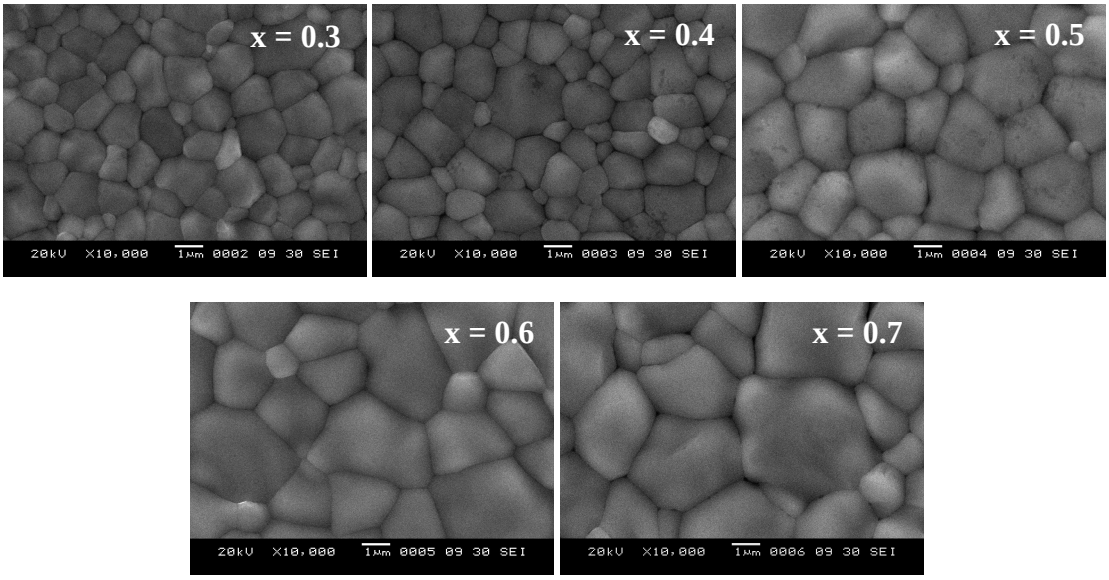

Figure 3.18 Surface morphology of $La_{1-x}Sr_xFe_{0.9}Ni_{0.1}O_{3-\delta}$ (x = 0.3-0.7) discs.

The microstructures of $La_{1-x}Sr_xFe_{0.9}Ni_{0.1}O_{3-\delta}$ as shown in Figure 3.18 were homogeneous and dense surface. It was noticed that the grain size of samples doping with Ni at the B-sites of $La_{1-x}Sr_xFeO_{3-\delta}$ were larger than those of $La_{1-x}Sr_xFe O_{3-\delta}$. The density and relative density are listed in Table 3.11.

Table 3.11 Density of $La_{1-x}Sr_xFe_{0.9}Ni_{0.1}O_{3-\delta}$ (x = 0.3-0.7) discs

Ratio	Density ($g.cm^3$)	Relative density (%)
x = 0.3	6.109	95.80
x = 0.4	6.018	95.49
x = 0.5	5.974	96.34
x = 0.6	5.722	94.13
x = 0.7	5.565	93.22

3.2.2.5 Morphologies of $La_{0.4}Sr_{0.6}Fe_{1-y}Ni_yO_{3-\delta}$ (y = 0.0-0.2)

The surface morphology of $La_{0.4}Sr_{0.6}Fe_{1-y}Ni_yO_{3-\delta}$ (y = 0.0-0.2) disc after sintered at 1200 °C for 15 hours were displayed in Figure 3.19.

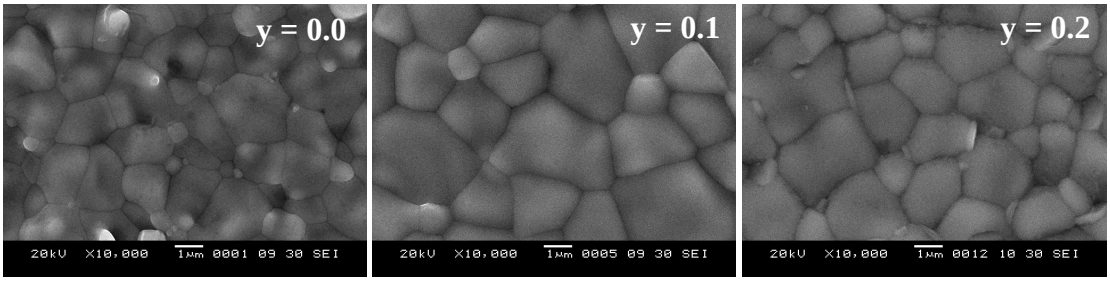

Figure 3.19 Surface morphology of $La_{0.4}Sr_{0.6}Fe_{1-y}Ni_yO_{3-\delta}$ (y = 0.0-0.2) discs.

The results show that all of the samples were homogeneous. It is seen that the grain size of 10% Ni-doped $La_{0.4}Sr_{0.6}FeO_{3-\delta}$ is slightly larger than that of $La_{0.4}Sr_{0.6}FeO_{3-\delta}$. It is noticed the increase amount of Ni substituted at Fe site has little effect on the grain size. The densities of $La_{0.4}Sr_{0.6}Fe_{1-y}Ni_yO_{3-\delta}$ discs were displayed in Table 3.12.

Table 3.12 Density of $La_{0.4}Sr_{0.6}Fe_{1-y}Ni_yO_{3-\delta}$ (y = 0.0-0.2) discs

Ratio	Density ($g.cm^3$)	Relative density (%)
y = 0.0	5.625	93.20
y = 0.1	5.722	94.13
y = 0.2	5.528	92.27

3.2.2.6 Morphologies of $La_{1-x}Sr_xFe_{0.9}Cu_{0.1}O_{3-\delta}$ (x = 0.3-0.7)

Figure 3.20 shows the SEM micrographs of $La_{1-x}Sr_xFe_{0.9}Cu_{0.1}O_{3-\delta}$ (x = 0.3-0.7) disc sintered at 1100 °C for 10 hours.

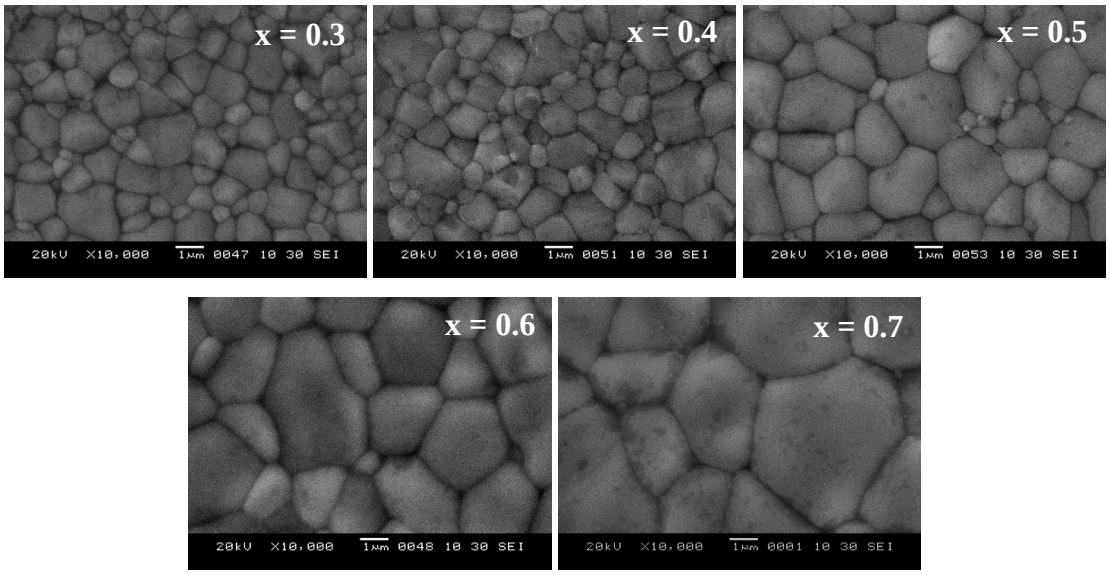

Figure 3.20 Surface morphology of $La_{1-x}Sr_xFe_{0.9}Cu_{0.1}O_{3-\delta}$ (x = 0.3-0.7) discs.

SEM micrograph of $La_{1-x}Sr_xFe_{0.9}Cu_{0.1}O_{3-\delta}$ (x = 0.3-0.7) show dense packed grain. It is observed that the grain sizes of Cu-substituted perovskite oxides were larger than the undoped oxide. These SEM images exhibited the larger grain size with the increase of Sr content. The relative density of $La_{1-x}Sr_xFe_{0.9}Cu_{0.1}O_{3-\delta}$ discs are more than 92% as displayed in Table 3.13.

Table 3.13 Density of $La_{1-x}Sr_xFe_{0.9}Cu_{0.1}O_{3-\delta}$ (x = 0.3-0.7) discs

Ratio	Density ($g.cm^3$)	Relative density (%)
x = 0.3	6.045	94.62
x = 0.4	5.883	92.96
x = 0.5	5.799	93.48
x = 0.6	5.749	94.53
x = 0.7	5.541	92.76

3.2.2.7 Morphologies of $La_{0.4}Sr_{0.6}Fe_{1-y}Cu_yO_{3-\delta}$ (y = 0.0-0.3)

Figure 3.21 shows the surface morphology of $La_{0.4}Sr_{0.6}Fe_{1-y}Cu_yO_{3-\delta}$ (y = 0.0-0.3) discs sintered at 1,100 °C for 6 hours.

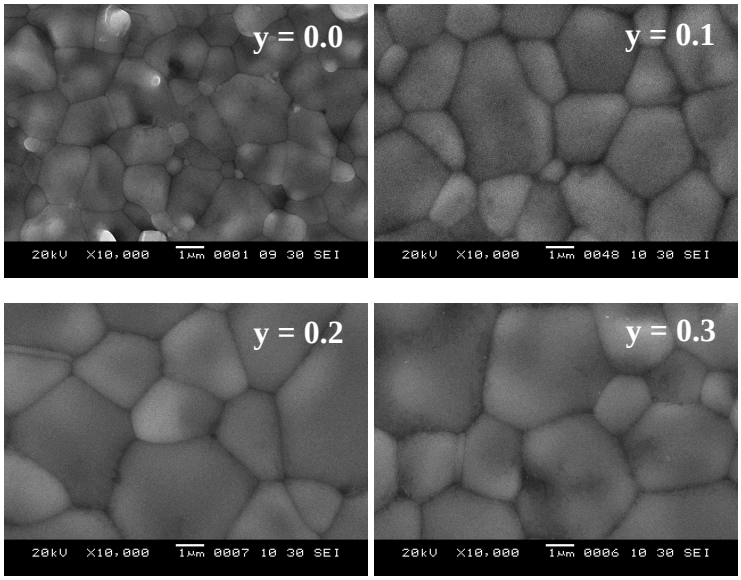

Figure 3.21 Surface morphology of $La_{0.4}Sr_{0.6}Fe_{1-y}Cu_yO_{3-\delta}$ (y = 0.0-0.3) discs.

The grain sizes increased with the increasing content of Cu as shown in Figure 3.14. $La_{0.4}Sr_{0.6}Fe_{0.7}Cu_{0.3}O_{3-\delta}$ has the highest grain sizes. As observed previously [48-49] the increase in particle size with the doping level is a result of a change in the melting point of the samples. Doping with copper decreases melting points of the materials, this effect results in an enhanced grain growth. The densities of $La_{0.4}Sr_{0.6}Fe_{1-y}Cu_yO_{3-\delta}$ with various amounts of Cu were listed in Table 3.14.

Table 3.14 Density of $La_{0.4}Sr_{0.6}Fe_{1-y}Cu_yO_{3-\delta}$ (y = 0.0-0.3) discs

Ratio	Density ($g.cm^3$)	Relative density (%)
y = 0.0	5.625	93.20
y = 0.1	5.749	94.53
y = 0.2	5.730	93.35
y = 0.3	5.694	92.64

The characterization by SEM is concluded that all samples exhibited high density (relative densities of sample discs are more than 92%) and had homogeneous surface. The grain sizes of $La_{1-x}Sr_xFeO_{3-\delta}$ increased with the increasing amount of Sr in A-site and increasing amount of Cu and Ni in B-site. Doping with 20 and 30% of Cr at B-site decreases the grain sizes.

3.3 Properties of the perovskite compounds

3.3.1 Electrical Conductivity

For the MIEC perovskite oxide, the co-presence of electronic holes and oxygen vacancies makes them simultaneously exhibit both electronic and ionic conductivities. The electrical conductivity of an oxide is given by the sum of partial conductivities of all mobile charged species as ions, electrons and holes. However, ionic conductivity in $La_{1-x}Sr_xFeO_{3-\delta}$ is small in comparison with the overall conductivity. The ion contribution does not exceed 1%, 3% and 5% of the overall conductivity for the compositions with x = 0.2, 0.5 and 0.9, respectively [50]. Assuming that the ionic conduction is negligibly small, the total conductivity can be mainly referred to electronic conductivity.

The total electrical conductivity of $La_{1-x}Sr_xFeO_{3-\delta}$ and $La_{1-x}Sr_xFe_{1-y}M_yO_{3-\delta}$ (M = Cr, Ni and Cu; x = 0.3-0.7; y = 0.0-0.3) has been investigated.

The electrical conductivity was measured with standard DC 4-probe technique using the rectangularly cut sintered samples in the temperature range from room temperature to 800 °C.

3.3.1.1 Electrical conductivity of $La_{1-x}Sr_xFeO_{3-\delta}$ (x = 0.3-0.7)

Electrical conducting property of $La_{1-x}Sr_xFeO_{3-\delta}$ (x = 0.3-0.7) were investigated as a function of temperature.

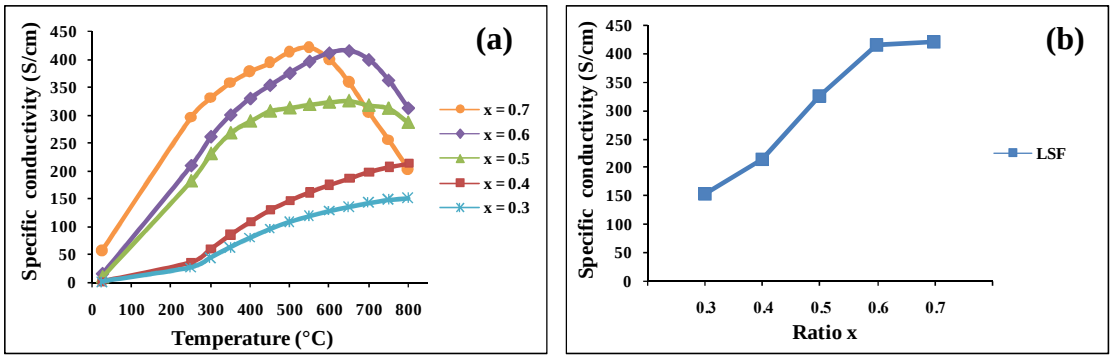

Figure 3.22 (a) Temperature dependence of the specific conductivity (σ) for $La_{1-x}Sr_xFeO_{3-\delta}$ (x = 0.3-0.7).
(b) Ratio x dependence of the maximum specific conductivity for $La_{1-x}Sr_xFeO_{3-\delta}$ (x = 0.3-0.7).

Table 3.15 Maximum specific conductivity of $La_{1-x}Sr_xFeO_{3-\delta}$ (x = 0.3-0.7)

Ratio	Maximum specific conductivity (S/cm)	Temperature (°C)
x = 0.0	1.004*	1,000*
x = 0.3	151.31	800
x = 0.4	212.33	800
x = 0.5	325.52	650
x = 0.6	414.78	650
x = 0.7	420.99	550

*from reference [51]

Our results illustrated that the electrical conductivity of $La_{1-x}Sr_xFeO_{3-\delta}$ increased with temperature within the region between room temperature to 800 °C, corresponding to the semiconducting property of these oxides when x = 0.3 and 0.4. While the Sr-doped $LaFeO_3$ with x = 0.5-0.7 showed semiconductive behavior between 25-650 °C and metallic property at higher temperature. However, the conductivity value of $La_{1-x}Sr_xFeO_{3-\delta}$ materials was enhanced by doping Sr at A-site. As displayed in Figure 3.22 and Table 3.15, the specific conductivity of $La_{0.3}Sr_{0.7}FeO_{3-\delta}$ reached the maximum value of 420.99 S/cm at about 550 °C.

In Table 3.15, when x increases from 0 to 0.7, the value of maximum specific conductivity increases whereas the temperature at maximum specific conductivity decreases from 1,000 to 550 °C. The partial replacement of trivalent lanthanum for divalent strontium results in increasing electrical conductivity of $LaFeO_3$, and rather intensive formation of oxygen vacancies competing with the oxidation of the iron. In order to discuss the possible responses of an oxide system, two extremes need to be considered on the introduction of the dopants (Sr^{2+}). The formation of oxygen vacancies occur when the oxidation state of the iron cations (+3) remains unchanged. Electronic compensation involves only a change of the oxidation state of iron cations from +3 to +4, which may be interpreted as an appearance of electron holes associated with Fe^{4+} cations [50]. Since the partial replacement of La by Sr affects the formation of both oxygen vacancies ($[V_O^{\bullet\bullet}]$) and Fe^{4+} ($[Fe_{Fe}^{\bullet}]$). The individual defect equilibrium can be expressed as following (Kröger-Vink notation has been used through this discussion).

$$[Sr'_{La}] = [Fe_{Fe}^{\bullet}] + [V_O^{\bullet\bullet}] \quad (3.1)$$

The assumption can be made that the electronic conduction is caused by the exchange of electron holes between Fe ions of different valence states [52], where the concentration of oxygen vacancies is always relatively small. It can be suggested that the addition of Sr into La sites increases the *p*-type conductivity.

The Arrhenius plot of $La_{1-x}Sr_xFeO_{3-\delta}$ (x = 0.3-0.7) is given in Figure 3.23. Its linear part can be described by the formula:

$$\sigma = (A/T) \exp(-E_a/kT) \quad (3.2)$$

where A is material constant including the carrier concentration term, E_a is the activation energy, k is the Boltzmann's constant and T is the absolute temperature. The activation energy calculated from the linear part of Arrhenius plot (Figure 3.23) is listed in Table 3.16. It can be clearly seen that the activation energy of $La_{1-x}Sr_xFeO_{3-\delta}$ decreased with the increase of the Sr content. According to these results, $La_{0.3}Sr_{0.7}FeO_{3-\delta}$ showed the lowest activation energy, corresponding to the highest specific conductivity.

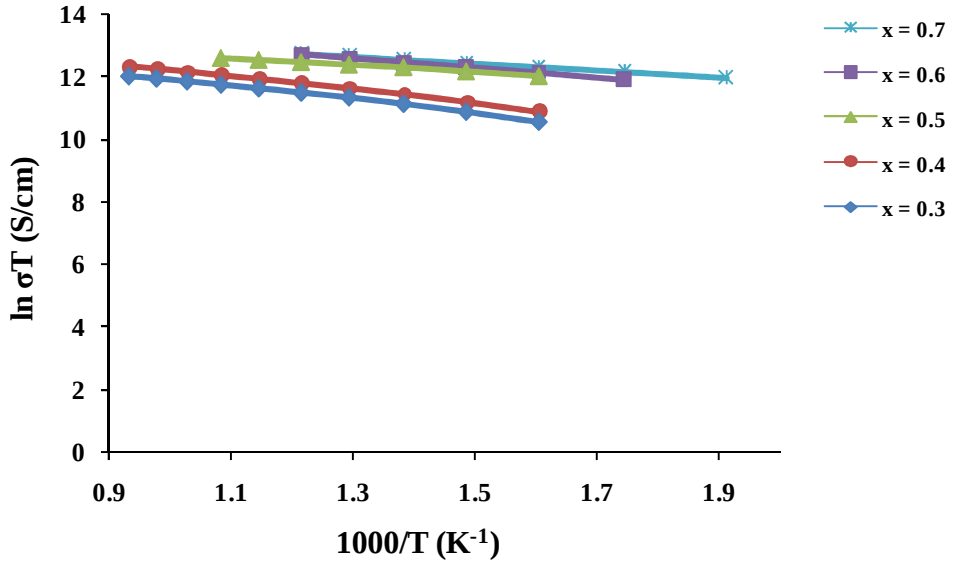

Figure 3.23 Arrhenius plot of the electrical conductivity of $La_{1-x}Sr_xFeO_{3-\delta}$ (x = 0.3-0.7).

Table 3.16 Activation energy of $La_{1-x}Sr_xFeO_{3-\delta}$ (x = 0.3-0.7)

Ratio	E_a (kJ/mol)
x = 0.3	17.77
x = 0.4	17.26
x = 0.5	12.06
x = 0.6	11.30
x = 0.7	10.10

3.3.1.2 Electrical conductivity of $La_{1-x}Sr_xFe_{0.9}Cr_{0.1}O_{3-\delta}$ (x = 0.3-0.7)

Figure 3.24 and Table 3.17 shows the temperature dependence of specific conductivity of $La_{1-x}Sr_xFe_{0.9}Cr_{0.1}O_{3-\delta}$ (x = 0.3-0.7) in air.

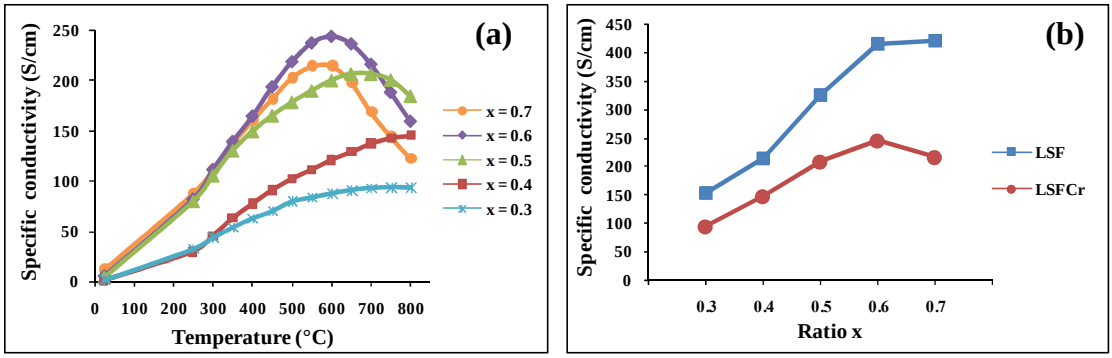

Figure 3.24 (a) Temperature dependence of the specific conductivity (σ) for $La_{1-x}Sr_xFe_{0.9}Cr_{0.1}O_{3-\delta}$ (x = 0.3-0.7).
(b) Ratio x dependence of the maximum specific conductivity for $La_{1-x}Sr_xFeO_{3-\delta}$ and $La_{1-x}Sr_xFe_{0.9}Cr_{0.1}O_{3-\delta}$ (x = 0.3-0.7).

Table 3.17 Maximum specific conductivity of $La_{1-x}Sr_xFe_{0.9}Cr_{0.1}O_{3-\delta}$ (x = 0.3-0.7)

Ratio	Maximum specific conductivity (S/cm)	Temperature (°C)
x = 0.3	93.76	800
x = 0.4	145.55	800
x = 0.5	206.56	650
x = 0.6	244.00	600
x = 0.7	214.47	600

The temperature dependence of the specific conductivity for all specimens is shown in Figure 3.24. The total conductivity of $La_{1-x}Sr_xFe_{0.9}Cr_{0.1}O_{3-\delta}$ in air is predominantly electronic and increases with temperature (Figure 3.24). The

electrical conductivity of $La_{1-x}Sr_xFe_{0.9}Cr_{0.1}O_{3-\delta}$ (x = 0.5-0.7) exhibits a semiconductor-type behavior from room temperature to 650 °C, whilst further heating leads to an apparent transition to pseudometallic conduction. As for other ferrites [53], the pseudometallic behavior at high temperatures is associated, most likely, with a decrease in concentration of *p*-type charge carriers due to an increase in oxygen nonstoichiometry on heating.

Figure 3.24 (b) demonstrated that the chromium doping of $La_{1-x}Sr_xFeO_{3-\delta}$ (x = 0.3-0.7) results in decreasing conductivity. Since Cr^{3+} cation is the most stable oxidation state and Cr^{4+} ion is rare [54], their incorporation into the B sublattice of $La_{1-x}Sr_xFeO_{3-\delta}$ decreases the total concentration of B-sites participating in the electronic transport, and also the absolute concentration of Fe^{4+} ions which represent *p*-type charge carriers.

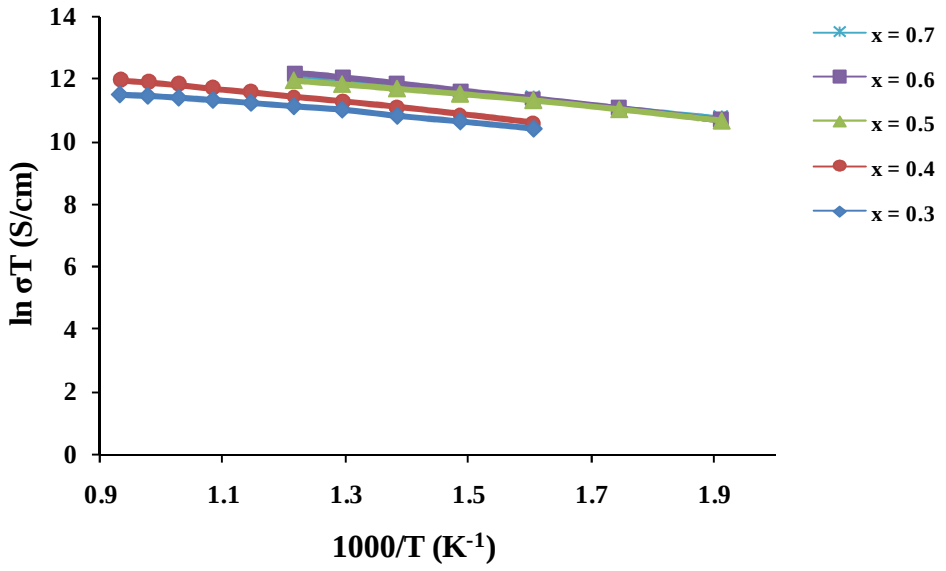

Figure 3.25 Arrhenius plot of the specific conductivity of $La_{1-x}Sr_xFe_{0.9}Cr_{0.1}O_{3-\delta}$ (x = 0.3-0.7).

Table 3.18 Activation energy of $La_{1-x}Sr_xFe_{0.9}Cr_{0.1}O_{3-\delta}$ (x = 0.3-0.7)

Ratio	E_a (kJ/mol)
x = 0.3	18.09
x = 0.4	17.01
x = 0.5	16.31
x = 0.6	13.72
x = 0.7	15.67

The Arrhenius plot of the specific conductivity and the activation energy of $La_{1-x}Sr_xFe_{0.9}Cr_{0.1}O_{3-\delta}$ (x = 0.3-0.7) are displayed in Figure 3.25 and Table 3.18, respectively. It can be observed that the activation energy of $La_{1-x}Sr_xFeO_{3-\delta}$ increased with the addition of chromium.

3.3.1.3 Electrical conductivity of $La_{0.4}Sr_{0.6}Fe_{1-y}Cr_yO_{3-\delta}$ (y = 0.0-0.3)

The temperature dependence of the specific conductivity for the $La_{0.4}Sr_{0.6}Fe_{1-y}Cr_yO_{3-\delta}$ (y = 0.0-0.3) samples is shown in Figure 3.26.

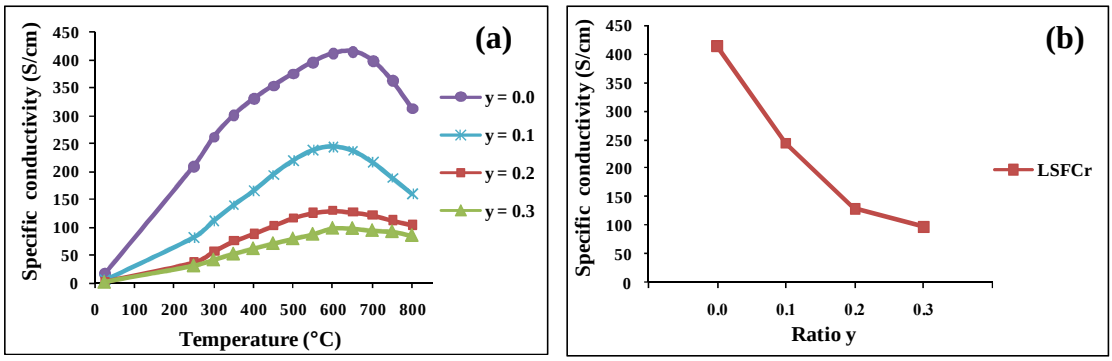

Figure 3.26 (a) Temperature dependence of the specific conductivity (σ) for $La_{0.4}Sr_{0.6}Fe_{1-y}Cr_yO_{3-\delta}$ (y = 0.0-0.3).
(b) Ratio y dependence of the maximum specific conductivity for $La_{0.4}Sr_{0.6}Fe_{1-y}Cr_yO_{3-\delta}$ (y = 0.0-0.3).

Table 3.19 Maximum specific conductivity of $La_{0.4}Sr_{0.6}Fe_{1-y}Cr_yO_{3-\delta}$ (y = 0.0-0.3)

Ratio	Maximum specific conductivity (S/cm)	Temperature (°C)
y = 0.0	414.78	650
y = 0.1	244.00	600
y = 0.2	128.93	600
y = 0.3	97.70	600

Figure 3.26 (a) shows two regions of conductivity. In the lower region (at room temperature to 650 °C), the Cr-doped oxide is semiconductor while these perovskites show metallic conductivity at higher temperature region. The electrical conductivity of $La_{0.4}Sr_{0.6}Fe_{1-y}Cr_yO_{3-\delta}$ (y = 0.0-0.3) is essentially dependent of chromium content. The electrical conductivity of $La_{0.4}Sr_{0.6}Fe_{1-y}Cr_yO_{3-\delta}$ decreases dramatically with chromium addition. It can be explained that the increase of

chromium content causes the concentration of Fe^{4+} ions in the structure to be reduced. Thus, the electrical conductivity decreases. In addition, processing conditions may affect the conductivity of perovskite oxides, probably due to an extremely important role of grain boundaries [55]. In case of $La_{0.4}Sr_{0.6}Fe_{0.7}Cr_{0.3}O_{3-\delta}$, it exhibited smallest grains (Figure 3.17), enhancing the amount of grain boundaries and then the conductivity decreased. The maximum specific conductivity of $La_{0.4}Sr_{0.6}Fe_{0.7}Cr_{0.3}O_{3-\delta}$ was the lowest (97.7 S/cm at about 600 °C) and it is about four times less than that of undoped $La_{1-x}Sr_xFeO_{3-\delta}$ (414.78 S/cm at about 650 °C).

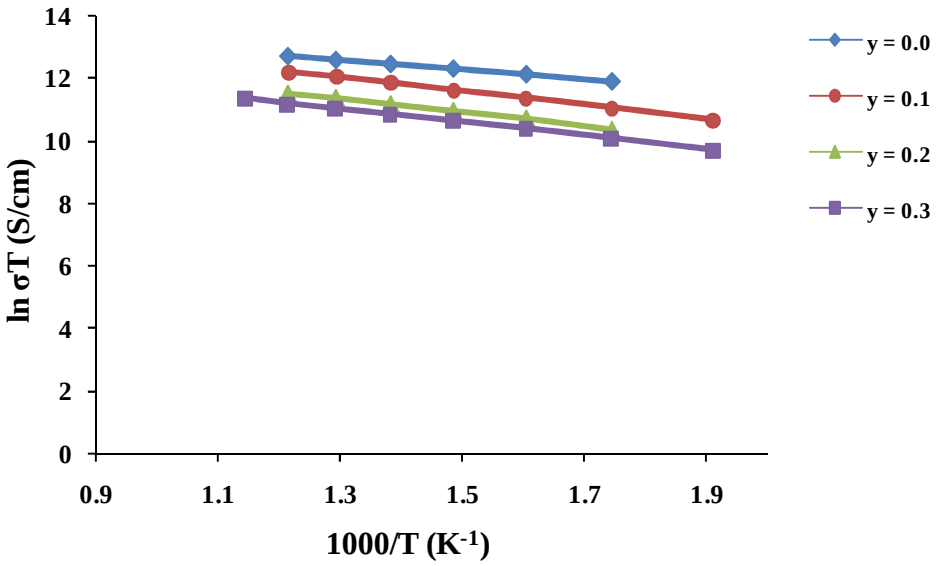

Figure 3.27 Arrhenius plot of the specific conductivity of $La_{0.4}Sr_{0.6}Fe_{1-y}Cr_yO_{3-\delta}$ (y = 0.0-0.3).

Table 3.20 Activation energy of $La_{0.4}Sr_{0.6}Fe_{1-y}Cr_yO_{3-\delta}$ (y = 0.0-0.3)

Ratio	E_a (kJ/mol)
y = 0.0	11.30
y = 0.1	13.72
y = 0.2	17.59
y = 0.3	18.12

The activation energy values of $La_{0.4}Sr_{0.6}Fe_{1-y}Cr_yO_{3-\delta}$ (y = 0.0-0.3) specimens calculated from the linear part of Figure 3.27 are shown in Table 3.20. The activation energy increases with the amount of chromium. The activation energy of

$La_{0.4}Sr_{0.6}$ $Fe_{1-y}Cr_yO_{3-\delta}$ is higher than that of $La_{1-x}Sr_xFeO_{3-\delta}$ corresponding to the lower specific conductivity of $La_{0.4}Sr_{0.6}Fe_{1-y}Cr_yO_{3-\delta}$.

3.3.1.4 Electrical conductivity of $La_{1-x}Sr_xFe_{0.9}Ni_{0.1}O_{3-\delta}$ (x = 0.3-0.7)

The electrical conducting property of $La_{1-x}Sr_xFe_{0.9}Ni_{0.1}O_{3-\delta}$ (x = 0.3-0.7) was investigated as a function of temperature.

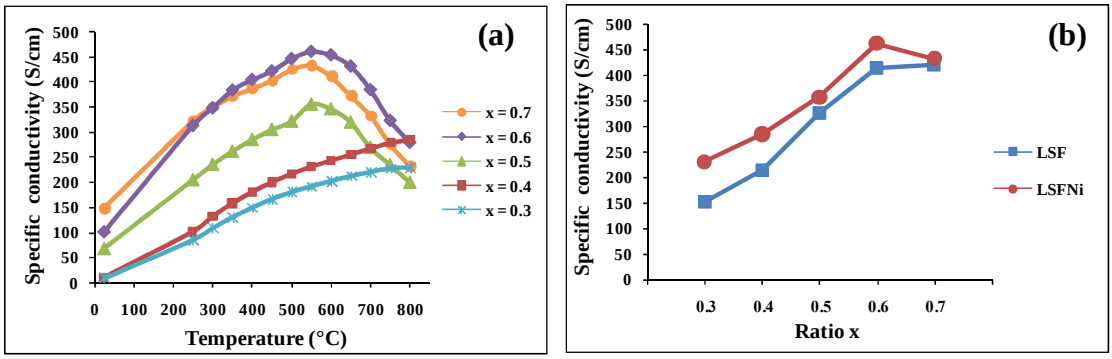

Figure 3.28 (a) Temperature dependence of the specific conductivity (σ) for $La_{1-x}Sr_xFe_{0.9}Ni_{0.1}O_{3-\delta}$ (x = 0.3-0.7).
(b) Ratio x dependence of the maximum specific conductivity for $La_{1-x}Sr_xFeO_{3-\delta}$ and $La_{1-x}Sr_xFe_{0.9}Ni_{0.1}O_{3-\delta}$ (x = 0.3-0.7).

Table 3.21 Maximum specific conductivity of $La_{1-x}Sr_xFe_{0.9}Ni_{0.1}O_{3-\delta}$ (x = 0.3-0.7)

Ratio	Maximum specific conductivity (S/cm)	Temperature (°C)
x = 0.3	230.06	800
x = 0.4	283.67	800
x = 0.5	356.34	550
x = 0.6	460.72	550
x = 0.7	432.41	550

In this study, the electrical conductivity was studied in the temperature range from room temperature to 800 °C. The temperature dependence of the specific conductivity for $La_{1-x}Sr_xFe_{0.9}Ni_{0.1}O_{3-\delta}$ (x = 0.3-0.7) is shown in Figure 3.28 and it showed the same pattern as Figures 3.22 and 3.24. It revealed that the specific conductivity increases with temperature, indicating the semiconductor nature of the lanthanum ferrite system. Table 3.21 summarizes the specific conductivity as a function of Ni-substituted concentration for $La_{1-x}Sr_xFe$ $O_{3-\delta}$. The conductivity values

of $La_{1-x}Sr_xFeO_{3-\delta}$ increase with Ni doping in the sample. The maximum specific conductivity, $\sigma_{550°C}$ = 460.72 S/cm, is found for $La_{0.4}Sr_{0.6}Fe_{0.9}Ni_{0.1}O_{3-\delta}$ specimen. It is possible that high electronic conductivity of $La_{1-x}Sr_xFe_{0.9}Ni_{0.1}O_{3-\delta}$ might be related to the charge transfer of B-site. Charge compensation for the introduction of strontium at the A-sites induces the charge change from Fe^{3+} to Fe^{4+} and Ni^{2+} to Ni^{3+} and/or Ni^{4+} [41]. In this case, the concentration of electronic holes increases thereby enhancing *p*-type conductivity.

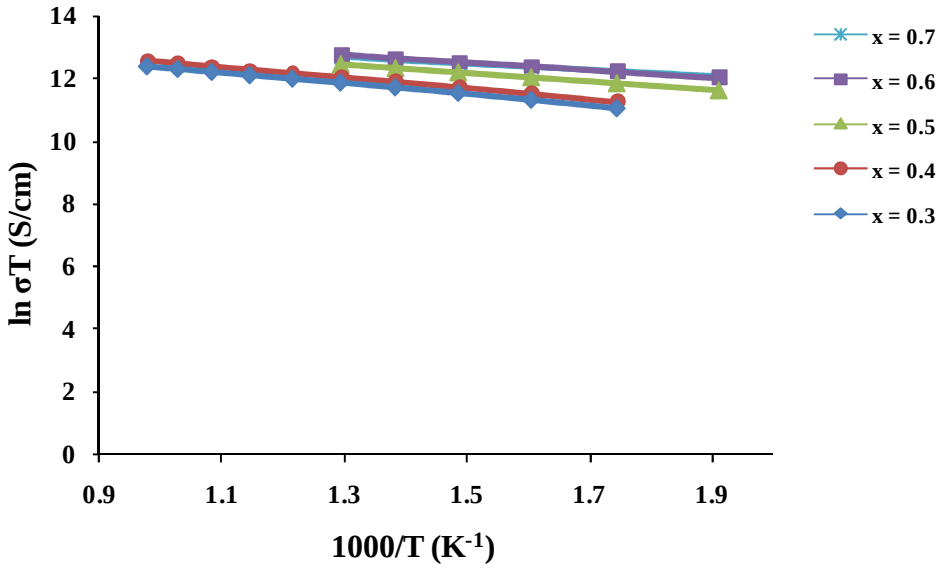

Figure 3.29 Arrhenius plot of the electrical conductivity of $La_{1-x}Sr_xFe_{0.9}Ni_{0.1}O_{3-\delta}$ (x = 0.3-0.7).

Table 3.22 Activation energy of $La_{1-x}Sr_xFe_{0.9}Ni_{0.1}O_{3-\delta}$ (x = 0.3-0.7)

Ratio	E_a (kJ/mol)
x = 0.3	14.21
x = 0.4	14.20
x = 0.5	9.59
x = 0.6	8.85
x = 0.7	9.24

Activation energy for the conduction is obtained by plotting the electrical conductivity data in Arrhenius relation, as displayed in Table 3.22. It can be seen that the substitution of the nickel 0.1 mol makes the activation energy of $La_{1-x}Sr_x$ $FeO_{3-\delta}$ decreased.

3.3.1.5 Electrical conductivity of $La_{0.4}Sr_{0.6}Fe_{1-y}Ni_yO_{3-\delta}$ (y = 0.0-0.2)

Figure 3.30 and Table 3.23 show temperature dependence of the specific conductivity of $La_{0.4}Sr_{0.6}Fe_{1-y}Ni_yO_{3-\delta}$ (y = 0.0-0.2) in air.

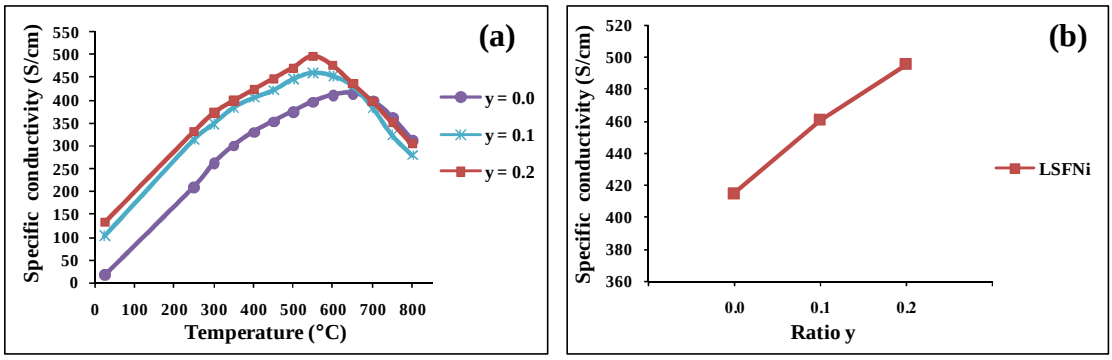

Figure 3.30 (a) Temperature dependence of the specific conductivity (σ) for $La_{0.4}Sr_{0.6}Fe_{1-y}Ni_yO_{3-\delta}$ (y = 0.0-0.2).
(b) Ratio y dependence of the maximum specific conductivity for $La_{0.4}Sr_{0.6}Fe_{1-y}Ni_yO_{3-\delta}$ (y = 0.0-0.2).

Table 3.23 Maximum specific conductivity of $La_{0.4}Sr_{0.6}Fe_{1-y}Ni_yO_{3-\delta}$ (y = 0.0-0.2)

Ratio	Maximum specific conductivity (S/cm)	Temperature (°C)
y = 0.0	414.78	650
y = 0.1	460.72	550
y = 0.2	495.46	550

DC electrical conductivity of $La_{0.4}Sr_{0.6}Fe_{1-y}Ni_yO_{3-\delta}$ (y = 0.0-0.2) was measured in air as a function of temperature as shown in Figure 3.30. The specific conductivity increased with temperature and nickel content. With increasing nickel content in B-sites, the conductivity increases as expected due to the enhancement of the total concentration of Ni^{3+} and Ni^{4+} at B-sites. The change of nickel charge from +2 to +3 and/or +4 might cause the electron holes that participate in the electronic transport process [41]. The highest specific conductivity value is obtained from the sample with the highest Ni-content on B-site ($\sigma_{550\ °C}$ = 495.46 S/cm at about 550 °C).

The activation energy values of $La_{0.4}Sr_{0.6}Fe_{1-y}Ni_yO_{3-\delta}$ (y = 0.0-0.2) specimens calculated from the linear part of Arrhenius plot in Figure 3.31 are listed in Table 3.24. Our results indicated that the activation energy of $La_{0.4}Sr_{0.6}Fe_{1-y}Ni_yO_{3-\delta}$ is less than that of $La_{0.4}Sr_{0.6}FeO_{3-\delta}$.

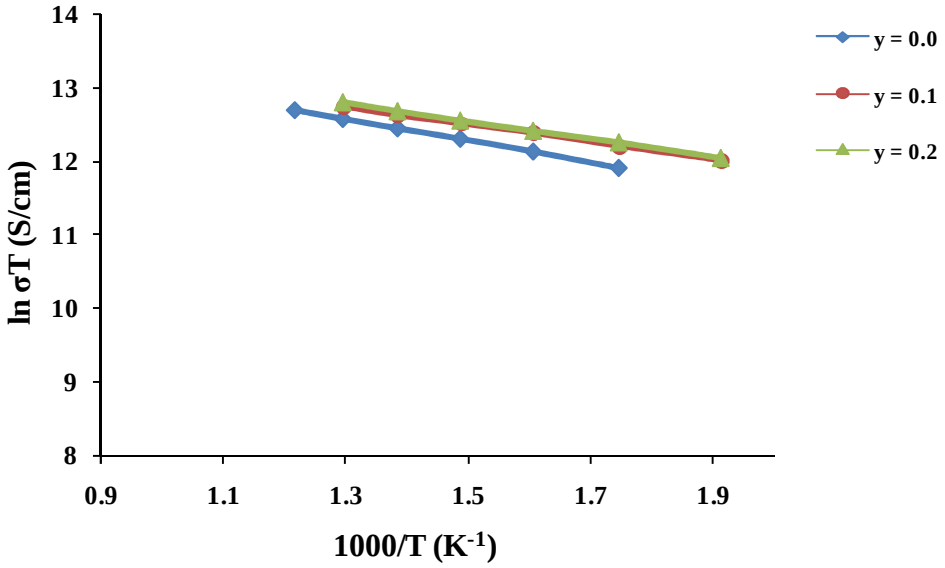

Figure 3.31 Arrhenius plot of the electrical conductivity of $La_{0.4}Sr_{0.6}Fe_{1-y}Ni_yO_{3-\delta}$ (y = 0.0-0.2).

Table 3.24 Activation energy of $La_{0.4}Sr_{0.6}Fe_{1-y}Ni_yO_{3-\delta}$ (y = 0.0-0.2)

Ratio	E_a (kJ/mol)
y = 0.0	11.30
y = 0.1	8.85
y = 0.2	8.53

3.3.16 Electrical conductivity of $La_{1-x}Sr_xFe_{0.9}Cu_{0.1}O_{3-\delta}$ (x = 0.3-0.7)

The temperature dependence of the specific conductivity of the $La_{1-x}Sr_xFe_{0.9}Cu_{0.1}O_{3-\delta}$ (x = 0.3-0.7) samples is displayed in Figure 3.32 and Table 3.25.

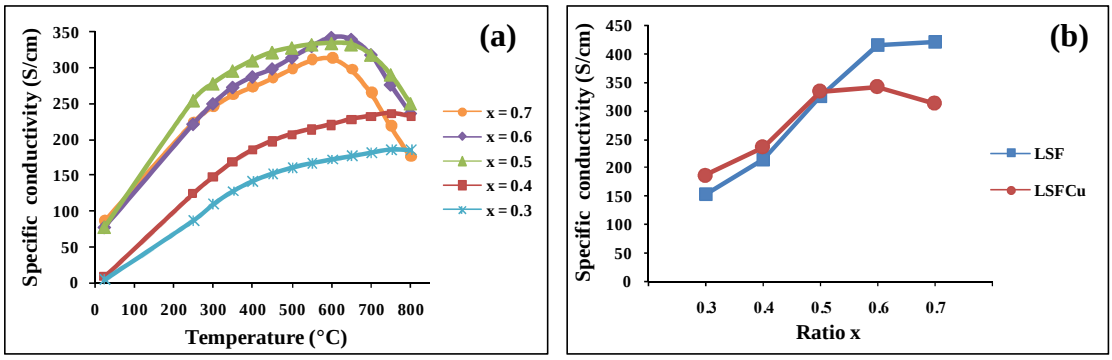

Figure 3.32 (a) Temperature dependence of the specific conductivity (σ) for $La_{1-x}Sr_xFe_{0.9}Cu_{0.1}O_{3-\delta}$ (x = 0.3-0.7).
(b) Ratio x dependence of the maximum specific conductivity for $La_{1-x}Sr_xFeO_{3-\delta}$ and $La_{1-x}Sr_xFe_{0.9}Cu_{0.1}O_{3-\delta}$ (x = 0.3-0.7).

Table 3.25 Maximum specific conductivity of $La_{1-x}Sr_xFe_{0.9}Cu_{0.1}O_{3-\delta}$ (x = 0.3-0.7)

Ratio	Maximum specific conductivity (S/cm)	Temperature (°C)
x = 0.3	186.28	750
x = 0.4	235.69	750
x = 0.5	333.97	600
x = 0.6	341.87	600
x = 0.7	312.84	600

Electrical conductivity measurements were recorded as a function of temperature in the $La_{1-x}Sr_xFe_{0.9}Cu_{0.1}O_{3-\delta}$ system, for x values of 0.3 to 0.7. Figure 3.25 depicts the same manner as Figure 3.21. It can be seen that Cu doping at B-site is not as effective as Sr doping at A-site for improving the conductivity (Table 3.25 and Figure 3.32). Partial addition of Cu at the Fe site causes the increase of specific conductivity and reduces the temperature of the maximum specific conductivity. Figure 3.32 illustrates that the conductivity of $La_{1-x}Sr_xFe_{0.9}Cu_{0.1}O_{3-\delta}$ increases with Sr content at x = 0.3-0.5. It is indicated that 10% Cu doping at the Fe site can improve the conductivity of $La_{1-x}Sr_xFeO_{3-\delta}$ and lower the temperature of maximum specific conductivity at some Sr contents. When the amount of Sr changes from 50% to 70%,

the maximum specific conductivity becomes lower. The decrease of the conductivity is mainly associated with the loss of the lattice oxygen and the reduction of the B-site (Fe ions) at elevated temperature [56].

Calculated from the slope of log (σ·T) versus 1000/T plots, the activation energy values of $La_{1-x}Sr_xFe_{0.9}Cu_{0.1}O_{3-\delta}$ specimens are shown in Table 3.26. It could be seen that the activation energy of $La_{1-x}Sr_xFeO_{3-\delta}$ decreased with copper replacement at B-site.

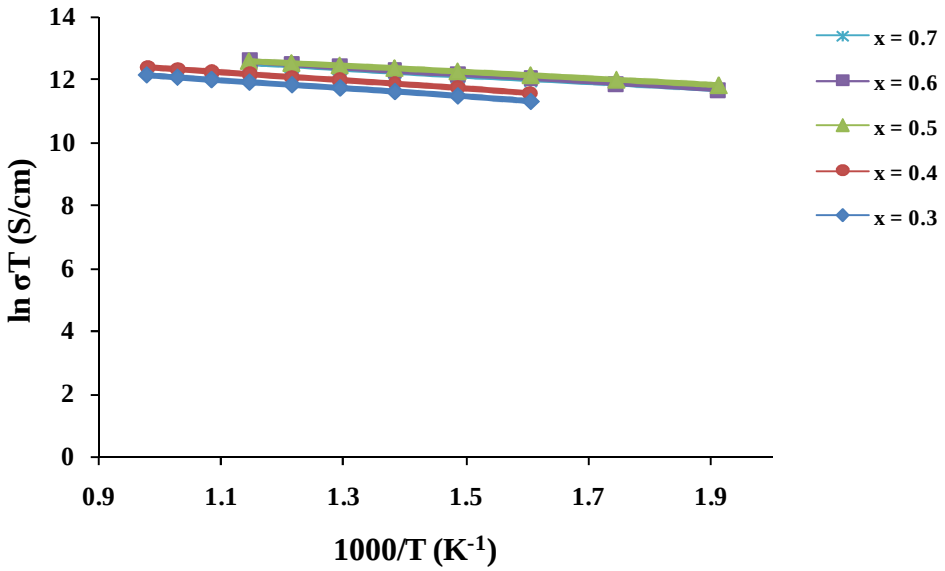

Figure 3.26 Arrhenius plot of the electrical conductivity of $La_{1-x}Sr_xFe_{0.9}Cu_{0.1}O_{3-\delta}$ (x = 0.3-0.7).

Table 3.26 Activation energy of $La_{1-x}Sr_xFe_{0.9}Cu_{0.1}O_{3-\delta}$ (x = 0.3-0.7)

Ratio	E_a (kJ/mol)
x = 0.3	11.38
x = 0.4	10.92
x = 0.5	9.92
x = 0.6	9.02
x = 0.7	9.86

3.3.1.5 Electrical conductivity of $La_{0.4}Sr_{0.6}Fe_{1-y}Cu_yO_{3-\delta}$ (y = 0.0-0.3)

Figure 3.34 and Table 3.27 shows the temperature dependence of specific conductivity of $La_{0.4}Sr_{0.6}Fe_{1-y}Cu_yO_{3-\delta}$ (y = 0.0-0.3) in air.

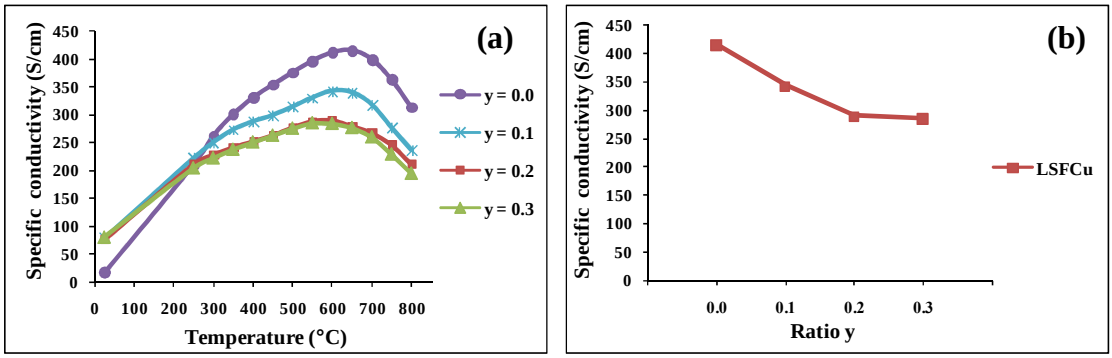

Figure 3.34 (a) Temperature dependence of the specific conductivity (σ) for $La_{0.4}Sr_{0.6}Fe_{1-y}Cu_yO_{3-\delta}$ (y = 0.0-0.3).
(b) Ratio y dependence of the maximum specific conductivity for $La_{0.4}Sr_{0.6}Fe_{1-y}Cu_yO_{3-\delta}$ (y = 0.0-0.3).

Table 3.27 Maximum specific conductivity of $La_{0.4}Sr_{0.6}Fe_{1-y}Cu_yO_{3-\delta}$ (y = 0.0-0.3)

Ratio	Maximum specific conductivity (S/cm)	Temperature (°C)
y = 0.0	414.78	650
y = 0.1	341.87	600
y = 0.2	288.67	600
y = 0.3	284.24	550

In Figure 3.34 and Table 3.27, the electrical conductivity that was measured in air as a function of temperature indicated a semiconducting behavior of Cu doped $La_{0.4}Sr_{0.6}FeO_{3-\delta}$ up to 650 °C. The specific conductivity of each composition increased with temperature up to their maximum specific conductivity value and then decreased. Figure 3.34 (b) showed that the substitution of 20-30% Fe^{3+} by Cu^{2+} led to positive charge deficiency, which is compensated by oxygen vacancies. The conductivity of $La_{0.4}Sr_{0.6}Fe_{1-y}Cu_yO_{3-\delta}$ decreased with Cu content, the increasing of oxide ion vacancies might cause a decreasing in electrical conductivity. The vacancies could also act as random trap for electrons, resulting in the decrease of the carrier mobility [56] and finally charge carrier concentration. It was indicated that Cu doping at the Fe site cannot improved the electrical conductivity of $La_{0.4}Sr_{0.6}FeO_{3-\delta}$.

Shown in Table 3.28, the activation energy values of Cu specimens were calculated from the linear part of Figure 3.35. It can be observed that the activation energy of $La_{0.4}Sr_{0.6}Fe_{1-y}Cu_yO_{3-\delta}$ (x = 0.1-0.3) was less than that of $La_{0.4}Sr_{0.6}FeO_{3-\delta}$ and the activation energy increases with the amount of copper corresponding to the lower specific conductivity of $La_{0.4}Sr_{0.6}Fe_{1-y}Cu_yO_{3-\delta}$.

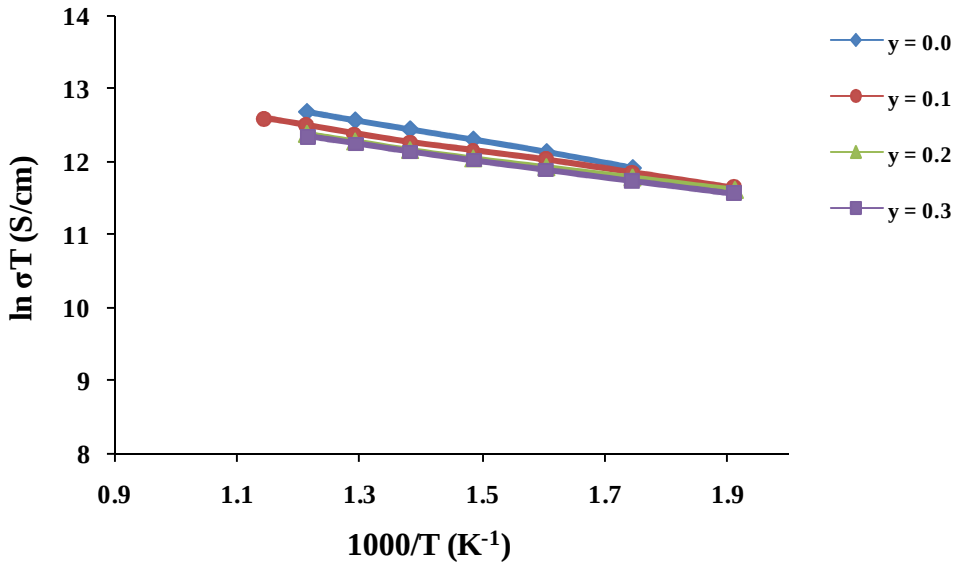

Figure 3.35 Arrhenius plot of the electrical conductivity of $La_{0.4}Sr_{0.6}Fe_{1-y}Cu_yO_{3-\delta}$ (y = 0.0-0.3).

Table 3.28 Activation energy of $La_{0.4}Sr_{0.6}Fe_{1-y}Cu_yO_{3-\delta}$ (y = 0.0-0.3)

Ratio	E_a (kJ/mol)
y = 0.0	11.30
y = 0.1	9.02
y = 0.2	9.22
y = 0.3	9.38

Table 3.29 Activation energy compilation for perovskite

Sample	E_a (kJ/mol)	Reference
$La_{0.4}Sr_{0.6}Fe_{0.8}Ni_{0.2}O_{3-\delta}$	8.53	This work
$La_{0.7}Sr_{0.3}Fe_{0.8}Ni_{0.2}O_{3-\delta}$	11.90	[41]
$La_{0.7}Sr_{0.3}Fe_{0.8}Cu_{0.2}O_{3-\delta}$	13.76	[41]
$La_{0.7}Sr_{0.3}Fe_{0.8}Mn_{0.2}O_{3-\delta}$	17.54	[41]
$La_{0.7}Sr_{0.3}Fe_{0.8}Al_{0.2}O_{3-\delta}$	21.46	[41]

From the conductivity results, it can be concluded that partial substitution of Sr at the A-site is crucial to increase the conductivity performance at lower temperature. For x = 0.7, the specific conductivity of $La_{1-x}Sr_xFeO_{3-\delta}$ shows the highest value which is 420.99 S/cm at 550 °C. By replacing Fe with Cr, Ni and Cu, the enhancement of $La_{1-x}Sr_xFeO_{3-\delta}$ conductivity can only be achieved with Ni doping. The highest specific conductivity obtained from this work is 495.46 S/cm for $La_{0.4}Sr_{0.6}Fe_{0.8}Ni_{0.2}O_{3-\delta}$ at about 550 °C.

3.3.2 Thermal expansion coefficients

Since SOFCs operate at high temperatures and should endure the thermal cycle from room temperature to operating temperature. Materials of SOFCs must be thermally compatible with the other cell components. Therefore, the thermal expansion coefficient (TEC) of materials must be close to those of the other cell components to minimize the thermal stresses.

The thermal expansions were measured by using a dilatometer (NETZSCH DIL 402C) in the temperature range from room temperature to 800 °C. Measurements were performed at a heating rate of 10 °C/min and data acquisition of the differential length and the temperature was conducted every 10 s. No weight change of the sample was observed before and after the measurement.

3.3.2.1 Thermal expansion coefficients of $La_{1-x}Sr_xFeO_{3-\delta}$ (x = 0.3-0.7)

Dilatometric curves for the $La_{1-x}Sr_xFeO_{3-\delta}$ (x = 0.3-0.7) in air are shown in Figure 3.36 (a). The average thermal expansion coefficient (TEC) is defined as the slope of dilatometric curves, are displayed in Figure 3.36 (b) and Table 3.29.

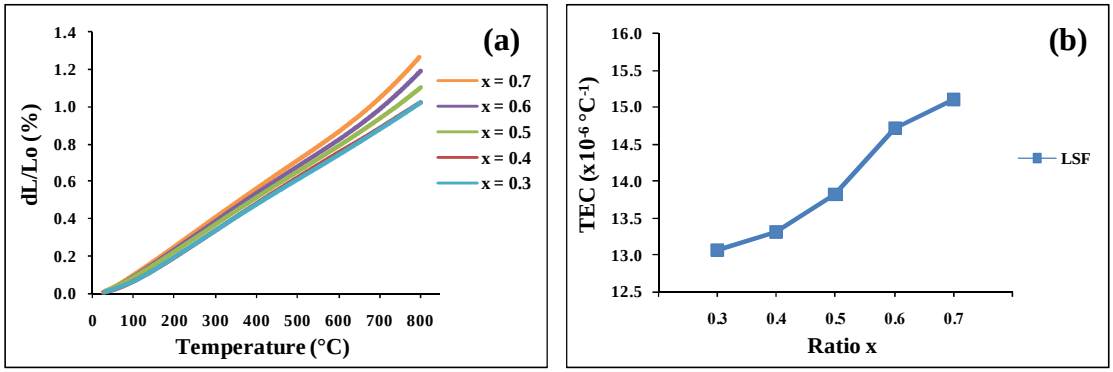

Figure 3.36 (a) Temperature dependence of the thermal expansion for $La_{1-x}Sr_xFeO_{3-\delta}$ (x = 0.3-0.7).
(b) Ratio x dependence of the TEC for $La_{1-x}Sr_xFeO_{3-\delta}$ (x = 0.3-0.7).

Lanthanum ferrite was doped by strontium in order to improve ionic and electronic conductivities. The ionic conductivity is related to the concentration of oxygen vacancies and the electronic conductivity is related to hole concentration. The partial substitution of lanthanum by strontium can lead to the creation of oxygen vacancies and holes, according to the reactions (3.2) and (3.3):

$$2\ SrO \xrightarrow{LaFeO_3} 2\ Sr_{La}' + V_O^{\bullet\bullet} + 2\ O_O^x \qquad (3.3)$$

$$\frac{1}{2}O_2 + 2\ SrO \xrightarrow{LaFeO_3} 2\ Sr_{La}' + 2\ h^{\bullet} + 3\ O_O^x \qquad (3.4)$$

$$Fe_{Fe}^x + h^{\bullet} \longrightarrow Fe_{Fe}^{\bullet} \qquad (3.5)$$

$$O_O^x + 2\ Fe_{Fe}^{\bullet} \longleftrightarrow \frac{1}{2}O_2 + V_O^{\bullet\bullet} + 2\ Fe_{Fe}^x \qquad (3.6)$$

Reaction (3.6) represents the global equilibrium between reactions (3.4) and (3.5).

TEC values of perovskites were measured for various strontium contents from LSF 731 to LSF 371 under air (Figure 3.36). The perovskite oxides expanded almost linearly in the temperature range 25-600 °C but they became steeper at high temperature. In the low temperature range, the substitution of lanthanum by strontium from x = 0.3-0.7 leads to a TEC variation in the range of 13.07 up to 15.10 $\times 10^{-6}$ $°C^{-1}$ under air. TEC is affected by strontium content in the low temperature range. Indeed in this range, the thermal expansion is only the result of lattice vibrations. In the high temperature range, the TEC increases from 13.33 up to

16.51×10^{-6} °C^{-1} in air, the concentration of oxygen vacancies increases with strontium content (reaction (3.3)) according to the relationship of electroneutrality conservation [57].

On the other hand [41], reaction (3.6) involves the creation of oxygen vacancies and the reduction of the valence state of iron from Fe^{4+} ($Fe_{Fe}^{\bullet}$) to Fe^{3+} (Fe_{Fe}^{x}) due to temperature. The volume expansion of the material is due to this reduction of Fe with increasing ionic radii (r_{Fe}^{4+} = 0.585 A° ; r_{Fe}^{3+} = 0.645 A°) and to oxygen vacancies with an increase of the electrostatic repulsion between the cations. The result of these chemical-induced mechanisms is a deformation and an increase of the unit cell volume. Therefore, thermal reduction of Fe^{4+} to Fe^{3+} and the formation of oxygen vacancies enhanced the thermal expansion coefficient.

The thermal expansion coefficient calculated from the slopes of the thermal expansion curves of Figure 3.36 (a). The thermal expansion of $La_{0.7}Sr_{0.3}FeO_3$ at 50-800 °C measured in this work is less than previous work. This work was synthesized from the modified citrate method but previous work using different methods and conditions. TEC values of $La_{1-x}Sr_xFeO_{3-\delta}$ can be improved by using the modified citrate method.

Table 3.30 TEC values of $La_{1-x}Sr_xFeO_{3-\delta}$ (x = 0.3-0.7)

Ratio	Temperature range (°C)	TEC ($x10^{-6}$ °C^{-1})	Reference
x = 0.3	50-500	13.07	This work
	50-800	13.33	This work
	30-800	16.30	[58]
x = 0.4	50-500	13.31	This work
	50-800	13.32	This work
	30-1000	16.30	[59]
x = 0.5	50-500	13.82	This work
	50-800	14.28	This work
	677-1037	23.70	[60]
x = 0.6	50-500	14.72	This work
	50-800	15.49	This work
x = 0.7	50-500	15.10	This work
	50-800	16.51	This work
	507-867	29.90	[61]

3.3.2.2 Thermal expansion coefficients of $La_{1-x}Sr_xFe_{0.9}Cr_{0.1}O_{3-\delta}$ (x = 0.3-0.7)

The average thermal expansion coefficient (TEC) of $La_{1-x}Sr_xFe_{0.9}Cr_{0.1}O_{3-\delta}$ (x = 0.3-0.7) in air, obtained from dilatometric curves (Figure 3.37 (a)) are showed in Figure 3.37 (b) and Table 3.30.

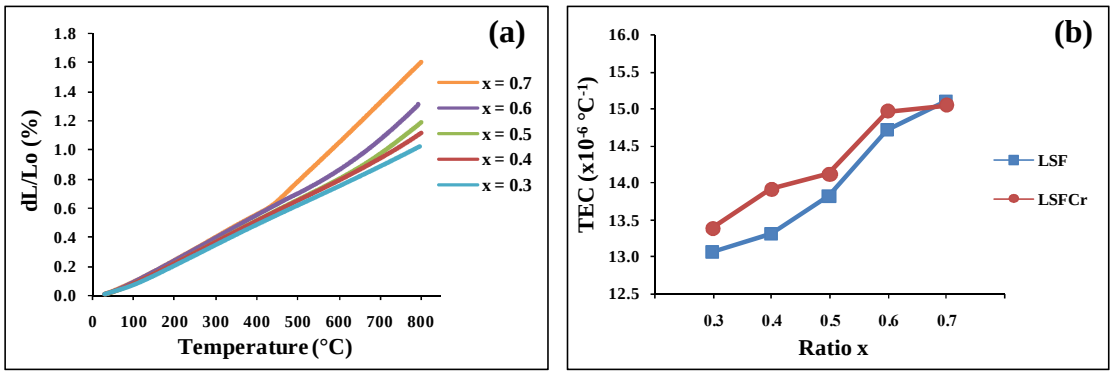

Figure 3.37 (a) Temperature dependence of the thermal expansion for $La_{1-x}Sr_xFe_{0.9}Cr_{0.1}O_{3-\delta}$ (x = 0.3-0.7).
(b) Ratio x dependence of the TEC for $La_{1-x}Sr_xFeO_{3-\delta}$ and $La_{1-x}Sr_xFe_{0.9}Cr_{0.1}O_{3-\delta}$ (x = 0.3-0.7).

Table 3.31 TEC values of $La_{1-x}Sr_xFe_{0.9}Cr_{0.1}O_{3-\delta}$ (x = 0.3-0.7)

Ratio	Temperature range (°C)	TEC ($x10^{-6}$ °C^{-1})
x = 0.3	50-500 50-800	13.38 13.69
x = 0.4	50-500 50-800	13.91 14.54
x = 0.5	50-500 50-800	14.11 15.58
x = 0.6	50-500 50-800	14.96 18.20
x = 0.7	50-500 50-800	15.04 20.96

From Figure 3.37 (b) and Table 3.30, it is seen that the magnitude of the thermal expansion contribution increases with increasing value of x, due to the higher concentration of oxygen vacancies in the samples with more Sr. Moreover, the TECs are observed to increase when Fe is replaced by Cr, can also be explained by electroneutrality condition. Cr is generally in the +3 state and high mobility Cr^{4+} ions

replaced 10% of Fe^{3+} and Fe^{4+}, might cause the increase of oxygen vacancy. It is attributed to the decrease in the covalence of Cr-O bond as compared to Fe-O bond. Thus replacements of Fe with Cr on the B-site cause increasing of TECs.

The expansion behavior of $La_{0.3}Sr_{0.7}Fe_{0.9}Cr_{0.1}O_{3-\delta}$, in those two temperature ranges, can be attributed to two different mechanisms. In the low temperature range (below 450 °C), the intrinsic thermal expansion is due to atomic vibrations of lattice with temperature. In the high temperature range, typically above 450 °C, in addition to the intrinsic thermal expansion, another contribution to the volume expansion is caused by oxygen loss from the structure with the creation of oxygen vacancies (reaction (3.7)), commonly called chemical-induced expansion [57]. The following reaction, where the Kröger -Vink notation is used, is thermally activated:

$$O_O = V_O^{\bullet\bullet} + \frac{1}{2} O_2 + 2e' \qquad (3.7)$$

3.3.2.3 Thermal expansion coefficients of $La_{1-x}Sr_xFe_{0.9}Ni_{0.1}O_{3-\delta}$ (x = 0.3-0.7)

Figure 3.38 and Table 3.31 illustrates the thermal expansion of $La_{1-x}Sr_xFe_{0.9}Ni_{0.1}O_{3-\delta}$ (x = 0.3-0.7) measured in air and the temperature range from room temperature to 800°C.

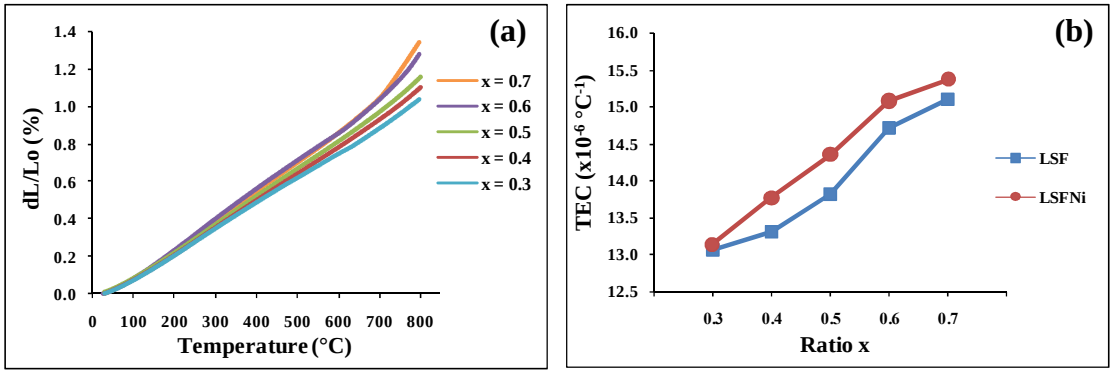

Figure 3.38 (a) Temperature dependence of the thermal expansion for $La_{1-x}Sr_xFe_{0.9}Ni_{0.1}O_{3-\delta}$ (x = 0.3-0.7).
(b) Ratio x dependence of the TEC for $La_{1-x}Sr_xFeO_{3-\delta}$ and $La_{1-x}Sr_xFe_{0.9}Ni_{0.1}O_{3-\delta}$ (x = 0.3-0.7).

Table 3.32 TEC values of $La_{1-x}Sr_xFe_{0.9}Ni_{0.1}O_{3-\delta}$ (x = 0.3-0.7)

Ratio	Temperature range (°C)	TEC ($x10^{-6}$ °C^{-1})
x = 0.3	50-500 50-800	13.14 13.46
x = 0.4	50-500 50-800	13.77 14.37
x = 0.5	50-500 50-800	14.35 15.18
x = 0.6	50-500 50-800	15.08 16.91
x = 0.7	50-500 50-800	15.37 17.70

It can be seen that doping with Ni^{2+} at B site of LSF increased the thermal expansion coefficient as compared with LSF and it increased with increasing the strontium content at A site.

The TEC values of doping with Ni^{2+} at B site were higher than that of undoped Ni^{2+} at B site, due to the larger ion of Ni^{2+} (0.69 A°) is partially replaced into Fe^{3+} (0.645 A°) site. The increase in TECs with increasing strontium content is associated, most likely, with higher concentration of oxygen vacancies formed to charge compensate Sr^{2+}; greater oxygen deficiency is expected to increase anharmonicity of atomic vibrations, the major factor determining thermal expansion of solids [62].

3.3.2.4 Thermal expansion coefficients of $La_{0.4}Sr_{0.6}Fe_{1-y}Ni_yO_{3-\delta}$ (y = 0.0-0.2)

Figure 3.39 compares the thermal expansion in air for compositions in the series $La_{0.4}Sr_{0.6}Fe_{1-y}Ni_yO_{3-\delta}$ (y = 0.0-0.2). The average thermal expansion coefficient (TEC), calculated from the dilatometric data, are summarized in Figure 3.39 (b) and Table 3.32.

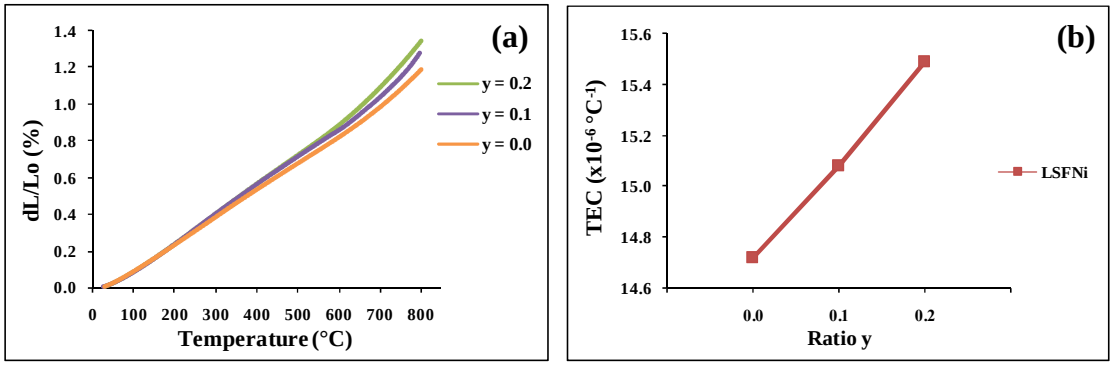

Figure 3.39 (a) Temperature dependence of the thermal expansion for $La_{0.4}Sr_{0.6}Fe_{1-y}Ni_yO_{3-\delta}$ (y = 0.0-0.2).
(b) Ratio y dependence of the TEC for $La_{0.4}Sr_{0.6}Fe_{1-y}Ni_yO_{3-\delta}$ (y = 0.0-0.2).

Table 3.33 TEC values of $La_{0.4}Sr_{0.6}Fe_{1-y}Ni_yO_{3-\delta}$ (y = 0.0-0.2)

Ratio	Temperature range (°C)	TEC (x10^{-6} °C^{-1})
y = 0.0	50-500 50-800	14.72 15.49
y = 0.1	50-500 50-800	15.08 16.91
y = 0.2	50-500 50-800	15.49 17.57

The TEC was measured versus Ni content and Sr content remaining constant (i.e. $La_{0.4}Sr_{0.6}Fe_{1-y}Ni_yO_{3-\delta}$ (y = 0.0-0.2)). A significant increase of the TEC value was observed with Ni content corresponding to the works of Kharton, *et al.* [63] explained that the average thermal expansion coefficient of $La_{1-y}Sr_yFe_{1-x}Ni_xO_{3-\delta}$ (x = 0.1-0.4, y = 0.1-0.2) ceramics rising with strontium and nickel contents. Its value vary in the ranges (12.4-13.4) × 10^{-6} K^{-1} at 700-1150 K and (14.2-18.0) × 10^{-6} K^{-1} at 1150-1370 K.

Increasing temperature leads to progressive oxygen losses from $La_{0.4}Sr_{0.6}Fe_{1-y}Ni_yO_{3-\delta}$ lattice and to decreasing oxidation states of the transition metal. As expected, this effect becomes more pronounced with nickel additions. The resultant oxygen vacancies formation cause the thermal expansion coefficient of Ni^{2+} samples increased with increasing the amount of Ni^{2+}.

3.3.2.5 Thermal expansion coefficients of $La_{1-x}Sr_xFe_{0.9}Cu_{0.1}O_{3-\delta}$ (x = 0.3-0.7)

The thermal expansion curves of $La_{1-x}Sr_xFe_{0.9}Cu_{0.1}O_{3-\delta}$ (x = 0.3-0.7) are presented in Figure 3.40 and TEC values of the perovskite oxides are listed in Table 3.33.

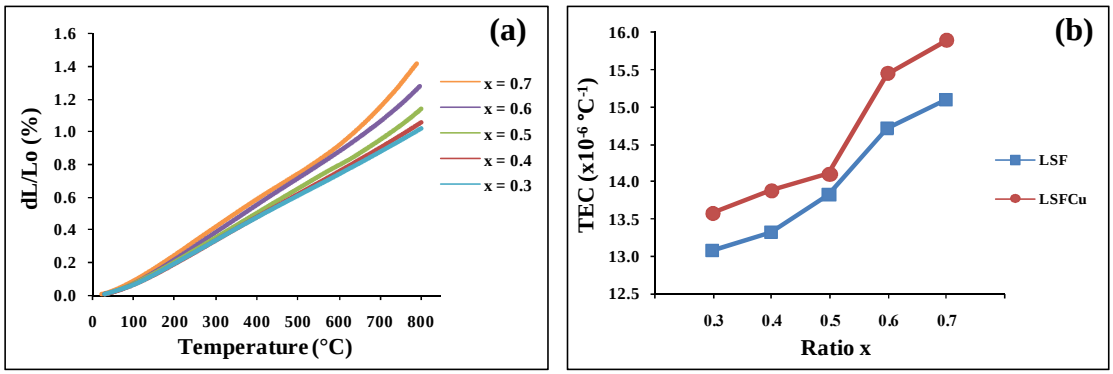

Figure 3.40 (a) Temperature dependence of the thermal expansion for $La_{1-x}Sr_xFe_{0.9}Cu_{0.1}O_{3-\delta}$ (x = 0.3-0.7).
(b) Ratio x dependence of the TEC for $La_{1-x}Sr_xFeO_{3-\delta}$ and $La_{1-x}Sr_xFe_{0.9}Cu_{0.1}O_{3-\delta}$ (x = 0.3-0.7).

Table 3.34 TEC values of $La_{1-x}Sr_xFe_{0.9}Cu_{0.1}O_{3-\delta}$ (x = 0.3-0.7)

Ratio	Temperature range (°C)	TEC ($x10^{-6}$ °C^{-1})
x = 0.3	50-500 50-800	13.58 13.65
x = 0.4	50-500 50-800	13.88 14.28
x = 0.5	50-500 50-800	14.03 14.94
x = 0.6	50-500 50-800	15.45 16.88
x = 0.7	50-500 50-800	15.89 18.93

In Figure 3.40 (b) and Table 3.33, the thermal expansion coefficient obtained from the slopes of the thermal expansion curves of Figure 3.40 (a). The thermal expansion coefficient of $La_{1-x}Sr_xFe_{0.9}Cu_{0.1}O_{3-\delta}$ (x = 0.3-0.7) samples increased with increasing the amount of Sr and increased with doping Cu at B site. They were similar to the results of Ni but the TEC values of Cu specimens were

higher than those of Ni. This increase suggested the ionic radius of Cu^{2+} (0.73 A°) is larger than Ni^{2+} (0.69 A°) and Fe^{3+} (0.645 A°).

From the results of thermal expansion, it is proved that partial replacement of Sr at the A-site is significant to increase the thermal expansion coefficient of $La_{1-x}Sr_xFe_{1-y}M_yO_{3-\delta}$ (M = Cr, Ni and Cu). This increase suggested the formation of oxygen vacancies due to charge compensate Sr^{2+}. The TEC values of $La_{1-x}Sr_xFeO_{3-\delta}$ increased with doping Cr, Ni and Cu 0.1 mol in B-site. The thermal expansion coefficient of $La_{0.4}Sr_{0.6}Fe_{1-y}M_yO_{3-\delta}$ samples increased with increasing the amount of Ni.

Consequently, the substitution with Sr at the A-site and Cr, Ni and Cu at B-site cannot improve thermal expansion property of $La_{1-x}Sr_xFeO_{3-\delta}$ for matching with yttria-stabilised zirconia (~ 10.7×10^{-6} °C^{-1}) electrolyte.

3.3.3 Oxygen permeation

Mixed oxide-ionic and electronic conduction ceramics (MIECs) have been attracted much attention due to their high potential for applications in various electrochemical devices. MIECs display oxide ionic conductivity, thereby they are suitable to be materials for SOFCs such as cathode and electrolyte. The oxygen permeation measurement was thus preformed to confirm the oxide ion conduction in the specimens.

In this study, $La_{0.4}Sr_{0.6}Fe_{0.8}Ni_{0.2}O_{3-\delta}$ materials that had highest specific conductivity were selected as the representative membrane compositions for the oxygen permeation measurement at elevated temperature range from 600-1000 °C. The effects of surface modification by $La_{0.6}Sr_{0.4}CoO_{3-\delta}$ or $La_{0.4}Sr_{0.6}Fe_{0.8}Ni_{0.2}O_{3-\delta}$ onto $La_{0.4}Sr_{0.6}Fe_{0.8}Ni_{0.2}O_{3-\delta}$ membranes for oxygen permeating property were also evaluated. Additionally, the following abbreviations were used for this section: LSCo64 for $La_{0.6}Sr_{0.4}CoO_{3-\delta}$; LSFNi4682 for $La_{0.4}Sr_{0.6}Fe_{0.8}Ni_{0.2}O_{3-\delta}$ without catalyst coating; C1-LSCo for membrane coated with $La_{0.6}Sr_{0.4}CoO_{3-\delta}$ on the air side; C2-LSCo for membrane coated with $La_{0.6}Sr_{0.4}CoO_{3-\delta}$ on both air and He sides; C1-LSFNi4682 for membrane coated with $La_{0.4}Sr_{0.6}Fe_{0.8}Ni_{0.2}O_{3-\delta}$ on the air side; and C2-LSFNi4682 for membrane coated with $La_{0.4}Sr_{0.6}Fe_{0.8}Ni_{0.2}O_{3-\delta}$ on both air and He sides.

3.3.3.1 Morphologies of surface catalysts

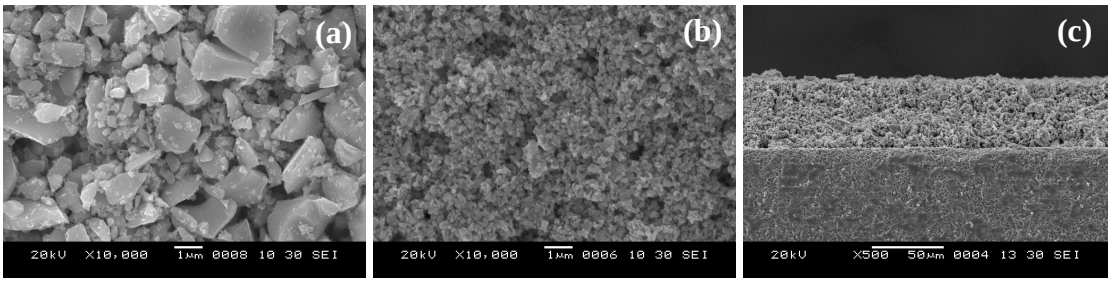

Figure 3.41 SEM micrographs of (a) porous LSCo64 surface, (b) porous LSFNi4682 surface and (c) cross section of the LSCo64 catalyst layer on LSFNi4682 specimen.

Microstructures of the LSCo64 and LSFNi4682 catalyst-coating layer on LSFNi4682 are represented in Figure 3.41. The specimen which was treated at 800 °C shows porous and particulate microstructure. According to our results, the grain sizes of LSFNi4682 (Figure 3.41 (b)) were significantly smaller than those of LSCo64 (Figure 3.41 (a)). As seen in Figure 3.41(c) representing the cross section of the catalyst layer on LSFNi4682 specimen, the catalyst-coating layer can be clearly distinguished from the LSFNi4682 membrane.

3.3.3.2 Oxygen permeation of the unmodified LSFNi4682

The oxygen permeation property of LSFNi4682 was investigated as a function of temperature.

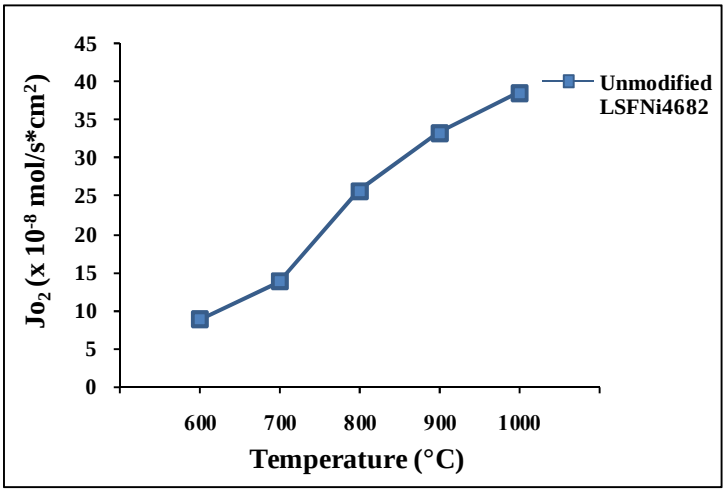

Figure 3.42 Temperature dependence of the oxygen permeation flux (Jo_2) for the unmodified LSFNi4682 specimen.

Table 3.35 Oxygen permeation flux of the unmodified LSFNi4682

Temperature (°C)	**Oxygen permeation flux (× 10^{-8} mol/s*cm^2)**
600	8.68
700	13.74
800	25.61
900	33.22
1,000	38.44

Figure 3.42 presents the change of oxygen permeation flux with temperature for the unmodified LSFNi4682 membrane. An increase in oxygen permeation flux with temperature is due to the increase in mobility and concentration of ionic carriers at high temperature [44]. Additionally, if the thickness of membrane is small enough compared with the characteristic length, i.e., if the kinetics of oxygen permeation is in a surface-exchange rate-controlled condition, we can regard the thermally activated surface-exchange rate as another cause for an increase in oxygen permeation flux.

The oxygen permeation flux of LSFNi4682 shows the maximum value of 38.44 × 10^{-8} mol/s*cm^2 at 1,000 °C (the highest operating temperature in this experiment), as displayed in Figure 3.42 and Table 3.34.

For Sr-doped lanthanum and Ni-doped ferrite metal oxide ($La_{1-x}Sr_x Fe_{1-y}M_yO_{3-\delta}$) whose lanthanum and ferrite lattice sites were occupied by strontium and nickel ions, respectively, negative effective charges (Sr'_{La} and Ni'_{Fe}) were formed. These negative effective charges need to be compensated by the formation of equivalent amount of positive effective charges, such as electron holes ($h^{\bullet}$) or oxygen vacancies ($V_O^{\bullet\bullet}$) [41]. The latter assumably cause oxygen permeability.

3.3.3.3 Oxygen permeation of the modified LSFNi4682 with porous LSCo64 surface catalyst

Temperature dependence for the oxygen permeation flux of the modified LSFNi4682 with porous LSCo64 surface catalyst is displayed in Figure 3.43.

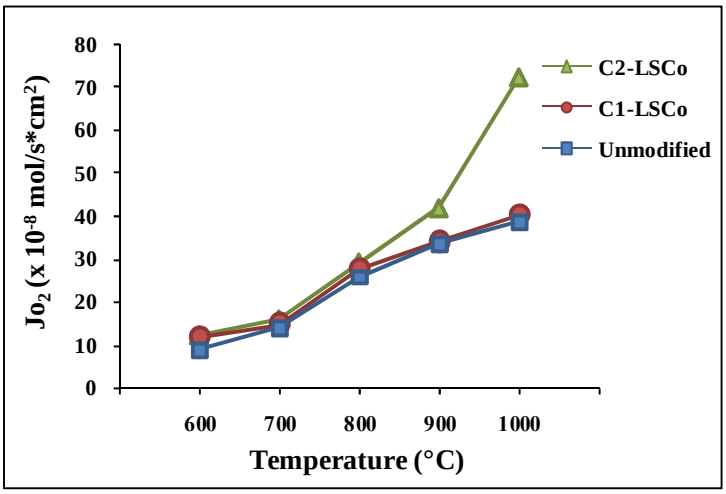

Figure 3.43 Temperature dependence of the oxygen permeation flux (Jo_2) for the unmodified LSFNi4682 specimen and the modified LSFNi4682 specimen with porous LSCo64 surface catalyst.

Table 3.36 Oxygen permeation fluxes of the unmodified LSFNi4682 specimen and the modified LSFNi4682 specimens with porous LSCo64 surface catalyst

Temperature (°C)	Oxygen permeation rate (× 10^{-8} mol/s*cm^2)		
	Unmodified	Coated-LSCo64	
		Air side	Air and He sides
600	8.68	11.84	12.18
700	13.74	14.71	15.88
800	25.61	27.39	29.11
900	33.22	33.80	41.69
1,000	38.44	39.97	72.09

The oxygen permeation fluxes of the LSFNi4682 membranes modified by porous LSCo64 are correlatively represented with that of the unmodified specimen in Figure 3.43 and Table 3.35. The oxygen permeation flux of the unmodified LSFNi4682 specimen was increased by coating porous LSCo64 at the air side. This

result suggests that oxygen dissociation reaction in air side was improved by surface catalyst. The oxygen permeation rate slightly increased and the highest oxygen permeation rate of 39.97 × 10^{-8} mol/s*cm^2 at 1,000 °C was achieved.

The porous LSCo64 layer coating on both air and He sides of the LSFNi4682 membrane greatly improved the oxygen permeation flux of the uncoated membrane from 38.44 × 10^{-8} to 72.09 × 10^{-8} mol/s*cm^2 at the temperature of 1,000°C. These increases in the oxygen permeation fluxes at all temperatures (600-1000 °C) may be caused by increases in both effective surface area and surface activity for oxygen dissociation and association at air and He sides, respectively [44].

3.3.3.4 Oxygen permeation of the modified LSFNi4682 with porous LSFNi4682 surface catalyst

Using LSFNi4682 with porous structure as its own surface catalyst, the oxygen permeation curves for the modified LSFNi4682 with porous LSFNi4682 are shown in Figure 3.44 and the average oxygen permeation flux of these oxides in comparison with the data of the unmodified one are displayed in Table 3.36.

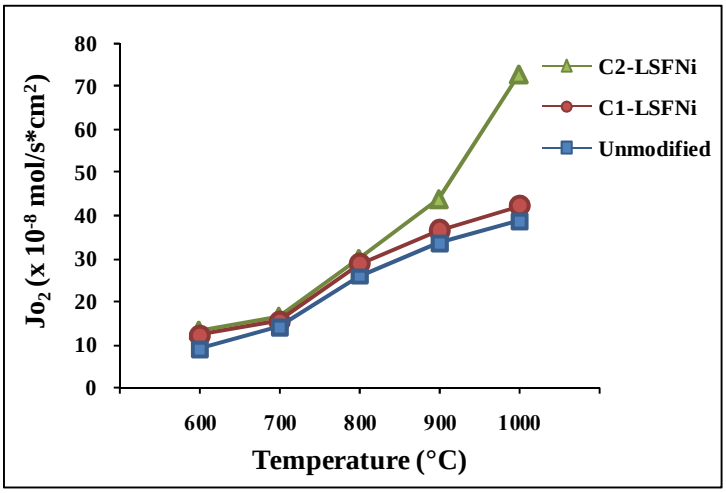

Figure 3.44 Temperature dependence of the oxygen permeation flux (Jo_2) for the unmodified LSFNi4682 specimen and the modified LSFNi4682 specimens with porous LSFNi4682 surface catalyst.

Table 3.37 Oxygen permeation fluxes of the unmodified LSFNi4682 specimen and the modified LSFNi4682 specimens with porous LSFNi4682 surface catalyst

Temperature (°C)	Oxygen permeation rate (× 10^{-8} mol/s*cm^2)		
	Unmodified	Coated-LSFNi4682	
		Air side	Air and He sides
600	8.68	12.07	12.84
700	13.74	15.29	16.08
800	25.61	28.54	29.53
900	33.22	36.33	43.46
1,000	38.44	41.98	72.51

Figure 3.44 presents oxygen permeation fluxes from air to He environment through LSFNi4682 membranes with and without porous LSFNi4682 surface catalyst and the results showed similar trend as these of Figure 3.43. The oxygen permeation flux of LSFNi4682 membrane increased by applying porous LSFNi4682 catalyst layers, and the largest enhancement was observed with the coating on both air and He sides (72.51 × 10^{-8} mol/s*cm^2 at 1,000 °C), followed by the coating only on the membrane air side (41.98 × 10^{-8} mol/s*cm^2 at 1,000 °C). The ratio of the oxygen permeation flux of the LSFNi4682 coated on both sides to that of the unmodified LSFNi4682 is approximately 1.89 at 1000 °C.

However, the oxygen permeation flux of the LSFNi4682 coated specimen is higher than the LSCo64 coated one. It is possible that higher oxygen permeation flux due to LSFNi4682 surface catalyst might be related to its grain sizes. As showed in Figure 3.42, the grain sizes of LSFNi4682 were smaller than those of LSCo64 so the surface active area of LSFNi4682 catalyst is more than that that of LSCo64.

In conclusion, the results of oxygen permeation experiment demonstrated that the surface morphologies of the membrane can affect the oxygen permeation flux. By introducing the LSCo64 or LSFNi4682 surface catalyst on the either side or both sides of LSFNi4682 membrane, significant promotion in oxygen permeation flux could be obtained. The oxygen permeation flux of the LSFNi4682 coated membrane is higher than that of LSCo64 coated one. The highest oxygen permeating flux of 72.51 × 10^{-8} mol/s*cm^2 (at 1,000 °C) from air to He was achieved on LSFNi4682 membrane coated with LSFNi4682 on both air and He sides.

CHAPTER IV

CONCLUSIONS

4.1 Conclusions

$LaFeO_3$ perovskites doped with various compositions of Sr ions at A-site and Cr, Ni and Cu at B-site were synthesized by the modified citrate method. The structures of the synthesized perovskite compounds were characterized by XRD, confirming that $La_{1-x}Sr_xFe_{1-y}M_yO_{3-\delta}$ (M = Cr, Ni and Cu; x = 0.3-0.7; y = 0.0-0.3) had cubic perovskite structure. All of the XRD patterns revealed the single phase of ABO_3 perovskite oxides except the pattern of $La_{0.4}Sr_{0.6}Fe_{0.7}Ni_{0.3}O_{3-\delta}$ which showed an impurity phase, suggesting that 0.3 mol of Ni cannot be doped at the B-site of $La_{0.4}Sr_{0.6}FeO_{3-\delta}$.

Moreover, the XRD analysis indicated that La substitution by Sr at A-site affected on the lattice parameter of the perovskite. With the addition of Sr, the lattice parameter decreased. It was likely that the electroneutrality compensation of the perovskite oxide via the formation of oxygen vacancies caused the shrinkage of lattice parameter. Compared to the B-site replacement (substituting Fe with Cr, Ni and Cu); the lattice parameter changed slightly.

Surface morphology of the sintered discs was examined by SEM. SEM characterization concluded that each sample exhibited high density (more than 92%) with homogeneous surface. The grain sizes of $La_{1-x}Sr_xFeO_{3-\delta}$ increased with the amount of Sr in A-site as well as Cu and Ni quantities in B-site. On the other hand, doping with Cr at B-site decreased the grain sizes. Additionally, $La_{0.4}Sr_{0.6}Fe_{0.7}Cr_{0.3}O_{3-\delta}$ has the smallest grain sizes whereas $La_{0.4}Sr_{0.6}Fe_{0.7}Cu_{0.3}O_{3-\delta}$ has the largest grain sizes.

From the conductivity results, the partial replacement of trivalent lanthanum for divalent strontium results in an increase the electrical conductivity of $LaFeO_{3-\delta}$. It can be clearly seen that the electrical conductivity of $La_{1-x}Sr_xFeO_{3-\delta}$ increased with the Sr content owing the conversion of Fe^{3+} to Fe^{4+} to stabilize A-site doping. For x = 0.7, the electrical conductivity of $La_{1-x}Sr_xFeO_{3-\delta}$ shows the highest value which is 420.99

S/cm at 550 °C. By replacing Fe with Ni and Cu at B-site, the enhancement of $La_{1-x}Sr_xFeO_{3-\delta}$ conductivity can be achieved. However, the increase in the amount of Cr doping at B-site lowered the perovskite electrical conductivity. Nevertheless, it is satisfied that the electrical conductivity of $La_{1-x}Sr_xFeO_{3-\delta}$ could be greatly improved by simultaneous doping Sr and Ni at A- and B-sites. The specific conductivity of 495.46 S/cm for $La_{0.4}Sr_{0.6}Fe_{0.8}Ni_{0.2}O_{3-\delta}$, at intermediate temperature (550 °C) was obtained in this work.

The thermal expansion values proved that partial replacement of Sr at the A-site is significant to increase the thermal expansion coefficients of $La_{1-x}Sr_xFe_{1-y}M_yO_{3-\delta}$. The volume expansion of the material could arise via the thermal reduction of the valence state of iron from Fe^{4+} to Fe^{3+} (r_{Fe}^{4+} = 0.585 A° and r_{Fe}^{3+} = 0.645 A°) and the formation of oxygen vacancies due to charge compensation for Sr^{2+}. The TEC values of $La_{1-x}Sr_xFeO_{3-\delta}$ increased with doping Cr, Ni and Cu 0.1 mol in B-site. On the other hand, the thermal expansion coefficient of $La_{0.4}Sr_{0.6}Fe_{1-y}Ni_yO_{3-\delta}$ samples increased with the amount of Ni.

Oxygen permeating information demonstrated that the LSFNi4682 membrane was improved in oxygen permeation flux by the coating of porous LSCo64 or LSFNi4682 surface catalyst layers. The modification on both air and He sides with porous surface catalysts makes LSFNi4682 perovskite be better oxygen permeable membrane. The highest oxygen permeating flux obtained from this work is 72.51 × 10^{-8} mol/s*cm^2 at 1,000 °C for the LSFNi4682 membrane coated with LSFNi4682 on both air and He sides.

$La_{0.4}Sr_{0.6}Fe_{0.8}Ni_{0.2}O_{3-\delta}$ with the specific conductivity of 495.46 S/cm at about 550 °C, the oxygen permeability of 72.51 × 10^{-8} mol/s*cm^2 at 1000 °C and the thermal expansion coefficient of 15.49 × 10^{-6} $°C^{-1}$ at the temperature range 50-500 °C can compete with other materials for uses in Intermediate Temperature Solid Oxide Fuel Cells (IT-SOFCs).

4.2 Suggestion

From experiment results, the future work should be focused on the following:

1. Improvement for the oxygen permeability of $La_{0.4}Sr_{0.6}Fe_{0.8}Ni_{0.2}O_{3-\delta}$ membrane by coating on both air and He sides with the fine particle surface catalyst.
2. Studies for the electrochemical performance of $La_{0.4}Sr_{0.6}Fe_{0.8}Ni_{0.2}O_{3-\delta}$ specimens in single cell testing.

REFERENCES

[1] U.S. Department of Energy. Comparison of Fuel Cell Technologies [Online]. (n.d.). Available from: http://www1.eere.energy.gov/hydrogenandfuelcells/fuelcells/pdfs/fc_comparison_chart.pdf [2009, November 3]

[2] Badwal, S.P.S., and Foger K. Solid Oxide Electrolyte Fuel Cell Review. Ceramics International 22 (1996): 257-265.

[3] Fuel Cell Test and Evaluation Center (FCTec). Solid Oxide Fuel Cell (SOFC) [Online]. (n.d.). Available from: http://www.fctec.com/fctec_types_sofc.asp [2009, November 3]

[4] Minh, N.Q. Ceramic Fuel Cells. Journal of the American Ceramic Society 76 (1993): 563-88.

[5] Wincewicz, K.C., and Cooper, J.S. Taxonomies of SOFC material and manufacturing alternatives. Journal of Power Sources 140 (2005): 280-296.

[6] Amethyst Galleries. Perovskite [Online]. Available from: http://www.galleries.com/ minerals/oxides/perovski/perovski.htm [2009, November 5]

[7] Gyeongsang National University. ABO_3 ideal perovskite structure [Online]. (n.d.). Available from: http://super.gsnu.ac.kr/lecture/inorganic/perovskite.html [2009, November 5]

[8] Peña, M.A., and Fierro, J.L.G. Chemical Structures and Performance of Perovskite Oxides. Chemical Reviews 101 (2001): 1981-2017.

[9] West, A.R. Solid State Chemistry and Its Applications, John Wiley & Sons, Chichester, 1984.

[10] West, A.R. Basic Solid State Chemistry, John Wiley & Sons, Chichester, 1988.

[11] Bouwmeester, H.J.M., and Burggraaf, A.J. Dense ceramic membranes for oxygen separation, in: A.J. Burggraaf, L. Cot (Eds.), Fundamentals of Inorganic Membrane Science and Technology, Elsevier Science B.V., Amsterdam, 1996.

[12] Marques, R.M.C., Marques, F.M.B., and Frade, J.R. Characterization of mixed conductors by dc techniques. Part I: Theoretical solutions, Solid State Ionics 73 (1994): 15-25.

[13] Mizusaki, J., Yoshihiro, M., Yamauchi, S., and Fueki, K. Nonstoichiometry and Defect Structure of the Perovskite-Type Oxides $La_{1-x}Sr_xFeO_{3-\delta}$, Solid State Chemistry 58 (1985): 257-266.

[14] Teraoka, Y., Nobunaga, T., and Yamazoe, N. Effect of Cation Substitution on the Oxygen Semipermeability of Perovskite-Type Oxide, Chemistry Latters (1988): 503-506.

[15] Sunarsoa, J., Baumannb, S., Serrac, J.M., Meulenbergb, W.A., Liua, S., Lind, Y.S., and Diniz da Costa, J.C. Mixed ionic-electronic conducting (MIEC) ceramic-based membranes for oxygen separation. Journal of Membrane Science 320 (2008): 13-41.

[16] Bouwmeester, H. J. M., Kruidhof, H., and Burggraaf, A. J. Influence of the Surface Exchange Kinetics in Rate Limiting Oxygen Permeation Through Mixed-Conducting Oxides. Solid State Ionics 72 (1994): 185-194.

[17] Teraoka, Y., Zhang, H. M., Furukawa, S., and Yamazoe, N. Oxygen Permeation Through Perocskite-Type Oxide. Chemistry Letters (1985): 1743-1746.

[18] Capoen, E., Steil, M.C., Nowogrocki, G., Malys, M., Pirovano, C., Löfberg, A., Bordes-Richard, E., Boivin, J.C., Mairesse, G., and Vannier, R.N. Oxygen permeation in bismuth-based materials. Part I: Sintering and oxygen permeation fluxes. Solid State Ionics 177 (2006): 483-488.

[19] Kusaba, H., Shibata, Y., Sasaki, K., and Teraoka, Y. Surface effect on oxygen permeation through dense membrane of mixed-conductive LSCF perovskite-type oxide. Solid State Ionics 177 (2006): 2249.

[20] van Hassel, B.A. Oxygen transfer across composite oxygen transport membranes, Solid State Ionics 174 (2004): 253.

[21] Cousin, P., and Ross, R.A. Preparation of mixed oxides: a review. Materials Science and Engineering: A 130 (1990): 119-125.

[22] Bhalla, A.S., Guo, R., and Roy, R. The perovskite structure-a review of its role in ceramic science and technology. Materials Research Innovations 4 (2000): 3-26.

[23] Cushing, B.L., Kolesnichenko, V.L., and O'Connor, C.J. Recent advances in the liquid phase syntheses of inorganic nanoparticles. Chemical Reviews 104 (2004): 3893.

[24] Haas, P.A. Gel processes for preparing ceramics and glasses. Chemical Engineering Progress 85 (1989): 44.

[25] Inoue, O., and Kawashima, S. Methods for producing crystalline complex perovskite compounds. US Patent 4,853,199 (1989).

[26] Liu, S., Tan, X., Li, K., and Hughes, R. Synthesis of strontium cerates-based perovskite ceramics via water-soluble complex precursor routes. Ceramics International 28 (2002): 327-335.

[27] Pechini, M.P. Method of preparing lead and alkaline earth titanates and niobates and coating method using the same to form a capacitor. US Patent 3,330,697 (1967).

[28] Nagamoto, H., Hayashi, K., and Inoue, H. Methane oxidation by oxygen transported through solid electrolyte. Journal of Catalysis 126 (1990): 671-673.

[29] Dawson, W.J. Hydrothermal synthesis of advanced ceramic powders. American Ceramic Society Bulletin 67 (1988): 1673.

[30] Hart, A.M., Peters, B.C., Plonka, J.H., West, W.H., and Macki, J.M. Advanced ceramic opportunities-a review. Chemical Engineering Progress 85 (1989): 44.

[31] Roy, D.M., and Oyefesobi, S.O. Preparation of very reactive Ca_2SiO_4 powder. Journal of the American Ceramic Society 60 (1977): 178.

[32] Lenntech. Calcination [Online]. (n.d.). Available from: http://www.lenntech.com /chemistry/calcination.htm [2009, November 10]

[33] Kuczynski, G.C. Transactions of the American Institute of Mining, Metallurgical, and Petroleum Engineering. Journal of Applied Physics, 21 (1950): 632-637.

[34] Gosavi, P.V., and Biniwale, R.B. Pure phase $LaFeO_3$ perovskite with improved surface area synthesized using different routes and its characterization. Journal of Materials Chemistry and Physics 119 (2010): 324-329.

[35] Yu, H., Fung, K., Guo, T., and Chang, W. Syntheses of perovskite oxides nanoparticles $La_{1-x}Sr_xMO_{3-\delta}$ (M = Co and Cu) as anode electrocatalyst for direct methanol fuel cell. Electrochimica Acta, 50 (2004): 811-816.

[36] Simner, S., Anderson, M., Bonnett, J., and Stevenson J. Enhanced low temperature sintering of (Sr, Cu)-doped lanthanum ferrite SOFC cathodes. Solid State Ionics 175 (2004): 79-81.

[37] Kharton, V.V., Viskup, A.P., Bochkov, D.M., Naumovich, E.N., and Reut O.P. Mixed electronic and ionic conductivity of $LaCo(M)O_3$ (M=Ga, Cr, Fe or Ni) III. Diffusion of oxygen through $LaCo_{1-x-y}Fe_xNi_yO_{3-\delta}$ ceramics. Solid State Ionics 110 (1998): 61-68.

[38] Ortiz-Vitoriano, N., Ruiz de Larramendi, I., Ruiz de Larramendi, J.I., Arriortua, M.I., and Rojo, T. Synthesis and electrochemical performance of $La_{0.6}Ca_{0.4}Fe_{1-x}Ni_xO_3$ (x = 0.1, 0.2, 0.3) material for solid oxide fuel cell cathode. Journal of Power Sources 192 (2009): 63-69.

[39] Ishihara, T., Ishikawa, S., Hosoi, K., Nishiguchi, H., and Takita, Y. Oxide ionic and electronic conduction in Ni-doped $LaGaO_3$-based oxide. Solid State Ionics 175 (2004): 319-322.

[40] Lu, H., Tong, J., Deng, Z., Cong, Y., and Yang, W. Crystal structure, oxygen permeability and stability of $Ba_{0.5}Sr_{0.5}Co_{0.8}Fe_{0.1}M_{0.1}O_{3-\delta}$ (M = Fe, Cr, Mn, Zr) oxygen-permeable membranes. Materials Research Bulletin, 41 (2006): 683-689.

[41] Virattayanon, N. Synthesis of $La_{0.7}Sr_{0.3}Fe_{1-x}M_xO_3$ (M= Ni, Cu, Al and Mn) as anode materials for solid oxide fuel cell. A Master Thesis, Program in Petrochemistry and Polymer Science, Faculty of Science, Chulalongkorn University, 2008.

[42] Huang, Y., Vohs, J.M., and Gorte, R.J. Fabrication of Sr-doped $LaFeO_3$-YSZ composite cathodes. Journal of the Electrochemical Society, 151 (2004): A646-A651.

[43] Teraoka, Y., Honbe, Y., Ishii, J., Furukawa, H., and Moriguchi, I. Catalytic effects in oxygen permeation through mixed-conductive LSCF perovskite membranes. Solid State Ionics, 152-153 (2002): 681-687.

[44] Lee, S., Lee, K.S., Woo, S.K., Kim, J.W., Ishihara, T., and Kim .D.K. Oxygen-permeating property of $LaSrBFeO_3$ (B=Co, Ga) perovskite membrane surface-modified by $LaSrCoO_3$, Solid State Ionics 158 (2003): 287-296.

[45] Ishihara, T., Tsuruta, Y., Todaka, T., Nishiguchi, H., Takita, Y. Fe doped $LaGaO_3$ perovskite oxide as an oxygen separating membrane for CH_4 partial oxidation. Solid State Ionics 152-153 (2002): 709-714.

[46] Tai, L.W., Nasrallah, M.M., Anderson, H.U., Sparlin, D.M., and Sehlin, S.R. Structure and electrical properties of $La_{1-x}Sr_xCo_{1-y}Fe_yO_3$. Part 1. The system $La_{0.8}Sr_{0.2}Co_{1-y}Fe_yO_3$. Solid State Ionics 76 (1995): 259-271.

[47] Armstrong, T.R., Stevenson, J.W., Pederson, L.R., and Raney, P.E. Dimensional Instability of Doped Lanthanum Chromite Journal of the Electrochemical Society 143 (1996): 2919-2925.

[48] Rodríguez-Martínez, L.M., Vidal, K., Ortega-San-Martín, L., Díez-Linaza, E., Nó, M. L., Rojo, T., Laresgoiti, A., and Arriortua, M. I. Isolating the effect of doping in the structure and conductivity of $(Ln_{1-x}M_x)FeO_{3-\delta}$ perovskites. Solid State Ionics 178 (2007): 1310-1316.

[49] Kharton, V.V., Shaulo, A.L., Viskup, A.P., Avdeev, M., Yaremchenko, A.A., Patrakeev, M.V., Kurbakov, A.I., Naumovich, E.N., and Marques, F.M.B. Perovskite-like system (Sr, La)(Fe, Ga)$O_{3-\delta}$: structure and ionic transport under oxidizing conditions. Solid State Ionics 150 (2002): 229-243.

[50] Patrakeev, M.V., Leonidov, I.A., Kozhevnikov, V.L., and Poeppelmeier, K.R. p-Type electron transport in $La_{1-x}Sr_xFe_{3-\delta}$ at high temperatures. Solid State Chemistry 178 (2005): 921-927.

[51] Berchmansa, L.J., Sindhub, R., Angappana, S., and Augustin, C.O. Effect of antimony substitution on structural and electrical properties of $LaFeO_3$. Journal of Materials Processing Technology 207 (2008): 301-306.

[52] Kim, M.C., Park, S.J., Haneda, H., Tanaka, J., and Shirasaki, S. High temperature electrical conductivity of $La_{1-x}Sr_xFeO_{3-\delta}$ (x>0.5) Solid State Ionics 40-41 (1990): 239-243.

[53] Patrakeev, M.V., Mitberg, E.B., Lakhtin, A.A., Leonidov, I.A., Kozhevnikov, V I., Kharton, V.V., Avdeev, M., and Marquesw, F.M.B. Oxygen nonstoichiometry, conductivity and Seebeck coefficient of $La_{0.3}Sr_{0.7}Fe_{1-x}Ga_xO_{2.65+\delta}$ perovskites. Solid State Chemistry 167 (2002): 203-213.

[54] Wikipedia. Chromium [Online]. (n.d.). Available from: http://en.wikipedia.org /wiki/Chromium [2009, December 30]

[55] Kharton, V.V., Figueiredo, F. M., and Kovalevsky, A.V. Processing, microstructure and properties of $LaCoO_{3-\delta}$ ceramics. Journal of the European Ceramic Society 21 (2001): 2301-2309.

[56] Wei, B., L¨u, Z., Huang, X., Liu, M., Li, N., and Su,W. Synthesis, electrical and electrochemical properties of $Ba_{0.5}Sr_{0.5}Zn_{0.2}Fe_{0.8}O_{3-\delta}$ perovskite oxide for IT-SOFC cathode. Journal of Power Sources 176 (2008): 1-8.

[57] Justea, E., Julian, A., Etchegoyen, G., Geffroy, P.M., Chartier, T., Richet, N., and Del Gallo P. Oxygen permeation, thermal and chemical expansion of (La, Sr)(Fe, Ga)$O_{3-\delta}$ perovskite membranes. Journal of Membrane Science 319 (2008): 185-191.

[58] Ullmann, H., Trofimemko, N., Tietz, F., Stöver, D., and Ahmad-Khanlou, A. Correlation between thermal expansion and oxide ion transport in mixed conducting perovskite-type oxides for SOFC cathodes. Solid State Ionics 138 (2000): 79-90.

[59] Kindermann, L., Poulsen, F.W., Larsen, P.H., Nickel, H., and Hilpert, K. Synthesis and properties of La-Sr-Mn-Fe-O based perovskites. In: 3. European solid oxide fuel cell forum. , Proceedings 3rd ed., Europe, (1998): 123-132.

[60] Kharton, V.V., Waerenborgh, J.C., Viskup, A.P., Yakovlev, S.O., Patrakeev, M.V., Gaczyński, P, Marozau, I.P., Yaremchenko, A.A., Shaula, A.L., and Samakhval**,** V.V. Mixed conductivity and Mössbauer spectra of $(La_{0.5}Sr_{0.5})_{1-x}Fe_{1-y}Al_yO_{3-\delta}$ (x=0-0.05, y=0-0.30). Solid State Chemistry 179 (2006): 1273-1284.

[61] Shaula, A.L., Yaremchenko, A.A., Kharton, V.V., Logvinovich, D.I., Naumovich, E.N., Kovalevsky, A.V., Frade, J.R., and Marques. F.M.B. Oxygen permeability of $LaGaO_3$-based ceramic membranes. Journal of Membrane Science 221 (2003): 69-77.

[62] Tsipis, E.V., Patrakeev, M.V., Kharton, V.V., Yaremchenko, A.A., Mather, G.C., Shaula, A.L., Leonidov, I.A., Kozhevnikov, V.L., and Frade J.R. Transport properties and thermal expansion of Ti-substituted $La_{1-x}Sr_xFeO_{3-\delta}$ (x=0.5-0.7). Solid State Sciences 7 (2005): 355-365.

[63] Tsipis, E.V., Kiselev, E.A., Kolotygin, V.A., Waerenborgh, J.C., Cherepanov, V.A., and Kharton, V.V. Mixed conductivity, Mössbauer spectra and thermal expansion of (La, Sr)(Fe, Ni)$O_{3-\delta}$ perovskites. Solid State Ionics 179 (2008): 2170-2180.

[64] Wikipedia. ionic radius [Online]. (n.d.). Available from: http://en.wikipedia.org /wiki/Ionic_radius [2009, December 30]

APPENDICES

APPENDICES

APPENDICE A

Tolerance number

Goldschmidt (1926) defined the tolerance limits of the size of ions through a tolerance factor, t as Equation (A.1)

$$t = \frac{(r_A + r_O)}{\sqrt{2}(r_B + r_O)} \qquad \text{(A.1)}$$

where r_A, r_B, and r_O are the radii of respective ions. For the substituted perovskite at A and B site, $A_{1-x}A'_xB_{1-y}B'_yO_{3-\delta}$, r_A and r_B were calcuated from the sum of each metal at A site and B site, respectively, time its compostition. The atomic weight, ionic charge, coordination number, and ionic radius of all concerned metals were shown in Table A.1

Table A.1 Atomic weight, ionic charge, coordination number, and ionic radius of concerned metals [64]

Element	Charge	Ionic radius
La	3+	1.032
Sr	2+	1.180
Fe	2+	0.780
Fe	3+	0.645
Fe	4+	0.585
Cu	2+	0.730
Cu	3+	0.540
Ni	2+	0.690
Ni	3+	0.600
Ni	4+	0.480
Cr	3+	0.615
O	2-	1.400

Therefore, as Equation A.1 the tolerance number of perovskite compounds such as LSFNi 4682 was calculated as below.

$$\text{tolerance number of LSFNi 4682} = \frac{(1.032 \times 0.4) + (1.18 \times 0.6) + 1.40}{\sqrt{2}\,[(0.645 \times 0.8) + (0.69 \times 0.2) + 1.40]} = 1.19$$

APPENDICE B

Activation Energy (E_a)

Arrhenius plot of LSFNi 4682 is given in Figure B-1. The linear part can be described by the small polaron conduction mechanism, following the formula:

$$\sigma = (A/T)\, e^{(-Ea/RT)}$$

$$\ln(\sigma T) = \ln A\, e^{(-Ea/RT)}$$

$$\ln(\sigma T) = \ln e^{(-Ea/RT)} + \ln A \qquad \text{(B.1)}$$

$$\ln(\sigma T) = (-E_a/R)(1000/T) + \ln A$$

y **slope** **x** **intercept y axis**

$$-E_a/K = \text{Slope of the linear}$$

$$E_a = -\text{Slope} \times K$$

A is material constant including the carrier concentration term,

σ = The specific conductivity (S/cm)

E_a = The activation energy (kJ/mol)

T = Temperature (K)

R = The gas constant = 8.314472 J/K.mol

From Equation B.1 Arrhenius plot of ln σT versus 1000/*T* gives a straight line, whose slope and intercept can be used to determine E_a and *A*.

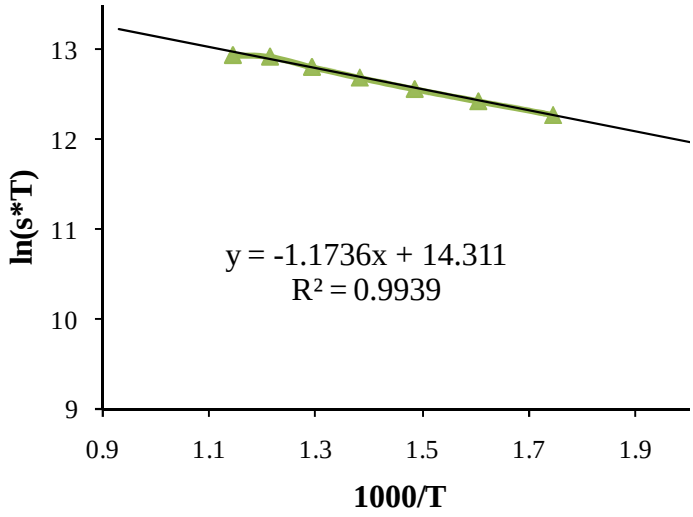

Figure B.1 Arrhenius plot of the electrical conductivity of LSFNi 4682

The activation energy calculated from the slope of the straight line of figure B.1 For example, the activation energy (*E*a) of LSFNi 4682, was calculated as below:

BSCF ; The linear equation is

$$y = -1.1736x + 14.311$$

$$\text{Slope} = -1.1736 = -E_a/R$$

Then, $E_a = -1.1736 \times 8.314472 = 9.76$ kJ/mol

APPENDICE C

Table C.1 Specific conductivity of $La_{1-x}Sr_xFeO_{3-\delta}$ (x = 0.3-0.7)

Ratio	Specific conductivity, σ (S/cm)						
	27°C	**250°C**	**300°C**	**350°C**	**400°C**	**450°C**	**500°C**
x = 0.3	0.38	26.05	44.30	63.12	80.17	95.64	108.81
x = 0.4	0.63	35.17	59.35	84.68	108.05	128.89	145.98
x = 0.5	9.16	181.58	230.59	267.90	289.09	307.11	312.85
x = 0.6	16.39	209.63	261.40	300.06	329.64	353.23	374.90
x = 0.7	56.95	295.80	330.61	357.45	377.88	392.99	413.37

Ratio	Specific conductivity, σ (S/cm)						
	550°C	**600°C**	**650°C**	**700°C**	**750°C**	**800°C**	**σ_{max} (T,°C)**
x = 0.3	119.12	128.09	135.76	142.62	148.38	151.31	151.31(800)
x = 0.4	160.60	173.89	185.53	197.47	205.84	212.33	212.33(800)
x = 0.5	318.78	323.07	325.52	317.44	311.86	286.66	325.52(650)
x = 0.6	395.75	410.76	414.78	398.77	362.08	312.48	414.78(650)
x = 0.7	420.99	399.95	358.14	304.62	255.06	202.94	420.99(550)

Table C.2 Specific conductivity of $La_{1-x}Sr_xFe_{0.9}Cr_{0.1}O_{3-\delta}$ (x = 0.3-0.7)

Ratio	Specific conductivity, σ (S/cm)						
	27°C	**250°C**	**300°C**	**350°C**	**400°C**	**450°C**	**500°C**
x = 0.3	0.65	31.87	43.10	53.42	62.26	69.68	79.38
x = 0.4	0.65	29.81	45.53	62.92	77.58	91.26	102.43
x = 0.5	4.78	86.31	110.03	130.07	149.24	164.82	178.20
x = 0.6	5.50	82.07	111.39	139.20	164.58	193.69	218.66
x = 0.7	11.30	87.17	110.94	136.58	160.23	181.55	202.52

Ratio	Specific conductivity, σ (S/cm)						
	550°C	**600°C**	**650°C**	**700°C**	**750°C**	**800°C**	**σ_{max} (T,°C)**
x = 0.3	83.35	87.48	90.86	92.96	93.76	93.30	93.76(800)
x = 0.4	111.58	121.31	129.24	137.54	142.99	145.55	145.55(800)
x = 0.5	189.67	199.96	206.56	206.27	200.44	184.35	206.56(650)
x = 0.6	237.39	244.00	236.52	216.05	188.23	159.37	244.00(600)
x = 0.7	213.84	214.47	197.64	168.30	143.73	122.14	214.47(600)

Table C.3 Specific conductivity of $La_{0.4}Sr_{0.6}Fe_{1-y}Cr_yO_{3-\delta}$ (y = 0.0-0.3)

Ratio	Specific conductivity, σ (S/cm)						
	27°C	**250°C**	**300°C**	**350°C**	**400°C**	**450°C**	**500°C**
y = 0.0	16.39	209.63	261.40	300.06	329.64	353.23	374.90
y = 0.1	5.50	82.07	111.39	139.20	164.58	193.69	218.66
y = 0.2	2.38	36.96	56.36	74.37	87.74	101.81	116.10
y = 0.3	2.19	31.36	41.73	52.27	61.60	70.63	79.01

Ratio	Specific conductivity, σ (S/cm)						
	550°C	**600°C**	**650°C**	**700°C**	**750°C**	**500°C**	**σ_{max} (T,°C)**
y = 0.0	395.75	410.76	414.78	398.77	362.08	312.48	414.78(650)
y = 0.1	237.39	244.00	236.52	216.05	188.23	159.37	244.00(600)
y = 0.2	125.05	128.93	126.37	121.19	112.05	103.61	128.93(600)
y = 0.3	87.21	93.67	97.70	97.48	91.73	84.91	97.70(650)

Table C.4 Specific conductivity of $La_{1-x}Sr_xFe_{0.9}Ni_{0.1}O_{3-\delta}$ (x = 0.3-0.7)

Ratio	Specific conductivity, σ (S/cm)						
	27°C	**250°C**	**300°C**	**350°C**	**400°C**	**450°C**	**500°C**
x = 0.3	7.43	84.47	107.87	129.91	149.11	166.31	180.39
x = 0.4	9.31	100.51	130.84	156.91	179.72	199.09	215.90
x = 0.5	68.37	205.62	235.80	262.40	285.73	305.53	322.50
x = 0.6	101.77	313.50	348.38	383.96	405.11	421.92	446.60
x = 0.7	147.55	321.43	349.48	371.14	386.43	403.03	424.89

Ratio	Specific conductivity, σ (S/cm)						
	550°C	**600°C**	**650°C**	**700°C**	**750°C**	**800°C**	**σ_{max} (T,°C)**
x = 0.3	192.06	202.50	212.24	220.66	227.81	230.06	230.06(800)
x = 0.4	230.39	242.50	254.75	266.59	277.96	283.67	283.67(800)
x = 0.5	356.34	347.07	320.48	269.98	235.59	200.17	356.34(550)
x = 0.6	460.72	453.77	431.87	384.87	323.62	279.69	460.72(550)
x = 0.7	432.41	410.93	371.53	332.17	274.77	231.71	432.41(550)

Table C.5 Specific conductivity of $La_{0.4}Sr_{0.6}Fe_{1-y}Ni_yO_{3-\delta}$ (y = 0.0-0.2)

Ratio	Specific conductivity, σ (S/cm)						
	27°C	**250°C**	**300°C**	**350°C**	**400°C**	**450°C**	**500°C**
y = 0.0	16.39	209.63	261.40	300.06	329.64	353.23	374.90
y = 0.1	101.77	313.50	348.38	383.96	405.11	421.92	446.60
y = 0.2	131.85	330.42	371.18	397.79	422.21	446.29	470.32

Ratio	Specific conductivity, σ (S/cm)						
	550°C	**600°C**	**650°C**	**700°C**	**750°C**	**500°C**	**σ_{max} (T,°C)**
y = 0.0	395.75	410.76	414.78	398.77	362.08	312.48	414.78(650)
y = 0.1	460.72	453.77	431.87	384.87	323.62	279.69	460.72(550)
y = 0.2	495.46	475.25	435.63	396.46	350.32	302.90	495.46(550)

Table C.6 Specific conductivity of $La_{1-x}Sr_xFe_{0.9}Cu_{0.1}O_{3-\delta}$ (x = 0.3-0.7)

Ratio	Specific conductivity, σ (S/cm)						
	27°C	**250°C**	**300°C**	**350°C**	**400°C**	**450°C**	**500°C**
x = 0.3	3.20	86.31	109.05	127.45	141.73	152.33	160.68
x = 0.4	8.37	123.77	146.84	168.19	184.99	197.15	207.12
x = 0.5	77.71	254.29	277.74	295.62	309.92	321.28	327.79
x = 0.6	77.09	220.88	249.39	272.23	286.81	298.00	313.41
x = 0.7	85.66	223.69	245.63	261.45	272.98	285.03	298.41

Ratio	Specific conductivity, σ (S/cm)						
	550°C	**600°C**	**650°C**	**700°C**	**750°C**	**800°C**	**σ_{max} (T,°C)**
x = 0.3	167.09	172.14	176.77	181.75	186.28	185.49	186.28(750)
x = 0.4	214.06	220.20	227.38	232.14	235.69	231.42	235.69(750)
x = 0.5	332.20	333.97	332.37	317.81	290.11	249.91	333.97(600)
x = 0.6	329.39	341.87	339.18	317.37	275.82	235.79	341.87(600)
x = 0.7	310.30	312.84	296.90	264.46	218.21	175.45	312.84(600)

Table C.7 Specific conductivity of $La_{0.4}Sr_{0.6}Fe_{1-y}Cu_yO_{3-\delta}$ (y = 0.0-0.3)

Ratio	Specific conductivity, σ (S/cm)						
	27°C	**250°C**	**300°C**	**350°C**	**400°C**	**450°C**	**500°C**
y = 0.0	16.39	209.63	261.40	300.06	329.64	353.23	374.90
y = 0.1	77.09	220.88	249.39	272.23	286.81	298.00	313.41
y = 0.2	75.74	210.31	227.38	240.82	251.11	262.07	275.94
y = 0.3	78.55	203.32	221.23	236.65	249.73	261.83	274.50

Ratio	Specific conductivity, σ (S/cm)						
	550°C	**600°C**	**650°C**	**700°C**	**750°C**	**500°C**	**σ_{max} (T,°C)**
y = 0.0	395.75	410.76	414.78	398.77	362.08	312.48	414.78(650)
y = 0.1	329.39	341.87	339.18	317.37	275.82	235.79	341.87(600)
y = 0.2	287.22	288.67	278.26	266.40	244.57	210.73	288.67(600)
y = 0.3	284.24	283.29	275.80	259.00	228.14	193.62	284.24(550)

VITAE

Miss Aunpajsuda Chaiyawong was born on January 5, 1985 in Chiang Mai, Thailand. She graduated with Bachelor's Degree in Industrial Chemistry from Faculty of Science, Chiang Mai University in 2007. She continued her study in Petrochemistry and Polymer Science Program, Faculty of Science, Chulalongkorn University in 2007 and completed in 2010.

PRESENTATIONS:

October 15-17, 2009.

Poster Presentation: "Electrical conductivity of $La_{1-x}Sr_xFeO_{3-\delta}$ and $La_{1-x}Sr_xFe_{0.9}Cu_{0.1}O_{3-\delta}$ perovskite oxides" The 35^{th} congress on science and technology of Thailand (STT 35), Burapha University, Thailand.